2020

Single-particle Cryo-EM Study of the Ric-8A:Gαi1 Complex

JAKE David JOHNSTON Mr

Single-Particle Cryo-EM Study of the Ric-8A:Gαi1 Complex

A Thesis submitted to the University of Montana for the degree of Master's in Biochemistry and Biophysics

2020

Jake Johnston

List of Contents

List of Tables

List of Figures

List of Abbreviations

ADP……Adenosine diphosphate
AHD……..…….alpha helical domain
Amp…….....Ampicillin
ARM……Armadillo
ATP…….Adenosine triphosphate
BME……..Beta mercaptoethanol
cAMP……..cyclic-adenosine monophosphate
Carb…….Carbenicillin
CHAPS…….……...3-[(3-cholamidopropyl)dimethylammonio]-1-propanesulfonate
CK2…….……...Casein Kinase 2
CCD…….Charge-coupled device
Cryo-EM…….....cryogenic electron microscopy
CTF……Contrast transfer function
DEER…….electron-electron double resonance spectroscopy
DNA…….deoxyribonucleic acid
DQE……..Detective quantum efficiency
DTT……..…..Dithiothreitol
e.coli……..Escherichia coli
EDTA……Ethylenediaminetetraacetic acid
EGTA……ethylene glycol-bis(β-aminoethyl ether)-N,N,N′,N′-tetraacetic acid
Fab…….Monoclonal fragments antigen binding
FPLC…….……...Fast protein liquid chromatography
FEG……..Field emission gun
FSC……..Fourier Shell Correlation
GAP……...GTPase activating protein
Gα…….……G-alpha subunit
GDP……Guanosine diphosphate
GEF…….……Guanine nucleotide exchange factor
GPCR……G-protein coupled receptor
GTPγS…….…….Guanosine 5’-O-[gamma-thio]triphosphate
GTP……Guanosine triphosphate
HCL…….Hydrochloric acid
HDX-MS……Hydrogen-Deuterium Exchange-mass spectrometry
IPTG……..Isopropyl β- d-1-thiogalactopyranoside
Kan…….Kanamycin
LB……..Luria Broth
LL…….....Lima Bean, Leupeptin
MBP……...Maltose binding protein
mES…….……..Mouse Embryonic Stem cells
MES……2-(N-morpholino)ethanelsulfonic acid
mGiα1……...myristoylated Gαi1
MTF……...Modulation transfer function
MWCO…….....Molecular weight cutoff
Nb……Nanobody
Ni-NTA……Nickel Nitrotriacetic acid

OD…… ……...Optical density
PDB……Protein Data Bank
PLCβ……..…..phospholipase Cβ
PMSF……..Phenylmethylsulfonyl fluoride
PTT……PMSF, TLCK, TPCK
RCC1…….Regulator of chromosome condensation 1
RGS……..Regulator of G-protein signaling
Ric……...Resistance to inhibitors of cholinesterase
RNA……..Ribonucleic acid
RNAi…….Ribonucleic acid interference
Rpm……Rotations per minute
RT……...Room temperature
SDS-PAGE……Sodium dedocyl sulfate polyacrylamide gel electrophoresis
SOS……..Sons of sevenless
TB……..….Terrific broth
TBP……....Tris, BME, PTT
TCEP……...tris(2-carboxyethyl)phosphine
TfbI…….....Transformation buffer I
TfbII…….…….Transformation buffer II
TEM……...Transmission electron microscope

Abstract

The University of Montana

Jake Johnston

Master’s Biochemistry and Biophysics

2020

G-proteins regulate several cellular processes and, when defective, have been associated with multiple endocrinal disorders. Heterotrimeric G-proteins are comprised of α, β, and γ subunits that are regulated through the binding of GDP (resting state) or GTP (active state) to the α-subunit, a process that is typically accelerated by membrane bound guanine nucleotide exchange factors (GEFs), such as G protein couple receptors (GPCRs). Ric-8A is a 60-kDa cytosolic protein that has been demonstrated to act not only as a GEF but as a molecular chaperone for the Gα i, q and 12/13 subunit families. Both Ric-8A GEF and chaperone activities are accelerated by phosphorylation at its C-terminus by casein kinase II. The structural mechanisms by which Ric-8A functions as a GEF and a molecular chaperone are poorly understood. We were able to isolate Ric-8A in complex with nucleotide-free Gα subunit for structural studies. We have determined a near atomic-resolution (~4 Å) structure of phosphorylated Ric-8A bound to nucleotide free Gαi1 using single-particle cryo-electron microscopy (cryo-EM). To facilitate Cryo-EM structure determination, the Ric-8A:Gαi1 complex was determined in accompany with four single-domain antibodies. The structure provides novel insights into elevated Ric-8A GEF activity from phosphorylation at the C-terminus along with mechanistic details of how Ric-8A moderates structural elements around the nucleotide binding sites of G proteins to promote GDP release. The work presented here provides a novel mechanism for G-protein activation.

Acknowledgments

Over the last five years I have worked on many projects as an undergraduate student and a Master's student in the Sprang laboratory. Many of the people in this lab have taught me many things that has ultimately led me to this point. They were all very enthusiastic, kind and knew how to enjoy the moment to make things as fun as possible. There also many other people outside of the lab who greatly helped me along the way. I would like to highlight all of these people.

I would like to Dr. Stephen Sprang for taking me in as an undergraduate student and a Master's student in his laboratory. He has been a great mentor and hopefully I was somewhat tolerable at times! I also owe a great deal of thanks to Dr. Tung-chung Mou who ultimately mentored me in the lab and allowed a wonderful opportunity to also fulfill the work presented in this thesis. His guidance and advice have been critical to my success with this project. I would also like to thank Cindee for all of her goofiness and keeping things interesting as always. Dr. Levi Mcclelland for tolerating me and allowing me to torment him on a daily basis that would drive any normal person to insanity. Dr. Sascha Stump for being an overall great lab member and for always knowing how to give me hard time over everything, pushing my stress level to new heights! Marlene for being Marlene and for teaching me proper lab techniques along the way. Furthermore, I would like to thank my parents for all of their support over my life and for always being so supportive of anything I have ever done. My wonderful girlfriend, Cynthia Janku, for putting up with all of my long hours and constant working. Also, her ability to keep me from working myself to death, which I would probably would have done! For all of this, I am very thankful! I would like to discuss contributions to this project also, as it was a very collaborative project. Kaiming Zhang performed cryo-EM vitrification, data collection, and processing for publication. I learned these steps under his guidance and re-processed data for this thesis. I prepared and optimized cryo-EM samples. Dr. Tung-Chung Mou performed model building for the project.

Chapter 1. Introduction.

1.1 A brief introduction to proteins.

Proteins are the most versatile macromolecules that reside in living systems and are essential in almost all biological processes. Proteins can function as catalysts, transport molecules, store other molecules, provide mechanical support, and transmit nerve impulses. Each type of protein has a unique structure that allows for diversity in their function (1). Proteins contain grooves and bulges on their surfaces that are necessary for specific protein-DNA/RNA interactions and protein-protein interactions. These grooves and bulges of proteins occur from different combinations of α-helical and β-sheet polypeptide chains that form the secondary structure. Polypeptides are made up of different sequences from the 20 types of amino acid molecules that ultimately define the properties of a protein. This dissertation will focus on protein to protein interaction and structure in regards to cell signaling mechanisms for G-proteins.

1.2 Introduction to cell signaling and G-Protein Coupled Receptors.

Cells in a multicellular organism experience constant bombardment from a variety of extracellular signals that have to be interpreted and translated into the appropriate response for their environment. These signals can either be soluble factors that are generated locally such as in synaptic transmission, or distantly such as with hormones and growth factors. Cells have to maintain a diversity of receptors to respond appropriately to the individual stimuli that they may experience. As such, there are several major classes of receptors that include G-protein Coupled Receptors (GPCRs), ligand gated ion channels, integrins, receptor tyrosine kinases, and cytokine receptors (2). GPCRs are the largest family of receptors and can be found in many organisms from fungi to animals. GPCRs have seven transmembrane spanning segments where the N-terminus of the protein resides outside the cell, and C-terminus in the inside of the cell. GPCRs bind a very diverse set of ligands ranging from proteins, small molecules, hormones and drugs that are recognized by the N-terminus of the protein and/or by a pocket formed by the extracellular and intracellular domains. The binding of an agonist to a GPCR initiates the G-Protein cycle transducing a signaling cascade and then acting to terminate the signal (3). Based on the characteristics of this project, the G-protein cycle will be discussed in further detail.

1.3.1 The G-Protein Cycle in cell signaling

Heterotrimeric G-proteins are comprised of α, β, and γ subunits that reside in an inactive state when the α-subunit is bound to guanosine diphosphate (GDP) and are activated when GDP is exchanged for guanosine triphosphate (GTP) on the α-subunit. The binding of an agonist to a GPCR induces a conformational change that causes the GPCR to act as guanine nucleotide exchange factor (GEF) which accelerates the release of GDP from the α-subunit and allowing for binding of GTP (4). Binding of GTP to Gα causes the dissociation of the βγ subunits that then can act on downstream signaling effectors (5). GTP bound to the Gα subunit is then hydrolyzed to GDP, resulting in deactivation, a process accelerated by GTPase activating proteins (GAPS). This is depicted in Figure 1.1.

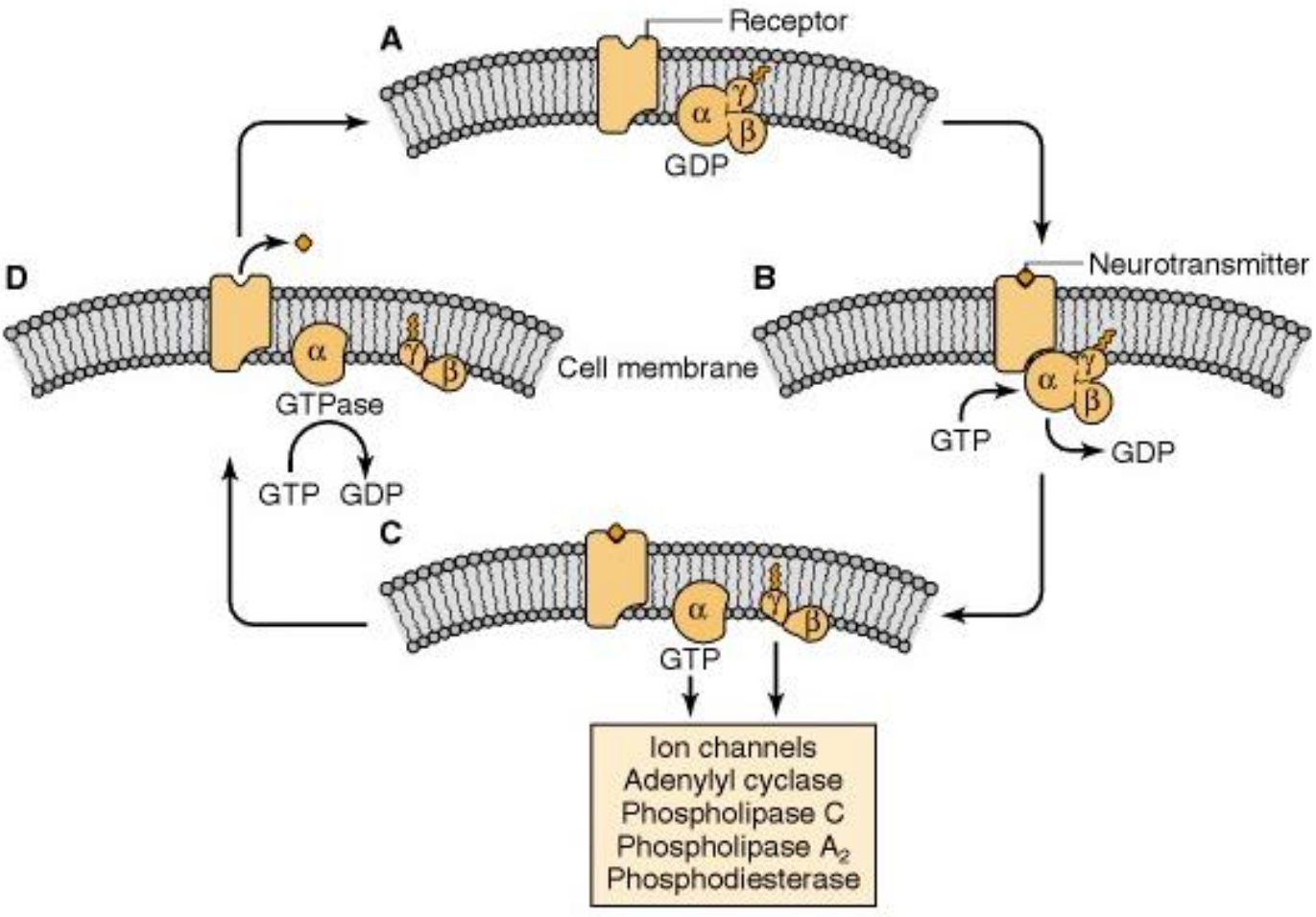

Figure 1.1) Overview of the G-protein cycle. Figure obtained from reference (6).

1.3.2 Different Classifications of heterotrimeric G-protein alpha subunits

Heterotrimeric G-proteins are classified based on the sequence and functional similarities of the Gα subunits. They are grouped into four different families: Gαs, Gαi, Gαq, and Gα12. The Gαs family contains two members that include Gαs and Gαolf where the s stands for stimulation and olf for olfactory. Gαs is expressed in most cells, while Gαolf is expressed only in olfactory sensory neurons (7). Members of the Gαs family interacts directly with adenylate cyclase to simulate the production of cyclic-adenosine monophosphate (cAMP) (8). Gαi is the largest and most diverse family consisting of Gαi1, Gαi2, Gαi3, Gαit, Gαo, Gαz, and Gαg which are present in most cells (7). Gαi (i representing inhibitory) inhibits production of cAMP by interacting directly with adenylate cyclase (9). In humans, the Gαq family is comprised of four different classes: Gα16, Gα11, Gα14 and Gαq. Gα16 and Gα14 are expressed in hematopoietic cells or in kidney cells, while Gαq and Gα11 are expressed ubiquitously (7). Gαq interacts with isoforms phospholipase Cβ (PLCβ) which results in an increase in intracellular Ca^{2+} and activation of protein kinase C (10, 11). The Gα12 family is comprised of Gα12 and Gα13 which are expressed ubiquitously (7). Gα12 interacts with a small subset of RhoGEFs which includes p115 RhoGEF, LARG, and PDZ-RhoGEF, that activate the small GTPase Rho (12, 13, 14).

1.3.3 Lipid modifications of Heterotrimeric G-protein alpha subunits

Gα subunits are N-terminally modified by covalent attachment of the fatty acids myristate (14 carbon fatty acid chain) and/or palmitate (16 carbon fatty acid chain). N-myristoylation of Gαi occurs co-translationally at a glycine at the N-terminus following removal of the initiator methionine (15). All Gα subunits, except Gαt, can undergo reversible palmitoylation to a cysteine near the N-terminus via a thioester bond (15). Lipid modification for Gα subunits is important for their proper membrane localization as palmitoylation results in the stable attachment of Gα to the cellular membrane (16). Myristoylation contributes to membrane localization, though interestingly, the expression of myristoylated Gαi/o results in a substantial portion in the cytosolic fraction, while palmitoylation still resulted in membrane retention (17,18,19). Palmitoylation and/or myristoylation of Gα subunits affects their interaction with their effectors and localization to specific cell membrane regions (20, 21, 22, 23).

1.3.4 Structure of heterotrimeric G-protein alpha subunits

The alpha subunit of heterotrimeric G-proteins contains two domains: The Ras-like and the Helical domain. The Ras-like domain consists of a six-stranded β-sheet with five helices and contains switch I, II, and III regions that undergo differing conformational changes in the presence of GDP, GTP, and other nucleotide adducts with GDP and GTP stabilizing alternate conformations (24, 25, 26, 170). GTP binding restrains and stabilizes the Gα switch regions, especially switch II, that provides a stable surface for interactions with effectors and inhibiting interactions with Gβγ subunits. Upon GTP hydrolysis, the switch regions become flexible, especially switch II, which results in a conformation that allows for interaction with Gβγ subunit in an inactive state. In complex with Gβγ, the switch II region now becomes rigid (27). The helical domain is a six helical bundle with postulated roles as an effector recognition domain (28), increasing GTP binding (29), functioning as a tethered intrinsic GTPase activating protein (30, 31), regulating Gα oligomerization (28, 30), and participating in the inactive-active conformational transitions of Gα (32).

Together, the helical and ras-like domains are held together by two flexible linkers that form a deep pocket for binding guanine nucleotides (33) where the nucleotide interacts with five conserved sequence motifs labeled G1-G5 (for G-binding) that show universally conserved structure and function (34). A diphosphate binding loop (P-loop or G1), containing the sequence GxxxxGK(S/T), contacts the α- and β-phosphates of the guanine nucleotide and connects the β1 strand to the α1 helix. G-proteins containing the P-loop motif are described as the “P-loop containing nucleotide triphosphate hydrolase superfamily”. The G3 loop, with the sequence of DXXG, located at the N-terminus of switch II links the sites required for binding the γ-phosphate of GTP and Mg^{2+}. The guanine ring is recognized by the NKXD sequence of the G4 loop that links the β5 strand and the α4 helix. The G2 loop corresponds to the switch I, which connects the helical domain to the β2 strand, contains a conserved threonine residue that functions in Mg^{2+} coordination. The G5 loop located between the β6 and α5 helix and containing the consensus sequence (T/G)(C/S)A, supports the guanine recognition site (35). The structure of Gαi1 bound to GTP is shown in Figure 1.2 and the nucleotide interactions are shown in Figure 1.3.

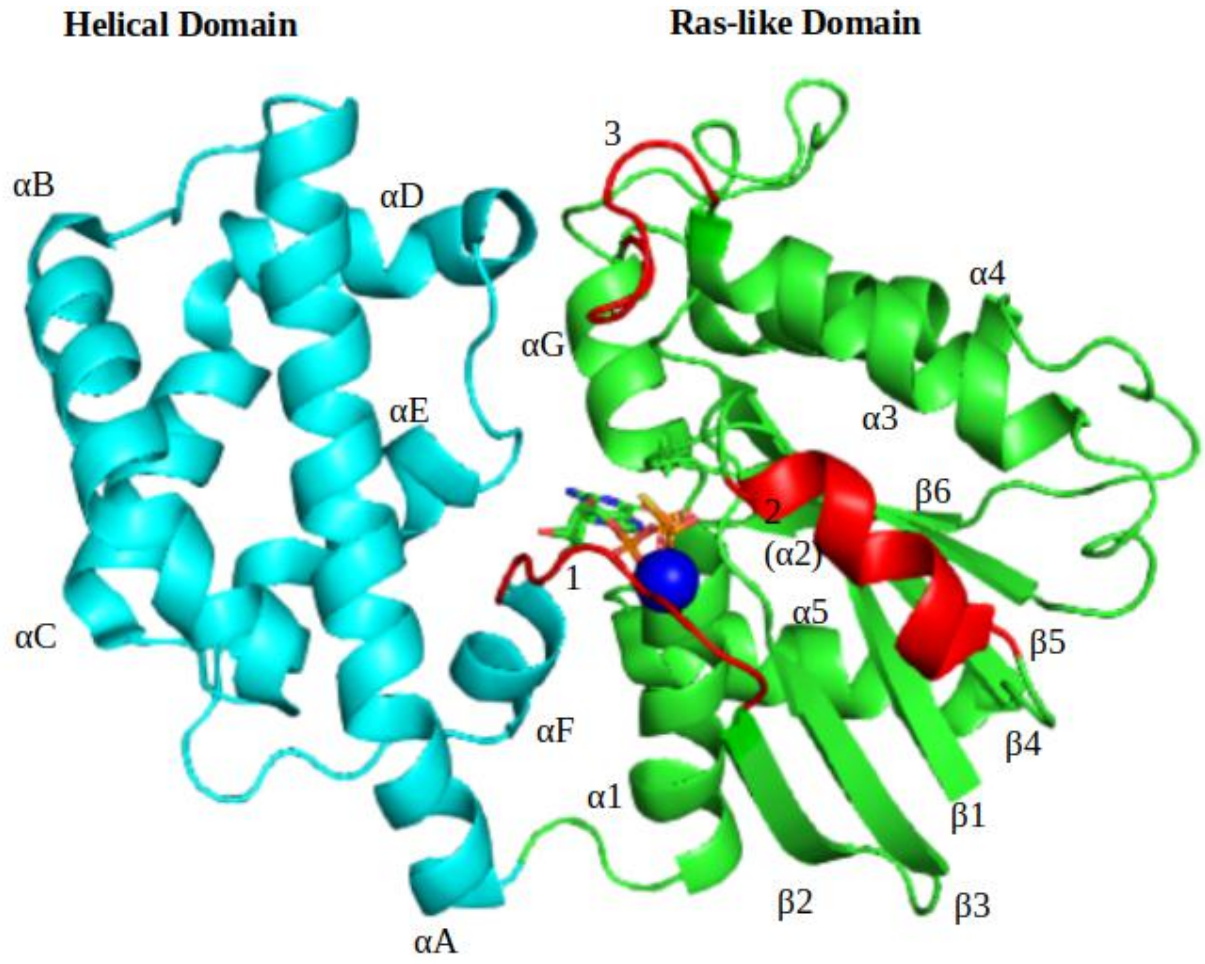

Figure 1.2) Crystal structure of Gαi1 bound to GTP from PDB (1GIA) made in pymol. The helical domain is shown in cyan and the Ras-like domain is shown in green. The switch regions are colored in red and are labeled with their corresponding numbers. The secondary elements are labeled, the magnesium ion is shown as a blue sphere and GTP is shown as a stick. The labeling of the secondary elements follows the convention that has been configured for the alpha subunit of heterotrimeric G-proteins. Helices in the helical domain are labeled from a-f. In the Ras-like domain, helices are numbered 1-5 and the beta sheets are labeled 1-6 from the N-to-C terminus. Switch I and II become disordered when bound to GDP.

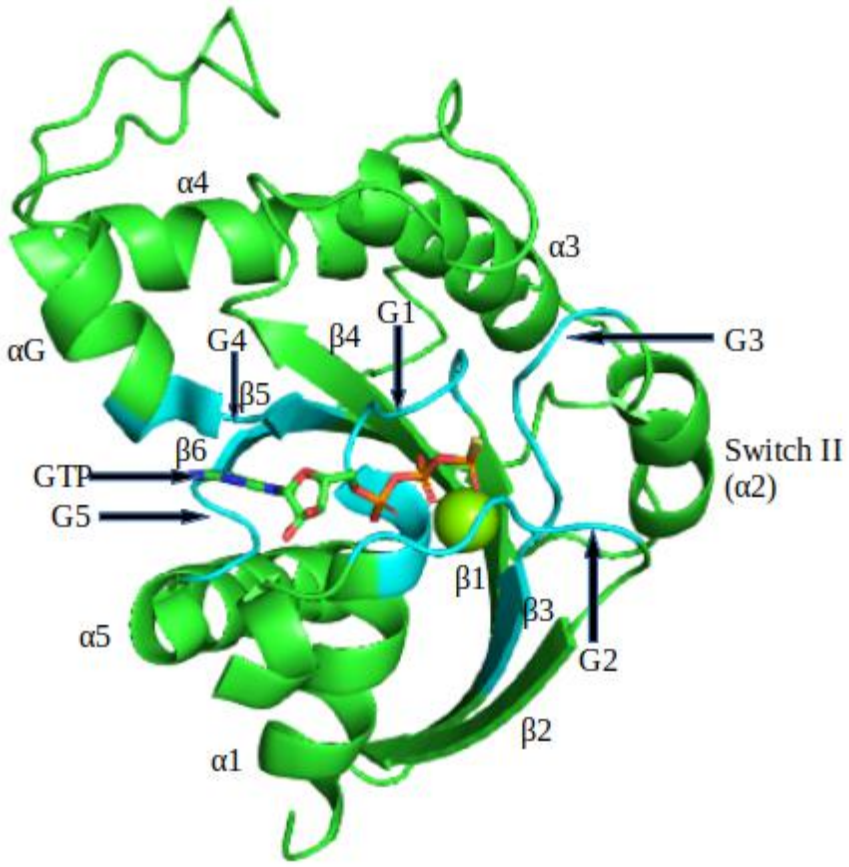

Figure 1.3) The Ras-like domain for Gαi1 from PDB (1GIA) made using pymol. The conserved motifs that make up the polypeptide loops interact with the guanine nucleotide are shown in cyan, while GTP is shown cyan, while GTP is shown as a stick model. The magnesium ion is shown as a green sphere in the model.

1.4: Regulation of G-proteins by Receptor-independent GEFs

As described above, the nucleotide-binding pocket of G-proteins are very conserved, where the binding of GDP and GTP proceeds through a conserved manner. This has generally been described as a "switch" mechanism, where loading and unloading of guanine nucleotides takes place in the Ras domain of G-proteins. The Ras domain essentially acts as a platform for nucleotide binding and also functions in intrinsic GTP hydrolysis (a slow process) (35). The G-protein nucleotide is tucked in between the switch I and switch II regions. The switch regions together with the P-loop or G1 interact with the phosphates of the nucleotide and coordinate with a magnesium ion. The magnesium ion and

phosphates are required for high affinity binding of the nucleotide to the G-protein (36). G-proteins have a high affinity for GDP, that in some cases can be in the picomolar range (high nanomolar range for Gα), which results in a very slow dissociation of GDP from the nucleotide binding pocket. GEFs function essentially to weaken the G-protein's affinity for GDP (36, 37) resulting in the loss of GDP. Cellular GTP is present at much higher concentrations in a cell, and thus, is readily available to bind to the G-protein resulting in dissociation of the bound GEF and activation of the G-protein (38). A generalized reaction scheme for GEFs is shown in figure 1.4.

The GEFs of Gα are typically membrane-bound GPCRs (171) that bind as far as 30Å away from the GDP binding region. This binding introduces a conformational change that triggers the release of GDP (4). The displacement of the α5 helix of Gα was shown to be 6Å toward the receptor breaking its contact with the α1 helix, while the helical domain separated away from the ras-like domain of Gα (4). The α1 helix of Gα contacts the N-terminal part of the α5 helix, helical domain, and GDP. Upon GPCR binding, α1-α5 contacts disintegrate disrupting the structural integrity of the α1 helix. As the α1 helix becomes flexible, contacts between α1, GDP, and the helical domain are lost, resulting in the loss of contacts with GDP resulting in decreased affinity for GDP (172).

While canonical regulation of guanine nucleotide exchange for G-proteins is typically thought of in regards to G-protein coupled receptors, receptor independent GEFs have been described over the past two decades. In contrast to GPCR mediated nucleotide exchange, receptor independent GEFs reside in the cytosol instead of being at the cellular membrane (37).Several research groups have worked to elucidate the mechanisms of GEF activity toward small G-proteins of the Ras family, where work has primarily focused on static binary complexes between GEFs and G-proteins (39, 40, 41, 42, 43). These studies have revealed that most of the catalytic domains of the various types of GEFs are structurally unrelated and interact very differently with the G-protein. For example, CDC25-HD of SOS was shown to contact the switch II region and pry open the G-protein nucleotide site using an α-helical wedge (39), while RCC1 used a β-turn on top of a β propeller for insertion into the nucleotide binding site (41). Despite the very different mechanisms between these GEFs, they follow a common theme of sterically impeding the magnesium binding site by changing the position of an alanine side chain in the DTAG motif of switch II or by inserting residues into the nucleotide binding site. Thus, the common action of GEFs has been proposed that they function to reconfigure the phosphate-binding site, while leaving the

base binding region mostly unperturbed, that ultimately results in the reduction G-protein's affinity for GDP (38).

Figure 1.4) The reaction scheme for a general GEF is shown. A G-protein bound to GDP interacts with a GEF to form a temporary complex comprised of the G-protein, GDP, and the GEF. The GEF induces conformational changes that results in the loss of GDP forming a binary nucleotide free complex comprised of G-protein and GEF. GTP, present at much higher concentrations in the cell, readily binds to the nucleotide free complex resulting in the dissociation of the GEF and activation of the G-protein.

1.5.1: Discovery of Ric-8 and its involvement in G-protein signaling

The Ric-8 (resistance to inhibitors of cholinesterase) gene was first identified in a *Caenorhabiditis elegans* ric genetic screen that was utilized to find mutants that exhibited reduced acetylcholine release. Acetylcholine is a neurotransmitter released by motor neurons of the nervous system to activate muscle contraction at the neuromuscular junction. *C. elegans* containing ric mutations are able to avoid the neurotoxic effects of the drug aldicarb, an inhibitor of acetylcholinesterase, that causes the toxic accumulation of synaptic acetylcholine (44). Later, it was determined in *C. elegans* that Ric-8 genes positively influenced synaptic neurotransmission and were found to include components of the G-protein signaling pathway, where the components included Gαq/egl-30, RGS/egl-10, and unc-13, a protein that regulates synaptic vesicle priming in response to diacylglycerol. The Ric-8 gene was found to encode a ~ 60 kilodalton protein that is often referred to as synembryn to reflect the dual roles of the protein in synaptic transmission and in early embryogenesis. Interestingly, ric-8 mutants were epistatic with the egl-30 gene which indicated the potential to be either acting upstream or in a parallel pathway with Gαq (45). In conjunction with being epistatic toward the egl-30 gene, later studies demonstrated that Ric-8 was also epistatic with Gαo, Gαs and adenylyl cyclase genes in *c.elegans* (46, 47, 48). The work performed in *C. elegans* demonstrated that the Ric-8 gene was involved in positively regulating three different G-protein signaling pathways.

1.5.2: Different Ric-8 isoforms interact directly with different classes of Gα subunits

There is only a single Ric-8 gene copy present in fungi (except *Saccharomyces cerevisiae)*, flies, worms, and slime molds, while two distinct genes of Ric-8 (Ric-8A and Ric-8B) are found in frogs,

mammals, and fish. Phylogenetic analysis between differing components of G-protein signaling pathways have suggested that Ric-8 mediated regulation of G-protein pathways appeared after GPCR signaling during eukaryotic evolution (49). The first real insights into Ric-8's function in regulating G-protein signaling pathways came from pull-down experiments and yeast two-hybrid screens, where Ric-8 was found to interact directly with Gα subunits (50, 51, 63). Interestingly, it was determined that Ric-8A and Ric-8B exhibited preference for differing Gα isoforms. Ric-8A shows a preference for interacting with Gαi, Gα12/13, and Gαq forms, while Ric-8B interacted with Gαs and Gαq. Ric-8A was demonstrated to interact with Gα bound to GDP relative to Gα bound to GTP (51).

1.5.3: Ric-8 acts as a molecular chaperone for Gα subunits *in vivo*

One of the essential cellular functions of Ric-8 is to regulate the proper expression levels of Gα subunits by acting as a molecular chaperone ensuring proper folding of Gα subunits. Indeed, the first observations that Ric-8 may function as a molecular chaperone for Gα subunits came as a result of disrupting the Ric-8 gene and RNAi treatment in *Drosophila* cells which resulted in a decrease of Gα subunits localized at the plasma membrane (51, 52, 53). These studies were further demonstrated again in multiple other model organisms ranging from filamentous fungi to mice and human cell lines (54, 55, 56). Most of these experiments have centered around genetic disturbances ranging from overexpression and reduction methods that include transgenic disruption, RNA interference, and isolation of hypomorphic alleles (57).

Ric-8 chaperone activity has been shown to occur at a very early stage in G-protein biosynthesis. One possibility for Ric-8's ability to regulate G-protein levels in a cell was at the transcriptional level. Though, this form of regulation by Ric-8 was discounted by a few studies, where it was observed that Ric-8A and Ric-8B knockouts in mice and Ric-8 knockouts in *neurospora* had no effect on the levels Gα transcript levels (58, 59). Studies in mouse Embryonic Stem cells (mES) containing Ric-8A knockouts indicated that newly synthesized Gαq and Gαi subunits were defective, where they were primarily located in the cytosol. Gα subunits residing the in the cytosol in the Ric-8A knockout mES cells were found to be degraded much more quickly than those of the wild-type mES cells (59). One study using a cell-free expression system containing endogenous Ric-8A or lacking endogenous Ric-8A showed that the Gα subunits were indeed misfolded and addition of Ric-8A to Ric-8A depleted extracts restored Gα function (60). Ric-8 was also found to inhibit polyubiquitination of Gα subunits (61, 62),

preventing degradation from the default ubiquitin proteasome pathway for misfolded proteins. Based on *in vivo* experiments performed for Ric-8, it is clear that the protein is required for proper regulation of G-protein levels and does so, by acting as a molecular chaperone for Gα subunits. Figure 1.5 displays the potential mechanism of Ric-8 induced chaperone activity.

1.5.4: Ric-8 functions as a cytosolic GEF toward Gα subunits *in vitro*

Ric-8 has been demonstrated to function biochemically as a GEF toward Gα subunits *in vitro*. Ric-8 binds to Gα:GDP and accelerates the release of GDP from Gα. Upon GDP release, Ric-8 acts to stabilize a nucleotide free intermediate of Gα. GTP binds to nucleotide free Gα that then results in the activation of Gα and the release of Ric-8. Thus, Ric-8 functions as expected for a GEF (38, 63, 64) (shown in Figure 1.5). Much work has been performed to understand the underlying mechanism of Ric-8 induced GEF activity toward Gα subunits, especially in the way of kinetic studies. Ric-8A GEF activity follows standard Michaelis-Menten kinetics to promote GDP release from Gα along with observed GTPγS binding (57, 65). Interestingly, steady-state GTP hydrolysis assays have shown that excess Ric-8 to Gα substrate are required to achieve to maximal activity. Ric-8 exhibits high-affinity for Gα nucleotide free states and thus, very high GTP concentrations are required to drive the steady-state GTPase assays in the forward direction, i.e. dissociation of Ric-8 from Gα. Due to the high concentrations of GTP required to drive the forward reaction, steady-state GTPase assays only provide a relative estimate of Ric-8's GEF activity. Ric-8 also has a much-lower and measurable activity toward Gα bound to GTP (57, 64). While work has been done to elucidate the kinetics of Ric-8, the physical mechanism of Ric-8 induced GEF activity has remained poorly characterized largely in part due to the lack of structural information pertaining to Ric-8 and a nucleotide-free Ric-8:Gα complex (57). However, very recently work has been performed structurally for Ric-8 and this will be discussed in a later section.

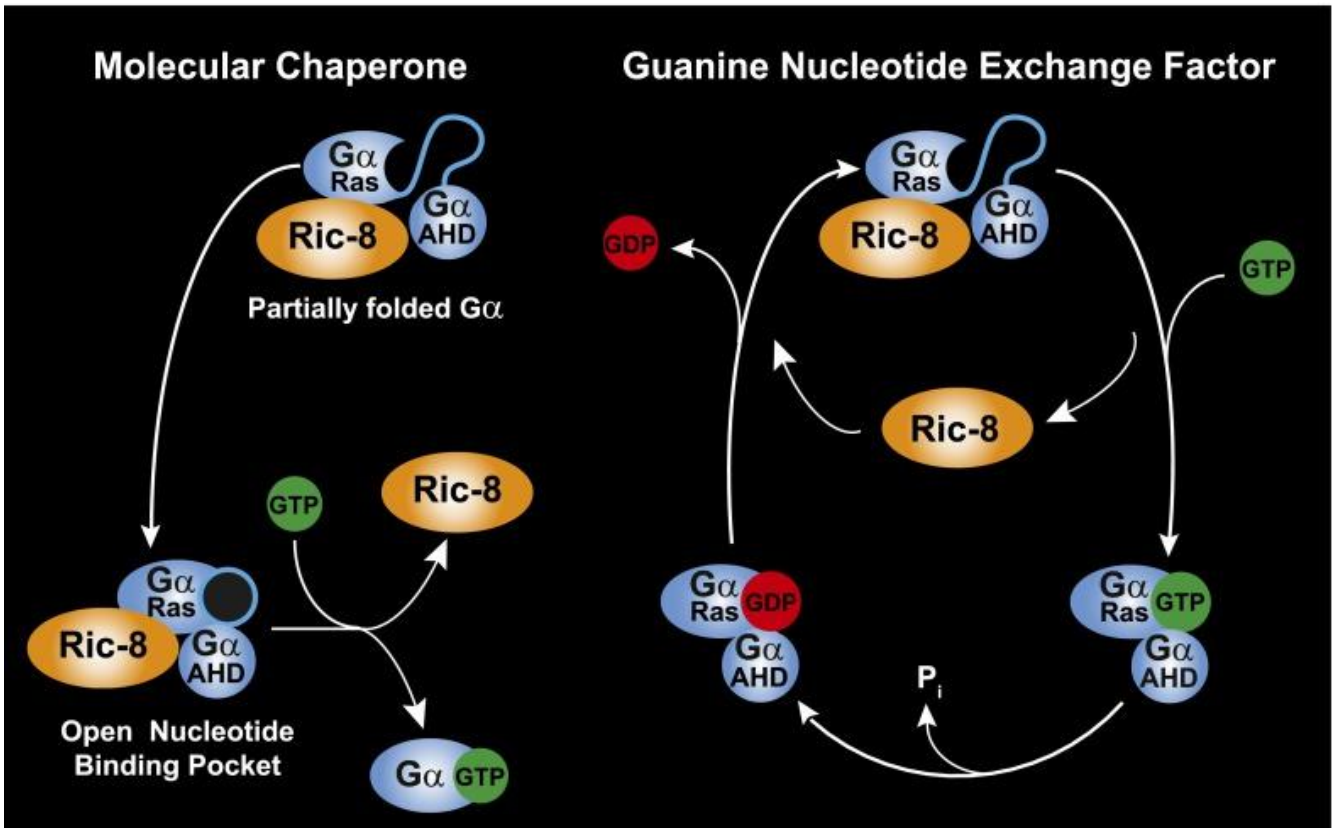

Figure 1.5) Models showing the Gα subunit molecular chaperoning and GEF activities of Ric-8. The domains on Gα are labeled as Ras for Ras-like and AHD for alpha helical domain. This figure was obtained from reference (57).

1.5.5: Casein Kinase II phosphorylation of Ric-8A enhances GEF and chaperone activity

Protein Kinase CK2 (formerly referred to as casein kinase 2) is a highly conserved serine and threonine kinase that recognizes the consensus sequence, (Ser-Xaa-Xaa-Acidic where the acidic residue may either be glutamate, aspartic acid, pSer, or pTyr), for phosphorylation of its subsrate (66, 67). CK2 is ubiquitously expressed in a variety of eukaryotic cells and is located in multiple cellular compartments such as the nucleus, cytoplasm, endoplasmic reticulum, and the golgi apparatus (68). CK2 consists of two 44 kilodalton catalytic subunits (CK2α) and two 26 kilodalton regulatory subunits (CK2β) where the kinase may function as a monomeric kinase or as a tetrameric complex (69). CK2 phosphorylates numerous cellular targets (70, 71) and as a result, is involved in multiple cellular processes such as cancer (72, 73), DNA-damage and repair (74, 75, 76), the ER-stress response (77), apoptosis (78, 79, 80), regulation of carbohydrate metabolism (81), and angiogenesis (82).

Ric-8A has been demonstrated to be phosphorylated by CK2 (83, 84). Using a collision-induced dissociation peptide analysis and mass fingerprinting software on CK2 treated E.coli produced Ric-8A indicated that Ser 435, Thr 440, Ser 522, Ser 523 and Ser 527 at the C-terminus were phosphorylated (84). Further, a flow cytometry interaction assay indicated that phosphorylated Ric-8A exhibited a 20-fold higher affinity for Gαi1 relative to unphosphorylated Ric-8A (84). Steady state GTPase assays indicated that *e.coli* purified full-length Ric-8A exhibited more GEF activity relative to unphosphorylated and insect-cell purified Ric-8A, which showed that phosphorylation at CK2 consensus sites activated Ric-8A (84). Interestingly, CK2 phosphorylated Ric-8A 1-493, truncated forty residues at the C-terminus containing only Ser 435 and Thr 440 present for phosphorylation, exhibited greater GEF activity relative to full-length Ric-8A (84). Unphosphorylated Ric-8A 1-493 was also shown to be more active than that of full-length Ric-8A (88). Phosphorylation of Ser 435 and Thr 440 residues by CK2 were further determined to enhance chaperone activity of full-length Ric-8A toward Gα subunits in a wheat germ extract translation and folding system (84). In contrast, CK2 phosphorylated Ric-8A 1-493 exhibited poorer chaperone activity relative to full-length Ric-8A (84). Together, this study indicated that CK2 phosphorylation may induce conformational changes that enhance Ric-8A induced GEF/chaperone activity. Potentially, Ric-8A enhanced GEF/chaperone activity could be a result of an electrostatic charge interaction between the phosphorylated C-terminus of Ric-8A and Gα subunit that enhances their interaction that otherwise would not be present in unphosphorylated Ric-8A.

1.5.6: Structural and functional characterization of Ric-8A and Ric-8A:Gα

Ric-8A's roles as a dual functioning protein acting as a GEF and a molecular chaperone has led to many questions regarding it's true physical mechanism of activity. While evidence has been presented that demonstrates both of these functions, structural support would be truly indispensable. Initially, only structural computational models were present for Ric-8A (84, 85), where Ric-8A was predicted to take on an entirely helical structure comprised of Armadillo (ARM) repeats. This was further confirmed by a 2.2 Å X-ray crystal structure of purified phosphorylated Ric-8A comprised of residues 1-452 (86) (Figure 1.6). Ric-8A 1-452 was found to take on a entirely superhelical fold comprising of nine repeat units (86). The repeats were not uniform and found to be either a two-helix-bundle of HEAT motifs or three-helix ARM motifs with the middle helix serving as a linker between the anti-parallel first and last helices of the bundle (86). Among helical repeat proteins, Ric-8A differs as it is comprised of both

types of repeat units (86, 87). While Ric-8A was phosphorylated, the last 28 residues were disordered and thus, the phosphorylation sites were not observed in the final crystal structure, although ordered sulfate ions in the crystal structure enabled prediction of potential Ric-8A binding sites for phosphorylated serine and threonine residues (86). Nonetheless, the structure provided useful insights into the structure of Ric-8A.

Structural and biochemical studies probing the interactions between Ric-8A and Gα has provided insights into the potential physical mechanisms of Ric-8A induced GEF/chaperone activity. The C-terminus of Gα has been shown to be a binding determinant of Ric-8A (88), where truncation of the Gα C-terminus inhibited binding of Ric-8A, furthermore, the C-terminus was also shown to be responsible for the preference of different Ric-8 isoforms toward differing classes of Gα. Very recently, X-ray crystal structures were determined for the apo form of Ric-8A 1-492 and a complex of Ric-8A 1-426 with a MBP-tagged C-terminal peptide of Gαt determined at 3.9 Å and 2.5 Å resolution, respectively (89) (Figure 1.6). The Ric8A 1-426:Gαt complex structure showed that the C-terminus of Gα binds along the concave surface of Ric-8A (89). Earlier hydrogen-deuterium Exchange-Mass Spectrometry (HDX-MS) analysis of Ric-8A and Gαi1, confirmed that Ric-8A interacted with the C-terminus of Gαi1 and identified switch I and switch II as potential binding sites (90). DEER (electron-electron double resonance) spectroscopy studies of the interaction of Ric-8A with Gαi1 indicated that the helical and Ras domain of Gai1 pivot as a far as 25Å apart upon Ric-8A binding (91). While these studies have identified the structure of Ric-8A and potential binding sites, it is imperative that a full complex structure of Ric-8 and Gα is determined fully using electron microscopy to understand the roles of phosphorylation, and to provide insights into Ric-8 GEF/chaperone activity.

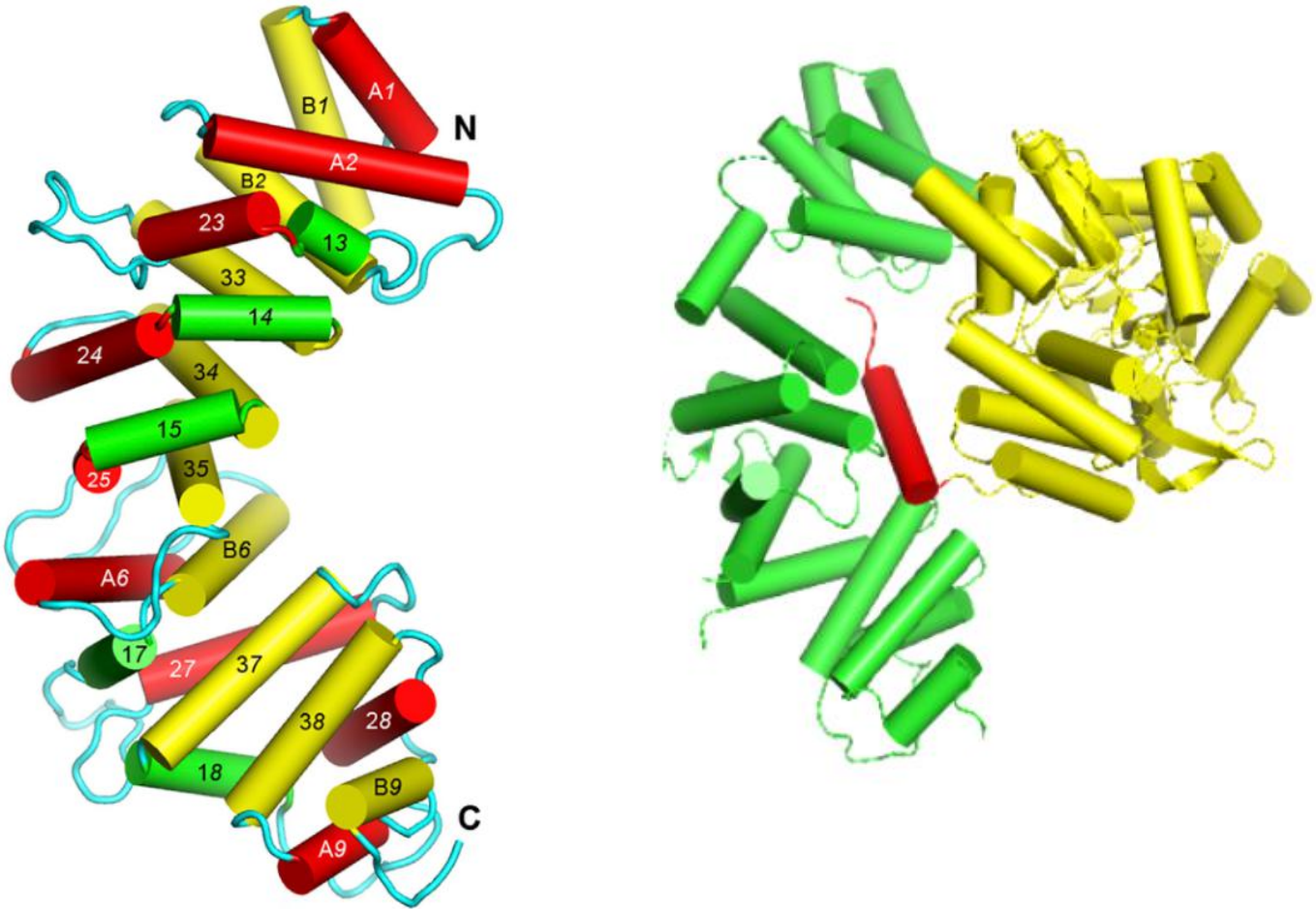

Figure 1.6) A) Crystal structures of Ric-8A 1-452. The N-terminus and C-terminus of the protein are labeled with an N and C. The cylinders represent α-helices. In red and labeled with A are the helices of the HEAT repeats or the second helix of an ARM triad. B helices of HEAT repeats or the third helix of an ARM repeat are colored yellow, and the first helices of ARM repeats are shown in green. Figure was obtained from reference (86). (PDB 6NMJ). B) The complex structure of Ric-8A 1-426 bound to a C-terminal peptide of Gαt with an MBP tag (PDB 6N85). The cylinders again represent α-helices. Green represents the structure of Ric-8A, while yellow represent the MBP-tag, and in red is the C-terminal peptide. The C-terminus of Gα interacts in the concave surface of Ric-8A. The figure was prepared in pymol.

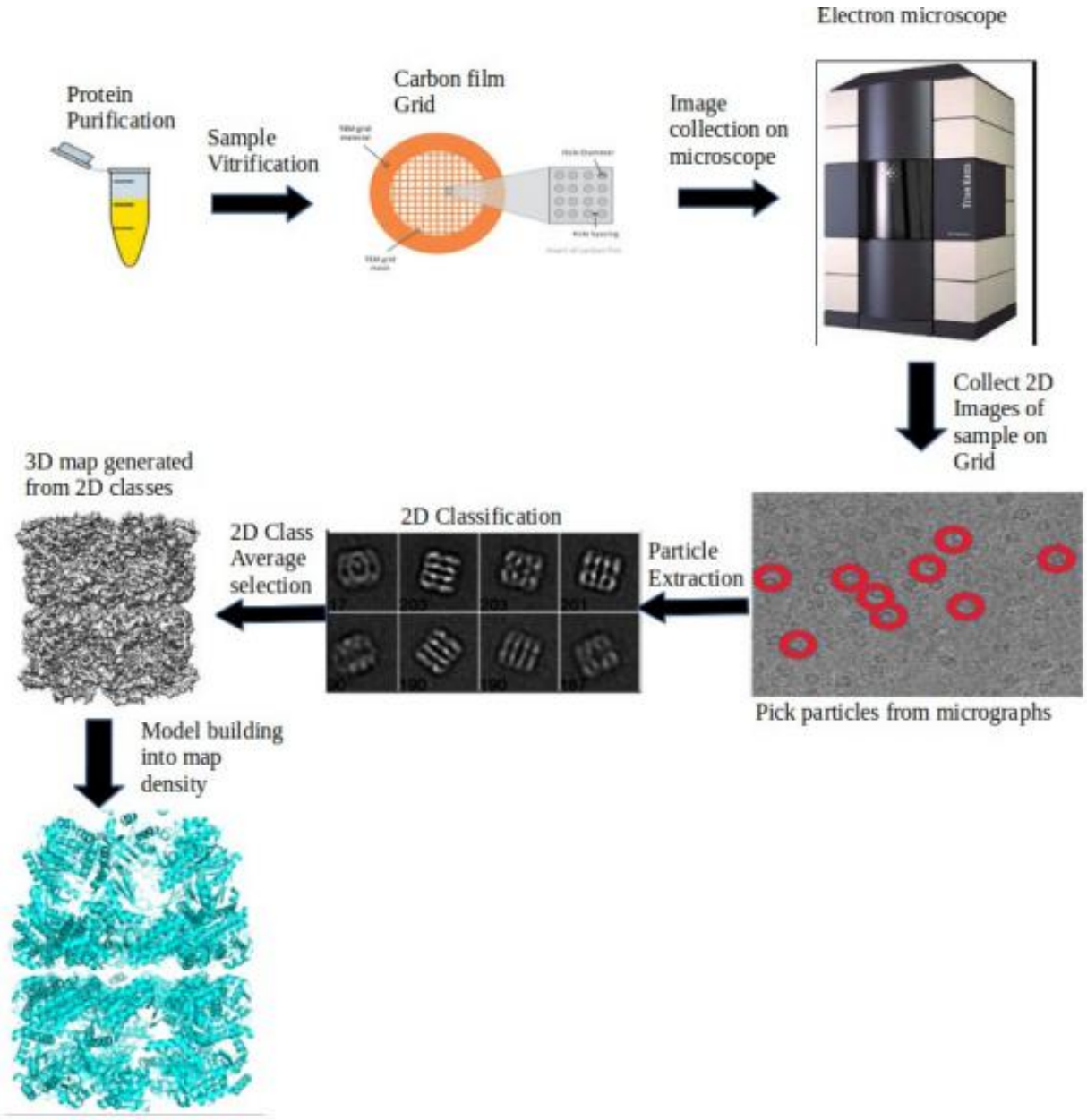

Figure 1.7.1) Single-particle cryo-EM workflow that leads to structure determination.

1.6: The aims and objectives of the study

In order to fully understand the physical mechanism of Ric-8A GEF/chaperone activity, it is very important to determine the complete structure of the Ric-8A and Gα complex. Although the structure of apo Ric-8A and Ric-8A bound to a Gα C-terminal peptide have been reported, many questions still remain unclear. In particular, no structural evidence presented thus far provides any insights as to how CK2 phosphorylation of Ric-8A enhances its activity as a GEF and a chaperone, the conformational changes that the helical domain undergoes when Ric-8A interacts with Gα, and how Ric-8A affects the nucleotide binding pocket of Gα that facilitates the release of GDP.

In this project, Ric-8A and Gαi1 proteins were purified from E.coli, mixed, and complexes were further purified for structural analysis by single-particle cryogenic electron microscopy (cryo-EM) while also being used in parallel for crystallographic studies. The complexes were stabilized using various combinations of nanobodies, small-camelid antibodies, that ultimately resulted in a high-resolution cryo-EM map. The EM map was further used for modeling and ultimately, provides insights into Ric-8A phosphorylation and Ric-8A induced conformational changes of Gα that facilitates GDP release.

1.7: Applicability of Cryogenic Electron microscopy in protein structure determination

X-ray crystallography has been the most widely used method of choice for determining protein structures with over 112,000 protein structures in the protein data bank (PDB) (92). To this day, X-ray crystallography is still the preferred method of choice for structure determination (92). Though, cryo-EM has recently undergone what was termed the “resolution revolution” as the method has improved enough to reach near-atomic resolution of macromolecular structures now rivaling that of X-ray crystallography (93, 94, 95). The recent progress of cryo-EM has largely been possible due to three significant improvements: direct electron detectors, improved sample preparation, and better data processing algorithm methods (96, 97, 98). These advancements have further resulted in the structure determination of high-resolution structures of very small proteins (less than 100 kilodaltons), which was previously not possible (99, 100, 101). Cryo-EM as an alternative method to X-ray crystallography, records digital micrographs of biological samples in fully hydrated and native states which provides many advantages over X-ray crystallography. A major bottleneck of X-ray crystallography lies in the necessity to crystallize the sample as proteins may be refractory toward crystallization, especially with membrane proteins and proteins that are inherently flexible (102, 103,

104). Cryo-EM circumvents the need to crystallize proteins, only requires a very small amount of protein (typically only a few µg), and conformational variability can be determined by computer processing (105, 106, 107).

1.7.1: A brief overview of the single particle cryo-EM workflow

Single-particle EM for a long period of time was typically performed using negative stain, though recently developed cryo-EM analytical techniques have become the main techniques for determining high resolution structures (107). Typically, the sample is purified to homogeneity at high concentrations and is immobilized onto a carbon film grid as a thin film solution, created by blotting. The sample is then vitrified using a refrigerant (liquid ethane) at -170^{o}C (108). The immobilized sample is imaged on an electron microscope, where low-dose electron beams at low temperatures are passed through the sample to obtain images of the sample without causing radiation damage (107, 109). Software packages such as EMAN2, Relion, and Cryosparc are used for particle picking, particle alignment, 2D class averaging, defocus determination, contrast transfer function (CTF) correction, particle alignment and classification to generate an initial 3D model and a refinement process to create a high-resolution 3D map of the protein particles at the molecular level (107, 110, 111). Software, such as Phenix, is subsequently used to build a model from the 3D map (112). The workflow for Cryo-EM is shown below in Figure 1.7.1.

1.7.2: Vitrification or freezing of samples in single-particle cryo-EM

Sample preparation in cryo-EM involves applying a protein sample onto a glow-discharged carbon film grid, blotting, and plunge freezing the sample into a cryogenic liquid, such as liquid ethane, to freeze the sample rapidly (114, 115). This method ensures that water molecules surrounding the sample remain in place, such that the sample is ideally in its native or hydrated state. Due to how rapid the sample is frozen, the water molecules do not have time to form an ordered crystalline lattice, and thus, the ice is vitrified or glass-like (116). By vitrifying the sample, the original structure is protected and thus, the micrographs of the sample are more representative of the sample. Vitrification of the sample also prevents the ice from absorbing electrons allowing for direct observation of the sample (116). The sample is also observed using a low-dose range of electrons (10-25 $e^{-}/Å^{2}$) that minimizes the radiation damage caused to the sample (117). Ice-thickness in cryo-EM is an important factor when considering

to collect high-resolution data. When the ice is thin, the number of electrons that are scattered is reduced, thus they are available to aid in image formation. Though, if the ice is too thin, then the particles of interest may not be present. Thick ice introduces more inelastic scattering and thus can affect the contrast of the image, and the visualization of the particles in the micrograph, resulting in low-resolution. Thick ice also contains particles that are located at different focal heights if the ice is much thicker than the particle size, then merging the data leads to a poor envelope function (118). Achieving optimal ice-thickness is a crucial bottleneck in obtaining high-resolution data in cryo-EM (119).

Another major bottleneck lies at the air-water interface during the vitrification step. As the sample on the grid is blotted, the protein sample is exposed to the atmosphere at a high surface-to-volume ratio. Macromolecules diffusing freely in such thin films have been proposed to collide with the air-water greater than 1000 times per second when the film is less than 100 nm thick (120, 121). This, in turn may cause the particles to adsorb to the air-water interface and become denatured immediately or for the particles to adopt a “preferred orientation”, where only one view is present in the micrographs (122, 123). Many methods have been shown to reduce the deleterious effects of the air-water interface. The addition of detergents to the sample before vitrification has been shown to be very beneficial for sample stability. The detergents are proposed to form a monolayer at the air-water interface that interacts with the proteins before they may arrive at the air-water interface (120). Immobilizing the protein sample onto an affinity support through the use of antibodies, affinity tags, and polylysine has been widely adopted (120, 124, 125). Changing the carbon film to a graphene type of film has proved useful for stabilization of cryo-EM samples from the air-water interface by providing an adherent surface for the sample. Though, using graphene supports come at the cost of introducing background noise, increased movement during imaging, potential contamination, and uncontrolled specimen-surface forces (126). Thus, overcoming the negative effects of the air-water interface is a major hurdle in achieving high-resolution data.

1.7.3: Principles of the transmission electron microscope

Transmission electron microscopes (TEMs) utilize high energy electrons (100 keV or higher) to form an image of a very thin object (127). Electrons are scattered very strongly by matter which occurs as either inelastic or elastic scattering. Elastic scattering occurs when there is no loss of energy from the primary incident electron. Elastically scattered electrons can change their direction, though the wavelength of these electrons do not change, as there was no energy loss. Inelastic scattering occurs when there is an interaction between matter and the electron, which results in the loss of energy from the primary incident electron. The energy may end up being transferred to the sample, and this loss of energy from the electron results in the electron having a longer wavelength (128).

The paths of the electrons in the microscope can be bent with magnetic lenses so that an image is created onto a viewing screen or on the detector. Electrons have a much shorter wavelength compared to visible light; thus, they are capable of achieving much higher resolution. The theoretical resolution achievable by an electron microscope is at 0.037 Å for electrons accelerated at 100 kV based on the de Broglie wavelength. Unfortunately, microscopes today have only been able to achieve resolutions in the range of 1-2 Å due to the aberrations in the lens of the microscopes (127). The microscopes are also kept in a vacuum to prevent the electrons from being scattered by air molecules. The issue with having to maintain a vacuum is the dehydration of the specimen, though this was solved recently. By keeping the sample frozen, at liquid nitrogen temperatures, the sample remains hydrated and the vapor pressure of water becomes negligible (127). The components of the microscope will now be discussed and are shown in Figure 1.7.2.

Cathode- Electrons are emitted from the cathode, which is kept at a high-negative value, while the rest of the microscope is kept at ground potential. Two types of cathodes are primarily used in electron microscopy which are field-emission guns (FEGs) and thermionic cathode. The primary mode of action for a thermionic cathode involves heating, where sufficient heat will result in the emission of electrons. Thermionic cathodes are typically hairpin-shaped wire comprised of tungsten. Lanthanum hexaboride is often used as a cathode as it has a low work function and results in more electrons being released and leads to much higher brightness relative to tungsten. A FEG emits electrons by lowering a potential barrier and the direction of the electrons is controlled by a strong electric field generated from the cathode tip (127).

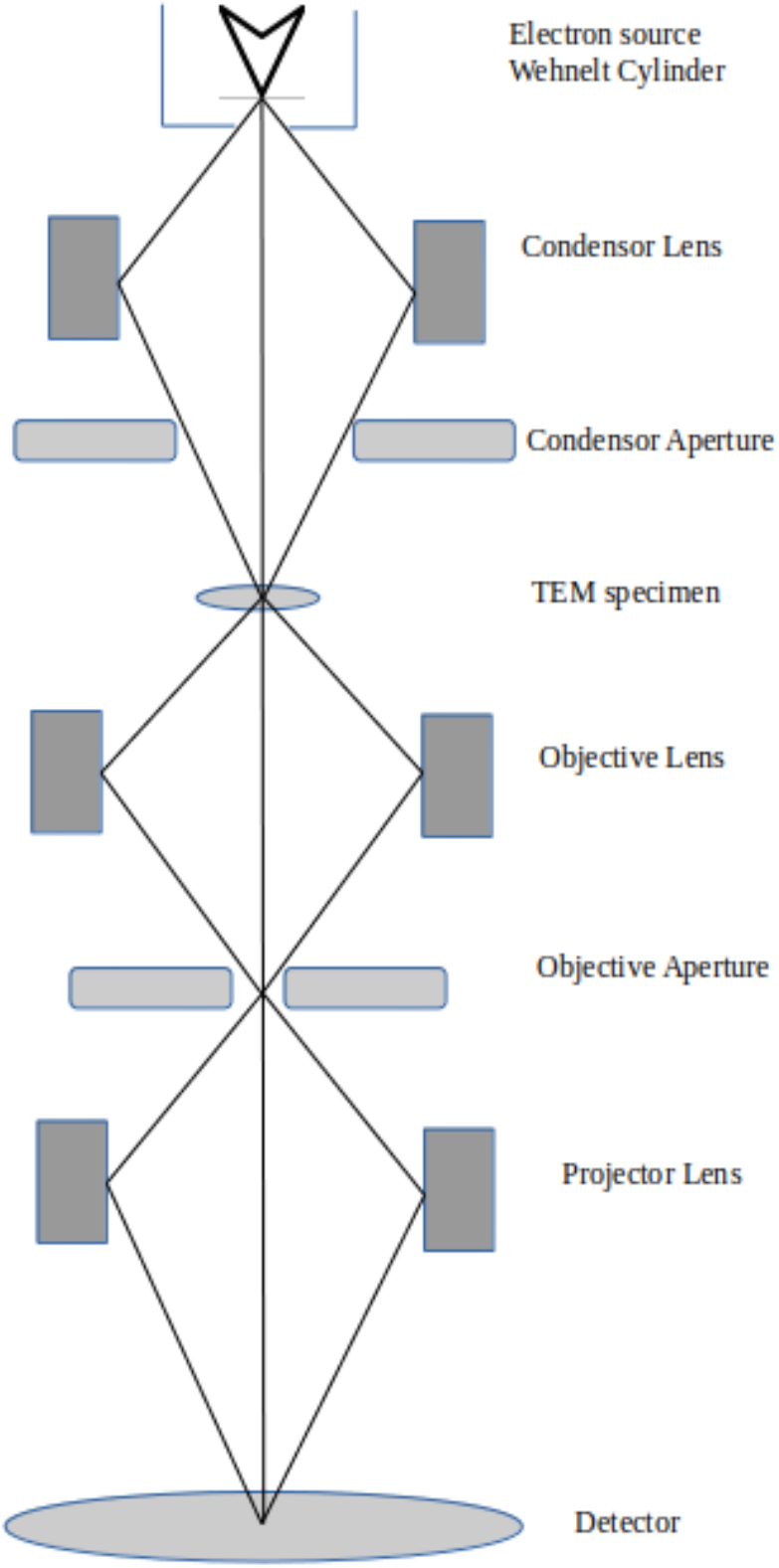

Figure 1.7.2) Diagram of various components of an electron microscope

Wehnelt cylinder- Surrounding the cathode is a cup-shaped electrode, with a 1-mm bore, where the electrons can exit. The wehnelt cylinder is kept slightly more negative than the cathode and specifically has a shape that allows the electrons to travel down the optical axis. This creates a space charge to build up as an electron cloud and at the tip of this cloud, lies the true source of the electrons being emitted (127).

Condensor lens- These lens function as part of the illumination system and control how the beam impacts the sample. The condensor lens primarily controls the spot size, the physical size of the beam on the specimen, and the angle of the beam required for convergence which also determines the coherence of the illumination. Most microscopes contain two condensor lens, such as the case with Talos Artica microscope, and some microscopes may contain three condensor lens as is the case with a Titan Krios microscope. (127, 129). Typically, the C1 lens is situated under the Wehnelt cylinder. The spot size of the image is primarily controlled by the current generated in the lens (127).

Objective lens: The objective lens is the first image forming lens in the microscope and subsequently, determines the quality of the final image obtained. Parallel beams are focused on the back focal plane and beams are scattered at the same angle at the same point. This results in a diffraction plane being generated in that same plane. An objective lens aperture portion, that resides in the back focal plane, determines what portion of the scattered rays participate in image formation. Phase contrast in electron microscopy is an important in high-resolution cryo-EM and results from the interference of unscattered and elastically scattered electrons that have endured a phase shift due to defocusing and wave aberrations (127). There are multiple types of objective len spherical aberrations that can occur in the lens of the microscope which include third-order aberrations, chromatic aberration, and axial astigmatism. Beams experiencing third-order aberrations the focal length is less than for those parallel to the optical axis. Axial astigmatism is typically described as an unroundness of the lens magnetic field, and typically depends on the features of the specimen depends on their orientation in the specimen plane. Axial astigmatism is typically corrected for with special corrector elements located underneath the objective lens. Chromatic aberrations determine how the lens focuses electrons with different energies. The electrons may differ slightly in energies because of high voltage fluctuations or have differing energies due to scattering. Microscopes are stable and thus the first factor is negligible.

Luckily for the latter, a chromatic aberration constant ensures that electrons undergoing energy less are out of focus relative to zero-loss electrons (127).

Intermediate Lens- These lenses are located between the objective and projector lens. The strength of these lens can be changed to produce magnifications in a wide range between 500 and 1 million. In structure determination, a typical range for magnification is from 35,000 to 60,000 (127).

Projector Lens- These are the final lens that project the image onto the screen or detector of the microscope. Special magnetic shielding is used around the EM column between the projector lens and screen to prevent stray fields from distorting the image as the final image is typically quite large (127).

Fluorescent screen- The fluorescent screen in the microscope is used for direct viewing of the specimen, when the screen is put directly into the image plane. The screen is a metal plane coated with a thin layer of fluorescent material that converts the electrons into bursts of light (127).

Detectors: Two types of detectors are in used in cryo-EM, which include direct electron detectors and charge-coupled devices (CCD). Direct electron detectors will be discussed in detail in a later section. CCD cameras are comprised of photosensitive silicon diodes that are optically coupled with a scintillator. The optical coupling is usually achieved with fiber optics or sometimes with a glass lens with a large numerical aperture. The scintillator converts the energy from the electron into a local light signal. The signals that are received from the electrons are read out and integrated over a period of time to form a digital image that is stored on the computer (127).

1.7.4: Direct electron detectors

Cryo-EM greatly advanced in its resolution capabilities with the creation of direct electron detectors over the use of typical CCD cameras (130, 131). Two parameters are discussed when describing the performance of detectors which is the Detective Quantum Efficiency (DQE) and the Modulation Transfer Function (MTF) (131). The DQE is measured as a ratio of the signal to noise ratio that is output by the detector divided by the ratio of the signal to noise that is input into the detector. The DQE effectively measures how the physics of the mechanism for signal conversion in the detector degrades the original signal in the image (131). DQE can be plotted against the spatial frequency and a DQE of

unity indicates a perfect detector that does not add any noise. The pixel spacing in a detector fixes the maximum spatial frequency in an image that can be recorded by the detector, especially since the shortest wavelength has to be sampled at least twice (131). This effectively describes the Nyquist cut-off frequency as 1/(2*pixel_spacing). The MTF describes how strongly the various spatial frequencies in the image up to the Nyquist frequency are recorded. The MTF is set by the pixel size and other factors, such as the point spread function which describes how electrons are spread on the surface of the detector. The MTF is plotted against as a function of spatial frequency, where a value of unity implies that perfect retention of the relative amplitude of the spatial frequency (131).

CCD cameras only record 2D projections of 3D objects in a micrograph in a given exposure (132). In contrast, direct electron detectors have the ability to collect to record high frame rate movies and also exhibit a much a much higher DQE relative to CCD cameras (131). The ability to record movies allows the effect of beam-induced specimen movement and image blurring to be reduced by the alignment of movie frames and the ability to appropriately weigh individual frames. This effectively increases the sharpness of the images maximizing the signal to noise ratio (133, 134, 135, 136, 137). The improved motion corrected images then make a more accurate determination of the position and orientation of the particle. This results in a 3D map at higher resolution, which provides a better target for orientation determination in an iterative manner (131). Thus, direct electron detectors were pivotal in the advancement of cryo-EM. This has resulted in an increase in popularity for cryo-EM and has made the method more competitive with X-ray crystallography.

1.7.5: Single-particle reconstruction processing work-flow in cryo-EM

To obtain enough detailed structural information, a large amount of data must be collected over several days. Furthermore, the processing of such data is also a very time-consuming process. Data collection have improved drastically recently and now researchers are capable of collecting data automatically using a range of computer software packages such as Leginon, SerialEM, and EPU (138, 139). Several software packages are also available for processing single-particle cryo-EM data (Relion, EMAN2, Cryosparc) where 3D models are reconstructed from 2D micrographs with the noise level reduced to the lowest possible level (140, 141, 142). In single-particle cryo-EM, the determination of 3D maps uses a single-particle reconstruction algorithm (143, 144, 145). The procedure begins with collecting raw movies from holes containing the particles of interest. The raw images are then corrected for

motion using the software Motioncor2 generating aligned images termed micrographs. The CTF of the micrographs are then corrected, using software such as CTFFIND4 and GCTF, which uncovers undistorted information that is buried in the noise (127, 146, 147). Single-particles are then selected from the micrographs using various software packages and extracted for further processing. The extracted particles are then classified into different groups based on similarities of their projections, and are representative of various angular views of a 3D object. These projections can then be used to estimate and iteratively reconstruct the 3D model of the object (145). Classification of particles based on this method is useful in detecting multiple conformations of chemically identical macromolecules or complexes and thus, multiple 3D models can be generated from one data set. Individual 3D classes can be subsequently refined to a higher-resolution using the auto refine procedure in various software packages. This procedure typically uses the so-called gold-standard Fourier Shell Correlation (FSC) calculation for a resolution estimate that avoids overfitting of the data (150). The FSC can be thought of as a function of consistency. The FSC is computed by splitting the particle data set in two sets, generating a reconstruction from each, and then computing the correlation coefficient between the Fourier transforms of each as a function of spatial frequency (151). The final refined density obtained is further filtered at the correct resolution with a mask around the density that removes the solvent noise to further increase the resolution of the map (152). The density then is further sharpened to an automatically estimated B-factor (153). The B factor or also known as the temperature factor describes the attenuation of structure factors by the thermal mobility of the molecule atoms. Figure 1.7.3 displays a flow chart for processing single-particle cryo-EM with the software package Relion.

1.7.6: CTF correction

The contrast transfer function (CTF) is a Fourier-based description of the image parameters along with how the image of an electron microscope is affected by the lens system. The CTF is affected by adjustable parameters during operation of the microscope such as defocus, astigmatism, and the acceleration voltage. The CTF may also be affected by fixed parameters such as lens aberrations and beam coherence (148). The CTF is an oscillating function, and fluctuates around zero contrast, modulating the amplitude and reversing the phase for some frequency intervals. The CTF also contains an envelope that results in a weakening of the signal with increasing spatial frequency (149). For high-

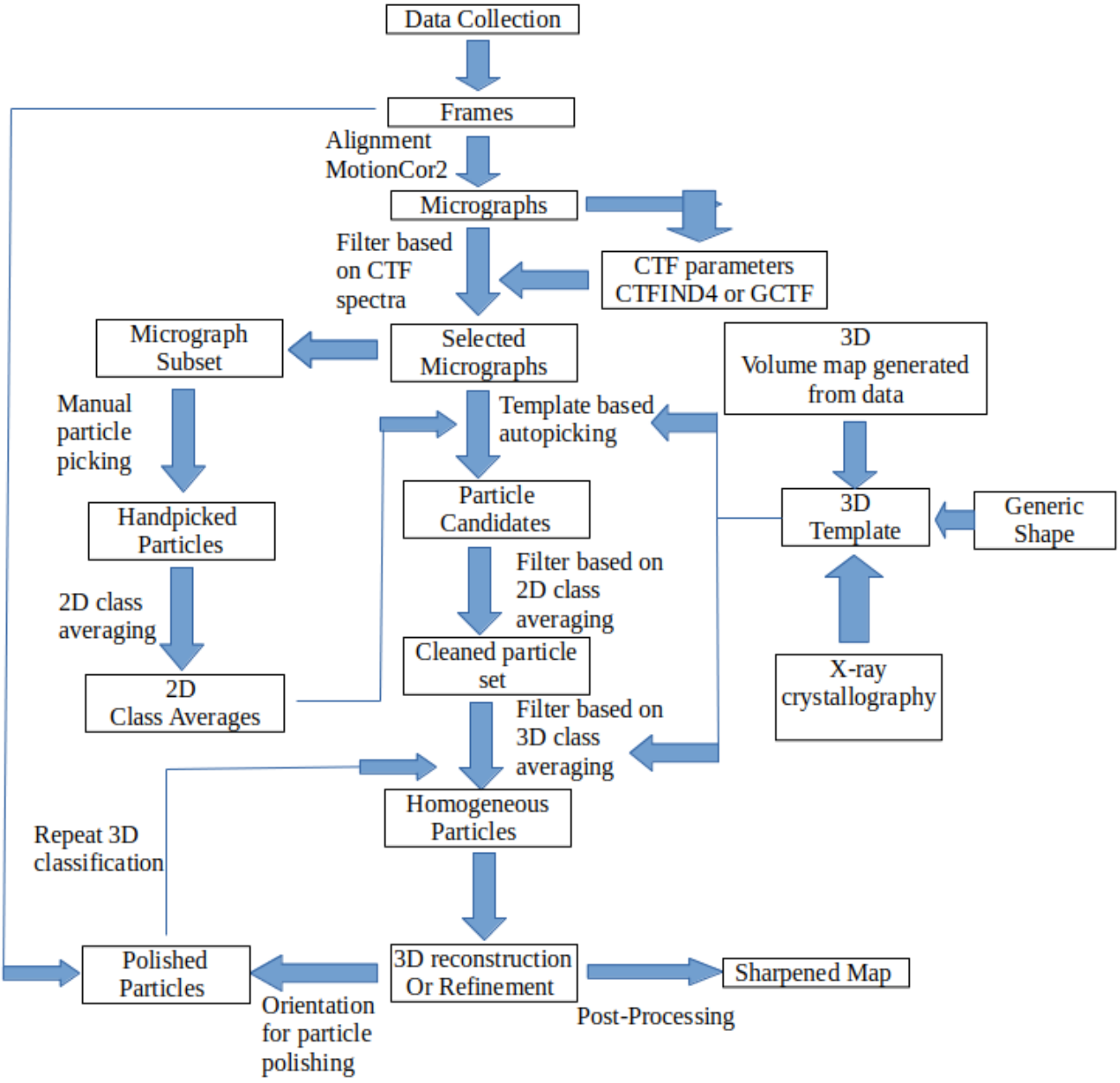

Figure 1.7.3) Displays the typical single-particle processing workflow for the software Relion. 2D classifications and 3D classifications generated in the work-flow can be used as templates for particle picking. Individual 3D classifications can also be used for refinement to high-resolution. After “polishing particles” it is recommended to redo the 3D classification and/or refinement.

resolution cryo-EM, the CTF must be applied and this is why this is performed in single-particle cryo-EM processing. For the work presented here, the CTF was applied using the CTFFIND4 program to determine the applied defocus and beam astigmatism. The CTF parameters are determined by computing the maximum cross-correlation between the averaged power spectrum of the image and a set of theoretical CTF spectra (146).

1.7.7: Particle polishing in the Relion Software

During the processing of cryo-EM data, large movements on the level on the entire micrograph are corrected for. However, the individual particles in the micrographs will show some trajectory or individual motions that cannot be corrected for at the level of the micrograph. In the Relion software, there is a particle polishing algorithm that tracks the individual particle motion trajectories which are subsequently fitted to a linear trajectory (154). Furthermore, per-frame B-factors and linear intensity factors are estimated by comparing the reconstructed half-maps from individual frames to the full-frame maps to account for accumulating radiation damage during data acquisition (133). This then generates what is termed “shiny” particles that have a much higher signal to noise ratio, which improves the accuracy of image alignment and typically results in higher resolution. These shiny particles are reconstructed with the spatial frequency contribution from each frame according to the radiation damage. It is typically recommended in the Relion software that the shiny particles are subjected for further 3D classification and refinement to obtain a higher resolution map.

1.7.8: The use of antibodies in single-particle cryo-EM

Monoclonal fragments antigen binding (Fabs) are useful tools in structural biology and have been used widely in protein X-ray crystallography to facilitate crystallization of proteins (155) by forming rigid, stable complexes and acting as a scaffold for crystal lattice contacts. Furthermore, Fabs have been widely used in single-particle cryo-EM to overcome size-limitations (156, 157) and to break symmetry or add features to the target protein facilitating image alignment during 2D and 3D classifications (158). Fabs are ~50 kilodalton antibody fragments composed of one constant domain and one variable from both heavy and light chains. The fragment retains full antigen binding capacity through its variable domain (156, 159, 160). In this project, nanobodies were employed to stabilize the Ric-8A:Gα complex to prevent dissociation during vitrification, provide features for image alignment and to stabilize flexible portions of the complex for single-particle cryo-EM structure determination.

Nanobodies are the small, stable 15 kilodalton single domain fragments that harbor the full antigen-binding capacity of the original heavy chain-only antibodies that naturally occur in camelids (161, 162, 163).

Nanobodies exhibit many advantages over the traditional use of Fabs in structural biology. For example, nanobodies are encoded by single-gene fragments, and thus, do not require enzymatic cleavage to generate the fragment of interest (161, 164). Due to the small size of nanobodies, they have access to small clefts or cavities to proteins that are not accessible to traditional to antibodies. Unlike Fabs, nanobodies can also be expressed in the periplasmic space of bacteria making purifications much easier (165, 166, 167, 173). Using various combinations of these nanobodies, we were able to stabilize the Ric-8A:Gα to facilitate structural studies using single-particle cryo-EM.

Chapter 2.
Materials and Methods.

All chemicals and reagents used in this study were supplied by Sigma-Aldrich, Fisher Scientific, Melford, and ForMedium. Buffers were filtered using using a .22-micron vacuum filter before use in FPLC (Fast Protein Liquid Chromatography) runs.

2.1.1: Media Recipes

Escherichia Coli strains were grown in standard laboratory media.

Table 2.1.1: Media Recipes

Medium	Ingredients and Methods
Luria Broth (LB)	10 g tryptone, 5 g yeast extract, 10 g NaCl, in 1L of miliQ H_2O. Approximately 2% w/v agar for Agar plates but not growth media. Autoclaved for sterility and stored at room temperature. Media was not stored for no longer then one week and plates were stored for up to one month.
Luria Broth (LB) + Carbencillin (Carb) or Ampicillin (Amp)	Ampicillin or Carbenicillin was added to autoclaved LB at 100 µg/mL immediately prior to inoculation
Terrific Broth (TB)	20 grams of tryptone, 24 grams of yeast extract, 4 mL of 100% glycerol, 2.31 g of KH_2PO_4, 12.54 g of KH_2PO_4 in 1L of miliQ H_2O. The media was autoclaved and stored at room temperature. Media was stored for up to one week.
Terrific Broth (TB) + Carb or Amp	Amp or Carb was added to autoclaved TB at 100 µg/mL immediately prior to inoculation.
Terrific Broth + Kanamycin (Kan)	Kanamycin was added to autoclaved TB immediately at 50 µg/mL prior to inoculation.
Terrific broth + Amp/Carb + Kan	Kan and Amp was added to autoclaved TB immediately at 50 µg/mL prior to inoculation.
Terrific broth + Amp + Glucose + $MgCl_2$	Amp was added to autoclaved TB immediately at 100 µg/mL prior to inoculation. Glucose was sterile filtered and added at 0.1% final concentration. $MgCl_2$ was added to final concentration of 1 mM.

2.1.2: List of *e.coli* Strains

Strain	Genotype	Source
BL-21 (DE3) RIPL	E. coli B F– ompT hsdS(rB– mB–) dcm+Tetrgalλ(DE3) endA Hte [argU proLCamr] [argU ileY leuW Strep/Specr]	Agilent Technologies
BL-21 (DE3)	E. coli B F– ompT hsdS(rB– mB–) dcm+Tetrgalλ(DE3) endA Hte	Agilent Technologies
JM109	endA1, recA1, gyrA96, thi, hsdR17 (rk–, mk+), relA1, supE44, Δ(lac-proAB), [F´ traD36, proAB, laqIqZΔM15	Promega
WK6	Δ(lac-proAB), galE, strA, nal, F'[lacIqZΔM15, proAB]	Invitrogen
TOP10	F– mcrA Δ(mrr-hsdRMS-mcrBC) φ80lacZΔM15 ΔlacX74 recA1 araD139 Δ(ara-leu)7697 galU galK λ– rpsL(StrR) endA1 nupG	Thermofisher Scientific
DH5α	F– φ80lacZΔM15 Δ(lacZYA-argF)U169 recA1 endA1 hsdR17(rK–, mK+) phoA supE44 λ– thi-1 gyrA96 relA1	Thermofisher Scientific

E.coli strains (BL-*21* (DE3*)* RIPL, BL-21 (DE3), JM109) were used as hosts for protein expression plasmid vector*s.* DH5α and TOP10 strains were used for plasmid amplification.

2.1.3: E.coli strain preservation

E.coli competent c*ell* strains were amplified from company stock using a chemical competency protocol. 10 µL of of company stock was added to 10 mL of LB media and grown overnight at 37ºC. The following day, the 10 mL overnight culture was added directly to 100 mL of LB media and grown to optical density (OD) of 0.5, where the cells were kept on ice for 5-10 minutes. Cells were collected at 5,000 x g centrifugation and the supernatant was discarded. The cell pellets were resuspended with 40 mL of TfbI buffer (refer to Table 2.1.3). Cells were incubated for 15 minutes on ice and collected at 2,000 x g centrifugation. The supernatant was discarded and cells were suspended with 4 mL of TfbII buffer (refer to Table 2.1.3) for 15 minutes on ice. The cells were aliquoted in 50 µL aliquots and snap frozen in liquid nitrogen. The cells were stored at -80^{0}C.

2.1.3: TfbI and TfbII recipes for chemical transformation of E.coli

TfbI (transformation buffer I)	
Components	Final Concentration
potassium acetate	30 mM
$RbCl_2$	100 mM
$CaCl_2$ -$2H_2O$	10 mM
$MnCl_2$	50 mM
Glycerol	15% v/v

TfbII (transformation buffer II)	
Components	Final Concentration
MOPS	10 mM
$CaCl_2$ -$2H_2O$	75 mM
$RbCl_2$	10 mM
Glycerol	15% v/v

TfbI is pH 5.8 with dilute Acetic Acid. TfbII is pH 6.5 with dilute NaOH. Buffers are sterile filtered and stored at 4^0C.

2.2: Plasmid protein constructs

Plasmid encoding containing the proteins of interest were made by others in the lab. Amplification of these constructs were first transformed (described later) into DH5α and Top10 competent cells. A single colony was isolated and inoculated into 5 mL of LB containing either Kan or Amp. The media and cells were incubated overnight at 37^0C in a shaking incubator at 180 rpm. Plasmids were extracted using the QIAprep Spin Miniprep Kit (Qiagen). The purification procedure was provided by the manufacturer. After purification, the concentration of the DNA was quantified using a NanoDrop 8000 (Thermo Scientific). The plasmids were sequenced using MW eurofins and stored at -20^0 C after confirmation of the correct sequence. Table 2.2 lists the name of the vectors used along with the gene and protein names of the insert in the vector.

2.2: Lists of Plasmid protein expression constructs

Plasmid	Protein	Gene/allele	Expression Tag	Cleaveable
PDEST 15	DeltaN31 Gαi1	Gnai1	N-terminal GST	yes
pET-28a	Ric-8A (1-491)	Ric8a	N-terminal His	yes
PDEST15	Gαi1 W258A	Gnai1	N-terminal GST	yes
pMESy4	Nanobodies	N/A	N-terminal His	no
PQE60	Gαi1W258A	Gnai1	N-terminal His	no
pBB131	N-myristoyl-transferase	M153_2200036954	N/A	N/A
PDEST15	Ric-8A Full-length	Ric8a	N-terminal GST	yes

2.2.1: Transformation of *e.coli*

50 µL aliquots of competent cells were pulled from the -80^0 C freezer and thawed on ice. 1-5 µL of plasmid at 60-100 µg/mL was added to the cells and incubated on ice for 30 minutes. The sample was then heated at 42^{0}C for 45 seconds in a water bath. The sample was then mixed with 400 µL of LB broth and was grown in a shaker at 37^{0}C shaking at 180 rpm for one hour. 150 µL of the sample was plated onto an LB agar plate containing the appropriate antibiotics. The plates containing the sample were allowed to grow overnight at 37^{0}C in an incubator and stored the next day at 4^{0}C for at most one month.

2.3: Protein purification of each component

2.3.1: Purification of pET28a Ric-8A 1-491

Plasmid harboring Ric-8A 1-491 was transformed into BL-21 (DE3) RIPL competent cells and plated onto Kan plates. Single or multiple colonies from the plate were inoculated into LB media containing 50 µg/mL of Kan and grown overnight at 37^{o}C in a incubator shaking at 180 rpm. Cells were recovered by centrifugation at 8,000 rpm. The cells were resuspended in TB media containing 50 µg/mL of Kanamycin and was used to inoculate 1.0 L of media in 2.79 Liter shaker flasks. The growths were grown to an OD of 0.6-0.8 at 37^{0}C at 200 rpm. Once the OD was reached, the temperature was reduced to 20^0 C and the cells were induced with IPTG at a final concentration of 50 µM. The cells were harvested 16 hours' post-induction by centrifugation at 5000 x g and pellets were stored at -80^0 C.

Pellets were removed from the -80^0 C and thawed on ice. The cell paste was resuspended in 75 mL of lysis buffer (refer to Table 2.3.1) per 12 g of cell paste and lysed using a cell disruptor. The suspension was centrifuged at 18,000 rpm in an SS34 rotor (Sorvall) for 30 minutes at 4^0 C. The supernatant was loaded onto an IMAC column at 2 mL of packed resin per 1L of growth. The column was washed with lysis buffer until a bradford assay indicated that contaminants were no longer washing off the column. Ric-8A was eluted with lysis buffer containing 300 mM imidazole. The eluted protein was subject to dialysis in a SnakeSkin pleated dialysis tubing (10K MWCO, ThermoScientific) to remove the imidazole and salt for anion exchange chromatography. TEV protease was added at a ratio of 1 mg to 20 mg of Ric-8A overnight at 4^0 C to remove the his-tag and reverse IMAC chromatography was used to remove uncleaved Ric-8A and TEV protease. Cleaved Ric-8A was applied onto a Fast Flow Hi-Trap Q column on a AKTA FPLC system and eluted with a NaCl gradient of 0-500 mM over 50 mL. Fractions containing Ric-8A were collected, pooled and concentrated to 10 mg/mL (Milipore Centricon, 30K MWCO) for size-exclusion chromatography on a HiLoad Superdex 200 pg column. Ric-8A was aliquoted, snap frozen in liquid nitrogen, and stored at -80^0 C for further studies. Yields typically were in the range of 70-100 mg of protein per liter of cell growth.

Table 2.3.1: Ric-8A 1-491 purification buffers

Buffer	Ingredient and methods
Lysis/Wash	50 mM Tris, pH = 8.0 with HCL, 250 mM NaCl, 5% Glycerol, 2 mM BME, 2 mM PMSF
Elution	50 mM Tris, pH = 8.0 with HCL, 250 mM NaCl, 5% Glycerol, 2 mM BME, 2 mM PMSF, 300 mM Imidazole
Dialysis/QA buffer	50 mM Tris, pH = 8.0 with HCL, 2 mM BME
QB buffer	50 mM Tris, pH = 8.0 with HCL, 2 mM BME, 500 mM NaCl
Size-Exclusion Buffer	50 mM Hepes, pH = 8.0 with NaOH, 150 mM NaCl, 1 mM TCEP

2.3.2: Purification of PDEST15 Ric-8A Full-length

Plasmids harboring Full-length Ric-8A were transformed into BL-21 (DE3)-RIPL competent cells onto LB Amp plates. Single or multiple colonies were inoculated into LB media containing 100 µg/mL of Amp and grown overnight at 37^0 C in an incubator shaking at 180 RPM. Overnight growth was centrifuged at 8,000 rpm and cells were resuspended in LB media containing 100 µg/mL of Ampicilin for inoculation into 2.79-liter shaker flask growths containing LB media. Cells were grown to an OD of 0.6-0.8 at 37^0 C in an incubator shaking at 200 rpm. The temperature was reduced to 20°C and the cells were induced with 70 µM IPTG overnight. Cells were harvesting by centrifugation at 8,000 rpm and stored at -80° C.

Cells were thawed on ice and resuspended in lysis buffer at 50 mL per liter of cells. The cells were lysed using a cell disruptor and the soluble fraction was obtained by centrifugation at 18,000 rpm at 4^0 C. The supernatant was applied directly over 5 mL of packed GST beads overnight at 4^0 C using a peristaltic pump and were washed with lysis buffer until a bradford assay indicated that no more unbound protein was eluting off the column. Tev protease containing 150 mM NaCl was added to the GST beads at a ratio of 1:20 overnight for removal of the GST tag from Ric-8A. Digested Ric-8A was eluted with QA buffer and was subsequently purified using anion exchange (SourceQ 15 mL column from Resource) with a gradient of 100 mM NaCl to 500 mM NaCl over 30 mL. Fractions containing Ric-8A were pooled and further purified with size-exclusion to remove aggregates. Purified proteins were snap frozen in liquid nitrogen and stored at -80^0 C for further use.

Table 2.3.2: Ric-8AFull-length purification buffers

Buffers	Ingredients and Methods
Lysis/Wash	50 mM Tris, pH = 8.0 with HCL, 250 mM NaCl, 5% Glycerol, 2 mM BME, 1x PTT/LL, 1 mM EDTA pH = 8.0
QA buffer	50 mM Tris, pH = 8.0 with HCL, 100 mM NaCl, 2 mM BME, 1x PTT/LL, 1 mM EDTA pH = 8.0
QB buffer	50 mM Tris, pH = 8.0 with HCL, 500 mM NaCl, 2 mM BME, 1x PTT/LL, 1 mM EDTA pH = 8.0
Size-exclusion	50 mM Hepes pH =8.0 with NaOH, 150 mM NaCl, 1 mM TCEP

2.3.3: Purification of PDEST15 Gαi1W258A and DeltaN31 Giα1

Plasmids harboring PDEST15 Gαi1W258A or DeltaN31 Gia1 were transformed into BL-21 (DE3) RIPL competent cells and were plated onto LB Amp plates in an incubator at 37^0 C overnight. Single or multiple colonies were inoculated into LB media containing 100 µg/mL AMP and were grown overnight in an incubator at 37^0C shaking at 200 rpm. Cells were isolated by centrifugation at 8,000 rpm at 4^0C and resuspended in TB media containing 100 µg/mL Amp. Suspended cells were inoculated into 2.79 L shaker flasks containing 1.0 L of TB media with 100 µg/mL Amp. Cells were grown in a incubator at 37^0 C shaking at 200 rpm until an OD of 0.6-0.8 at which point, the temperature was reduced to 20^0 C and cells were induced with 50-70 µM IPTG. The cells were grown overnight and harvested by centrifugation at 8,000 rpm at 4^0 C and pellets were stored at -80^0 C.

Cells were thawed and suspended in lysis buffer at 50 mL per Liter of cells. Suspended cells were lysed with a cell disruptor and the soluble fraction was obtained by centrifugation at 18,000 rpm at 4^o C. The soluble fraction was applied onto 5 mL of packed GST beads and was incubated for 30 minutes to overnight with gentle shaking to enhance binding. The column was washed until a bradford assay indicated that all unbound protein was washed away. To remove the GST tag, TEV protease was added at a ratio of 1:20 to the GST beads overnight at 4^0 C. Cleaved Gα was eluted with QA buffer for further purification on an anion exchange column. Eluted Gα was purified using anion exchange chromatography with a gradient of 0 mM to 500 mM NaCl over 50 mL. Fractions containing Gα were pooled and purified using size-exclusion chromatography to remove aggregates. Purified Gα was stored in size-exclusion buffer containing 10% glycerol at -80^0 C for further use.

Table 2.3.3: PDEST15 Gαi1W258A and DeltaN31 Gαi1 purification buffers

Buffers	Ingredients and Methods
Lysis/Wash	50 mM Tris, pH = 8.0 with HCL, 250 mM NaCl, 2 mM DTT, 2 mM PMSF, 50 µM GDP
QA buffer	50 mM Tris, pH = 8.0 with HCL, 2 mM DTT, 10 µM GDP
QB buffer	50 mM Tris, pH = 8.0 with HCL, 500 mM NaCl, 2 mM DTT, 10 µM GDP
Size-Exclusion	50 mM Hepes pH =8.0 with NaOH, 150 mM NaCl, 1 mM TCEP, 10 µM GDP

2.3.4: Purification of myristoylated Gαi1

Plasmids harboring N-methyltransferase (pBB131) and Giα1 (PQE60) were simultaneously transformed into JM109 competent cells. The cells were plated onto LB plates containing Amp at 50 µg/mL and Kan at 50 µg/mL overnight in an incubator at 37^0C. Single or multiple colonies were inoculated into LB media containing Amp (50 µg/mL) and Kan (50 µg/mL) and grown overnight in a incubator shaking at 200 rpm. Cells were harvested by centrifugation at 8,000 rpm at 4^0C. The cells were resuspended in TB media containing Amp (50 µg/mL) and Kan (50 µg/mL) for inoculation into 2.79L flasks containing TB media at the same antibiotic composition. The cells were then grown in a incubator at 37^0C shaking at 200 rpm until an OD of 0.4 was reached. At this point, the temperature was reduced to 30^0C and the cells were induced with 30 µM IPTG overnight. Cells were harvested by centrifugation at 8,000 rpm at 4^0C. The pelleted cells were stored at -80^0C for further use.

Pelleted cells were thawed and resuspended in 300 mL of TBP. Resuspended cells were lysed using a cell disruptor and the soluble fraction was collected by centrifugation at 18,000 rpm at 4^0C. The soluble fraction was applied onto 5 mL of packed Ni-NTA beads and was allowed to mix gently overnight at 4^0 C. The beads were then washed with Wash buffer until a bradford assay indicated that no more unbound protein was being eluted off. Myristoylated Gαi1 (mGαi1) was eluted with Elution buffer and was dialyzed in buffer C. Dialyzed mGαi1 was applied to a UNO-Q6 column for anion exchange was eluted with a gradient of 0 mM to 500 mM NaCl with Buffer C and D. Fractions containing mGαi1 were pooled and collected for size-exclusion chromatography to remove aggregates. Pure protein was stored at -80^0 C for further use.

Table 2.3.4: mGαi1 purification buffers

Buffers	Ingredients and methods
TBP Buffer	50 mM Tris, pH = 8.0 with HCL, 100 mM NaCl, 5 mM BME, 1XPTT, 50 µM GDP
Wash Buffer	50 mM Tris, pH = 8.0 with HCL, 400 mM NaCl, 5 mM BME, 1XPTT, 50 µM GDP, 10 mM Imidazole pH=8.0, 10% glycerol
Elution Buffer	50 mM Tris, pH = 8.0 with HCL, 5 mM BME, 1XPTT, 50 µM GDP, 150 mM Imidazole pH=8.0
Buffer C	50 mM Tris, pH = 8.0 with HCL, 2 mM DTT, 10 µM GDP

Buffer D	50 mM Tris, pH = 8.0 with HCL, 2 mM DTT, 10 µM GDP, 500 mM NaCl
Size-exclusion buffer	50 mM Hepes pH =8.0 with NaOH, 150 mM NaCl, 1 mM TCEP, 10 µM GDP

2.3.5: Nanobody purification

Plasmids harboring nanobody were transformed into WK6 competent cells and plated onto LB plates containing 100 µg/mL of Amp. The cells were left to grow overnight in a incubator at 37^0C. Single or multiple colonies were inoculated into LB media containing 2% glucose, 1 mM $MgCl_2$ and 100 µg/mL Amp. The cells were grown overnight in a incubator at 37^0C shaking at 200 rpm. Cells were harvested by centrifugation at 8,000 rpm at 4^0C. Pelleted cells were resuspended with TB media containing 1% glucose, 1 mM $MgCl_2$, and 100 µg/mL Amp. The suspended cells were inoculated into 2.79 L shaker flasks containing 1.0 L of TB media, 1 mM $MgCl_2$, 1% glucose, and 100 µg/mL Amp. The cells were grown in an incubator at 37^0C until an OD of 0.7-1.0 was reached at which point the temperature was reduced to 28^0C and the cells were induced with 300 µM IPTG. The cells were grown overnight and harvested by centrifugation at 8,000 rpm at 4^0C. Pelleted cells were stored at -80^0C for further use.

Cells were thawed and resuspended with ice cold TES buffer at 100 mL per liter of cell growth. The cells were allowed to mix with a stir bar for an hour at 4^0C. The solution containing resuspending cells was slowly dripped into TES buffer diluted 1 to 4 to lyse and was allowed to stir 4^0C. The soluble fraction was isolated by centrifugation at 8,000 rpm for 30 minutes at 4^0 C and was applied to 5 mL per liter of packed Ni-NTA beads per liter of cells grown. The soluble fraction was mixed gently overnight with the beads to enhance binding at 4^0C. The column was then washed with 5 column volumes of wash buffer I, 20 column volumes of wash buffer II, 10 column volumes of wash buffer III and finally, eluted with 3 column volumes of elution buffer. The nanobodies eluted were dialyzed against dialysis buffer and polished with size-exclusion buffer. Pure protein was stored at -80^0C for further use.

Table 2.3.5: Nanobody purification buffers

Buffers	Ingredients and methods
TES	50 mM Tris, pH = 8.0 with HCL, 0.5 mM EDTA pH=8.0, 0.5M Sucrose
Wash Buffer I	50 mM Tris, pH = 8.0 with HCL, 1M NaCl
Wash Buffer II	50 mM MES, pH = 6.5 with HCL, 1M NaCl
Wash Buffer III	50 mM Tris, pH = 8.0 with HCL, 500 mM NaCl
Elution Buffer	50 mM Tris, pH = 8.0 with HCL, 200 mM NaCl, 500 mM Imidazole pH =8.0
Dialysis Buffer	50 mM Tris, pH = 8.0 with HCL, 200 mM NaCl
Size-exclusion buffer	50 mM Hepes, pH = 8.0 with NaOH, 150 mM NaCl, 1 mM TCEP

Table 2.3.6: Nanobodies purified for this study

Nanobodies	Binding specificity
NB 8431	Complex binder only, at interface between Ric-8A and Gα.
NB 9156	Complex binder and Gα binder. Binds to the helical domain of Gα.
NB 8117	Complex binder and Ric-8A binder. Binds to the N-terminus of Ric-8A.
NB 8109	Complex binder and Ric-8A binder. Binds to the C-terminus of Ric-8A
NB 8119	Complex binder and Ric-8A binder. Binds to the C-terminus of Ric-8A.

2.4.1: Ric-8A phosphorylation by casein kinase 2

Before CK2 treatment, Ric-8A was purified further by anion exchange chromatography using a salt gradient of 100 mM NaCl to 1M NaCl. Ric-8A-491 typically eluted at 16 mS/cm, while Ric-8A- 530 eluted at a salt concentration of 25 mS/cm. After anion exchange chromatography, Ric-8A was purified using size-exclusion chromatography (HiLoad 16/600 Superdex, GE healthcare life sciences) to

separate aggregates and lower molecular weight bands. Ric-8A was then diluted in 1 X CK2 buffer at a concentration of 3.5-12 mg/mL. CK2 (New england biolabs) was added as described by the manufacturer. The mixture containing Ric-8A and CK2 was incubated overnight at room temperature. Phosphorylated Ric-8A was purified using a salt concentration of 100 mM NaCl to 1M NaCl. Typically, phosphorylated Ric-8A-491 eluted at 18 mS/cm while phosphorylated Ric-8A-530 eluted at 30 mS/cm.

Table 2.4: Buffers for Phosphorylating Ric-8A by CK2

Buffers	Ingredients and Methods
QA buffer	50 mM Hepes, pH = 8.0 with NaOH, 100 mM NaCl, 1 mM DTT, 1 mM EGTA pH = 8.0
QB buffer	50 mM Hepes, pH = 8.0 with NaOH, 1M NaCl, 1 mM DTT, 1 mM EGTA pH = 8.0
CK2 Buffer	50 mM Hepes, pH = 8.0 with NaOH, 20 mM MgCl2, 100 mM NaCl, 1 mM DTT, 2 mM EGTA pH = 8.0, 3-5 mM ATP, 1X PTT/LL
Size-Exclusion buffer	50 mM Hepes, pH = 8.0 with NaOH, 150 mM NaCl,1 mM TCEP

2.4.2: Purification of Ric-8A:Gα:nb complexes

Purification of Ric-8A:Gα:nb was proceeded with the following protocol. All proteins were stored at -80^{0}C up to the following point. Each individual component was again further purified using size-exclusion chromatography before mixing for complex formation. Purified Ric-8A was mixed with Gα and nb at a molar ratio of 1:2:3. The components were allowed to incubate from 1 hour to overnight, where no significant difference between complex formation was noticed from these time differences. The solution composed of these mixtures was then further purified with size-exclusion buffer (buffer comprised of Hepes pH=8.0, 150 mM NaCl, 1 mM TCEP) to separate Ric-8A:Gα:nb complex from excess free components of Gα and nanobody. Components comprised of Ric-8A:Gα:nb complex were pooled and collected for structural studies

2.5: SDS-PAGE

Sodium dedocyl sulfate polyacrylamide gel electrophoresis (SDS-PAGE) was used to determine the purity of the protein by fractionating protein molecules according to their mass. All gels used for this study were commercially purchased (Biorad, Mini-Protean Precast Gels) and were not made in the laboratory. To run SDS-PAGE for protein purity analysis, the gel was secured in a Biorad gel box with 1 X SDS Running buffer filled in the cathode chamber and the anode chamber. Before loading protein samples into the gel, protein samples were mixed with 1 X SDS sample buffer and denatured with a heat block at 95^0 C for 5 minutes. The electrophoresis was performed at 200 V for 30 minutes. Gels were stained using coomassie brilliant blue to visualize protein bands.

Table 2.5.1: SDS-PAGE Running Buffer Recipe/Gel staining and destaining recipe

Solution	Ingredients and Methods
1.5 M Tris-HCL (pH = 8.8)	181.7 g Tris base dissolved in 500 mL of dH2O, HCL was added to adjust pH to 8.8. Autoclaved and stored at RT.
1 M Tris-HCL (pH = 6.8)	25 g SDS powder was dissolved in 250 mL of dH2O. Stored at room temperature
10% (w/v) SDS	121.1 g Tris base was dissolved in 500 mL of dH2O, HCL was added to adjust to pH= 8.8. Autoclaved and stored at RT.
10 x SDS running buffer	10 g SDS (1% w/v), 30.3 g Tris base (250 mM) and 144.1 g glycine (2 M) were dissolved in 1 L of dH2O. Stored at RT
1 x SDS running buffer	100 mL of 10 X SDS running buffer plus 900 mL of dH2O. Stored at RT.
1 x SDS sample buffer	2% (w/v) SDS, 80 mM Tris-HCl (pH 6.8), 10% (v/v) glycerol, 1.5% (w/v) dithiothreitol (DTT), 0.1 mg/ml bromophenol blue. Stored at 4°C.
Coomassie brillant blue stain	Methanol (50 % v/v), 1 gram of coomassie brillant blue stain (BioRad), Glacial acetic acid (10 % v/v), H2O (40 % v/v). Stored at RT.

Destaining solution	Methanol (66 % v/v), Glacial acetic acid (7.5 % v/v), H2O (26.5 % v/v). Stored at RT

2.6: Vitrification of Ric-8A:Gα:nb complexes

To maintain the native form of proteins for high resolution reconstructions, hydrated protein samples were vitrified in a thin layer of ice by plunge freezing in liquid ethane cooled to liquid nitrogen temperatures. Protein vitrification was achieved using a FEI vitrobot. Copper meshed grids coated with carbon from Quantifoil (R2/1 μm hole, 200 mesh Cu) holey grids were negatively glow discharged at 15 mA for 40 seconds and then placed on a pair of tweezers. The chamber temperature of the vitrobot was set to 4^0 C with 100 % humidity to avoid sample evaporation before blotting. 3 μL of 0.1-3 mg/mL of protein was loaded onto the grid for for 6 seconds to allow the protein to settle on the carbon grid. The grid was automatically blotted blotted using a time range of 3-6 seconds on the vitrobot to remove excess liquid and was plunge frozen into liquid ethane pre-cooled with liquid nitrogen. Frozen grids were stored in liquid nitrogen until further use.

2.7: Operation of Talos Arctica and Titan Krios microscopes

Protocol courtesy of Megan Mayer

Grids containing the sample of interest were inserted into Talos microscopes for screening and into Titan Krios microscopes for high-resolution data collection. Data collection on the microscopes was performed using FEI EPU software. The following protocol was utilized for microscope operation.

Load grid cassette, perform inventory, insert a grid sample.

○ After docking a cassette, In TemUI's "Autoloader" Box, inventory your grids. Autoloader may have to be Initialized in the flapout if the cassette slots are not visible.

○ Double click on a grid to load it to the stage.

Launch EPU.

○ If EPU will not open: Must be in EFTEM mode in TEM-UI; Remote Gatan computer communication must be initiated (icon in bottom right hand of TEM-UI screen).

In EPU, check all magnification Preset parameters

○ In EPU 'preparation' tab, go through each preset in the dropdown menu.

■ Atlas Preset: ~135x, EF-CCD, binning 2, Readout Fill, Exp TIme 1s, Mode Linear, Nanoprobe, Spot Size ~6, no Slit.

■ Gridsquare Preset: ~580x-1000x, ~135x, ~-30-50 um defocus, EF-CCD, binning 2, Readout Full, Exp Time 1s, Mode Counting, Nanoprobe, Spot Size ~6, no Slit.

■ Eucentric Height Preset: ~1700x, K2 Dose over an empty hole should be ~10-15 e/pixel/second on a K2 camera. EF-CCD, binning 1, Readout Full, Exp TIme 1s, Mode Counted, Nanoprobe, Spot Size ~6, 20 nm slit.

■ Data Acquisition Preset: >100x. K2 Dose over an empty hole should be ~7-10 e/pixel/second on a K2 camera. EF-CCD, binning 1, Readout Full, Exp Time Xs (decide later), Mode Counted, Nanoprobe, Spot Size ~6, 20 nm slit.

■ Autofocus preset: Same as Data Acquisition Preset, except: bin 2, exposure 1s.

■ Drift Preset: Same as Data Acquisition Preset, except: bin 2, exposure 1s.

■ Zero Loss: Same as Data Acquisition Preset, except: bin 2, exposure 1s.

■ **These parameters are all estimations. Adjust each preset in DM so that the dose rate at the K2 is reasonable at the specific mode

In EPU, collect Atlas.

○ In EPU “Atlas” tab:

■ Create new session in ‘Session Setup’. MRC. Save to X drive, not C drive.

■ In ‘Atlas Acquisition’, press Start. Make sure column valve is open and the beam is centered before walking away.

Align the beam over carbon in EPU’s “Data Acquisition” mag preset. These alignments are done in TEM-UI, over the flu-screen.

○ If beam on flu screen is not round, Adjust condenser astigmatism.

■ In TEM-UI stigmators box, click condenser. Adjust with mf-x and mf-y to make sure that the beam is round on the Flu-screen.

○ Find eucentric height,

■ Can be done either in EPU “AutoFunction” tab → Eucentric by beam tilt, or manually in TEM-UI “Stage” box using alpha wobbler in flapout.

○ Normalize defocus by pressing eucentric focus on hand panel.

○ In TEM-UI direct alignments:

■ Beam Shift: Use mf-x and mf-y to shift beam and center to either K2 (small green circle) or ceta (large red circle).

■ Center C2 aperture in direct alignments. The intensity will be wobbled on Titan, it will not wobble on Talos. Make sure the beam is centered on itself when intensity is increased/decreased. If manually

centering, check free-control and turn off C3 condenser. On talos, center beam using beam shift, increase intensity, and center beam using C2-aperture adjustments.

■ NP Pivot Points Beam tilt, both x and y, in direct alignment. Make intensity/ illum. area as small a point as possible before crossover, with mf-x adjust until the two points merge. Only use mf-x for main adjustment of both, and mf-y for minor perpendicular adjustment.

■ Rotation center adjust until the image no longer moves, while the beam may still rotate/spiral around the image.

■ Coma Free Pivot Points Beam tilt, both x and y, in direct alignment. . Make intensity/ illum. area as small a point as possible before crossover, with mf-x adjust until the two points merge. Only use mf-x for main adjustment of both, and mf-y for minor perpendicular adjustment.

○ Use Auto CTF for Automated objective astigmatism and auto coma correction.

■ Measure at ~3 sec exposure, 2 binning, electron counting, -1 um defocus. Measure repeatedly until it passes.

■ Auto stigmate. Using these parameters.

■ Auto coma. Using these parameters.

○ Move beam to over a hole and measure dose at the K2 camera.

■ In DM, click View with data acquisition parameter beam. Dose will be a read out in X e-/pix/sec. Adjust the beam until the illumination area is ~1-1.3 um and the dose is ~7-10 e-/pix/sec on the K2.

○ Save these beam settings in EPU “preparation” tab: click “GET” under “data acquisition” magnification pre-set. This will save your beam at this state and illumination area. Adjust your data acquisition exposure time so that the total electron dose is ~50 e-. Adjust your “Fractions” to be ~30-50. “Fractions” refers to # frames in your exposure time. (EPU’s terminology is a bit confusing here).

Tune Energy Filter in Digital Micrograph at Data Acquisition parameters

○ Move beam over an empty hole on grid. Increase spot size to ~ 2 (beam should

be reading in counting mode)

○ Make sure you are in power user mode. Help → user mode → power user

○ Perform “Full tune” This also centers the ZLP.

Prepare Gain reference in Digital Micrograph at Data Acquisition Parameters

○ This should be done over empty hole. Remaining at this higher spot size (about 2), go to Camera tab → Prepare gain reference defualts usually good. The first gain reference is for linear mode want counts to be about 2000. Follow prompts (adust beam intensity), always adust beam over screen. Can adjust the beam dropping spot size and adjusting intensity knob. Reduce to lower spot size for counting reference (easiest way is to say “Set” in data acquisition parameter in EPU).

Once the beam is aligned, align all the different magnification presets in EPU.

○ First begin by finding a piece of dirt on your grid that you can see at data acquisition preset, and are still able to locate at lower mags.

○ Make sure you are at eucentric height and ~-2 um defocus at your data acqusition mag preset.

○ In preparation tab, on the left hand panel, go to “calibrate image shifts”.

○ Click Start. This will take an image of the item at the highest preset magnification, Data Acquisition. Make sure the item is identifiable in the first image.

○ Click proceed. This will take an image at the next step lower magnification preset called “eucentric height”. If this image is not centered properly, click on the item and “Re-Acquire” the image. Once the item is centered, click proceed.

○ Repeat until all mags have been calibrated.

○ Atlas may have to be re-acquired at this step, should only take ~5 mins on latest version of EPU.

In EPU, go to EPU tab and create a new session for setting up the automated data collection.

○ Under Tasks, everything is in order.

■ New Session SetUp:

● Session Name: Sample_Date

● Type: Manual

● Acquisition Mode: Accurate Hole Centering (Updated EPU only)

● MRC

● Unnormalized Packed w/ Gain Ref files

● Save to X:\DoseFractions (on DM)

● Apply

■ Square Selection:

● Choose a square, right click, Add, move stage to square

■ Hole Selection:

● AutoEucentric finds the eucentric height in the Eucentric height mag preset. After eccentricity is found, acquire an image. This saves the height.

● Measure hole size: yellow rings should be slightly larger than hole

○ Note: you only need to measure hole size once, all

preceding square hole templates will be based off this measurement.

● Find holes: patterns all holes based on measurement

● Remove holes close to grid bar

● Selection brush: remove any empty/trash

■ Template Definition

● Acquire

● Add Acquisition Area, add defocus range -1.5 to -3.0 um

● Add Autofocus Area, every 10 um, use objective lense, measure astigmatism

● Add drift measurement, once per grid square

● 5, 0.5, 0.5

■ Automated Acquisition: Press start. Make sure everything is running. Press start on your sample in eLogbook, with the updated parameters, to launch motion correction.

PHASE PLATE SETUP. Check to see which phase plate was last used and choose a new one.

○ TEM 1,2,4: Go to phase plate tab and hit active. Check MF-Y to find focal plane.

■ If image becomes streaky, un-check MF-Y. Adjust stigmator of condenser. When streaks are removed, Click done on condenser adjustment, and return to MF-Y.

■ Iterate between MF-Y of phase plate and condenser stigmator until you find the “Fish eye” view of the focal place and streaks are removed.

■ Go to direct alignments → phase plate alignments. Follow steps to align.

○ TEM 3: MUST BE IN PARALLEL BEAM CONDITION. Use intensity in FINE to find back focal plane.

■ If image becomes streaky, Adjust stigmator of condenser. When streaks are removed, CLick done on condenser adjustment, and return to adjusting intensity.

■ Iterate between changing intensity on back focal phase plate and condenser stigmator until you find the “Fish eye” view of the focal place and streaks are removed. Make note of the C2 % and values for condenser stigmation, as they will need to be kept consistent throughout data collection.

○ Use auto-CTF to measure optimal activation time under your beam conditions, with a target phase shift of ~0.5. May need to activate with a larger aperture immediately before data collection, and use the same position for entire data collections.

2.8: Data processing

The data was primarily processed using the Relion-3.1.0 software. In some cases, cryosparc was used for homogeneous refinement or heterogeneous refinement to achieve higher resolution. Furthermore, the software Topaz was used for particle picking to start with a initial cleaner particle set for processing, in cases where low resolution was observed.

2.8.1: CTF Correction

CTF correction for all data set was performed using the CTFFIND4.1 program. Typically, this was performed using mostly default values given from the program. The parameters were the following, FFT box size 512, minimum resolution 30 angstroms, maximum resolution 7.1 minimum defocus value 5000 angstroms, maximum defocus value 500000 angstroms, and phase shifts were not estimated as no phase plates were used. After CTF correction, micrographs containing high astigmatism and low CTF resolution was removed before processing.

2.8.2: Particle picking

Particle picking for the data sets was performed using the template picking function in Cryosparc or the Topaz particle picking software located in Cryosparc. Template picking begins by either manually selecting particles by hand, or by automatically selected particles using a Gaussian based function with user inputs for particle diameter that is expected and the threshold of the relative pixel contrast to the background of the micrograph. The manually or automatically selected particles are then subjected to reference free 2D class averaging and the best 2D class averages are then selected by the user. The good 2D class averages are then used as templates to pick good particles from the micrographs typically with a low-pass filter of 20Å to prevent “Einstein from noise” artifacts. Furthermore, these particles can be used as training for the Topaz neural network training network to select for good particles for further processing.

2.8.3: 2D class Averaging

2D class averaging was performed in the Relion 3.1.0 software or with the Cryosparc software. A box size of 200 was used and a set mask diameter of 160 angstroms (set in Relion 3.1.0) was used to remove solvent noise surrounding the particles. Typically, the number of classes was set from 100-200 and multiple rounds of 2D classifications were performed to remove poor 2D class averages. Most

settings for this parameter were performed under recommendations by the developer, or by using the default settings of the program.

2.8.4: Generating Initial models

To generate reliable and accurate initial models, the best 2D class averages (showing protein secondary structure) were selected. Typically, 3-12 models were generated initially to separate heterogeneity or poor particles from affecting the integrity of the maps. C1 symmetry was applied as the protein complex exhibits no symmetry.

2.8.5: 3D classification and map refinement

The best initial model generated in the previous step was Gaussian low pass filtered at 20 angstroms and used for 3D classification in Relion 3.1.0 or by the heterogeneous refinement program in Cryosparc. Multiple rounds of 3D classification or heterogeneous refinement were used to separate differing conformations and poor maps from the dataset. The best 3D classification map obtained was used for non-uniform refinement in Cryosparc. After refinement, local CTF refinement was performed for maps that were higher than 5 Å resolution, to better model the CTF. Furthermore, this was followed by another round of non-uniform refinement in Cryosparc to measure an FSC at higher resolution. For very noisy datasets, 3D refinement was not performed as it did not yield improvements in the map.

Chapter 3. Optimization of Ric-8A:Gα Complexes for Cryo-EM

3.1: Chapter Introduction

To investigate the structure of the Ric-8A:Gα complex, by single-particle cryo-EM analysis, various combinations of nanobodies were used to stabilize the complex during vitrification. In addition, detergents were added, in some cases, before freezing to prevent complex dissociation and to reduce its interaction with the air-water interface. This chapter will discuss the purification of various Ric-8A:Gα complexes, and the results obtained from these complexes from single-particle cryo-EM analysis. Purification of the individual components used to make the complexes will not be discussed and rather the optimization of the complexes for single-particle cryo-EM will be discussed in detail.

3.2: Purification of Ric-8A:Gαi1:nb complexes for cryo-EM analysis

Individual protein components were purified from *e.coli* to high purity and homogeneity using affinity chromatography, ion exchange chromatography, and size-exclusion chromatography. To make phosphorylated Ric-8A for structural studies, purified Ric-8A was treated with CK2 overnight at room temperature. Separation of phosphorylated Ric-8A from unphosphorylated Ric-8A was achieved using anion exchange chromatography, where phosphorylated Ric-8A elutes at a higher salt concentration. Purified proteins were then mixed, and incubated on ice for at least one hour to overnight, before further purification on a size-exclusion chromatography to separate excess Gα and nanobody from the complex. Confirmation of protein purity and complex formation was confirmed from SDS-PAGE analysis. Representative chromatograms of anion exchange and size-exclusion are shown in Figure 3.1 along with an SDS-PAGE showing complex purity.

3.3: Cryo-EM analysis of Phosphorylated Full-Length Ric-8A bound to mGαi1 and Nb 9156

3.3.1: Micrograph inspection

Initial analysis of the Ric-8A:Gαi1 complex was performed using full-length phosphorylated Ric-8A bound to mGαi1 and nb 9156. Nb 9156 binds to the helical domain of Gαi1 and could potentially reduce the inherent flexibility of the domain facilitating structural determination. Myristoylated Gαi1 was chosen to mimic physiological conditions and to investigate the effects that the lipid modification may induce the interaction between Gαi1 and Ric-8A. To obtain preliminary data, purified complex was vitrified and a data collection was performed with a total dose of 56.25 e/A^2. Approximately 1,000 micrographs were collected for cryo-EM processing using the software packages Relion and Cryosparc. The micrographs were very heterogeneous, with the presence of proteins that were smaller

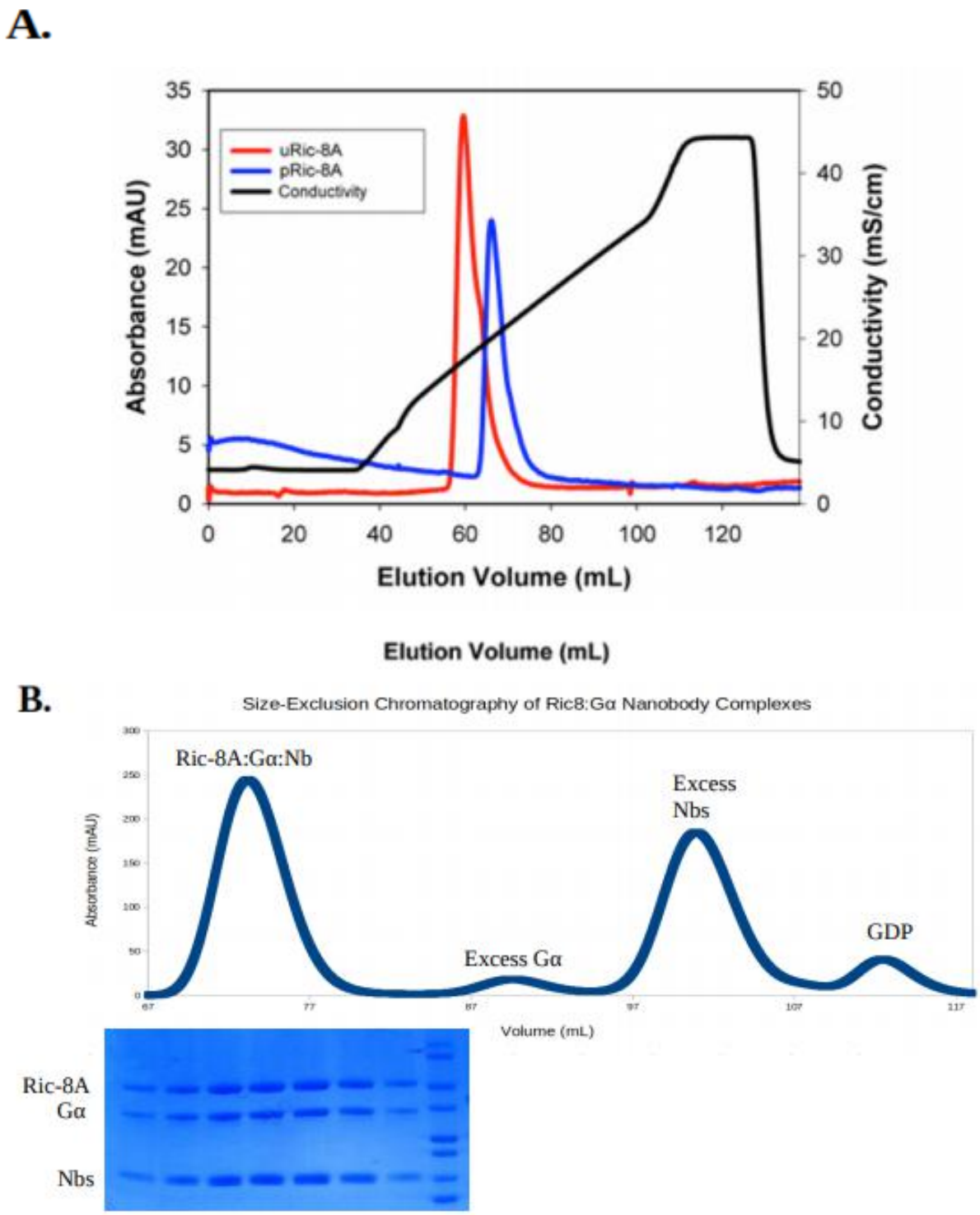

Figure 3.1: Displays the typical purification method used to obtained pure and homogenous Ric-8A complexes for cryo-EM analysis. A) Anion exchange chromatogram displaying the shift of phosphorylated Ric-8A-491 (blue line) relative to unphosphorylated Ric-8A-491 (red line). B) A typical size-exclusion chromatogram for Ric-8A complexes. The SDS-PAGE shows the purity of the first complex peak comprised of all the individual components at an approximate 1:1 ratio to each other. Figure 3.1A was obtained from reference (168).

A.

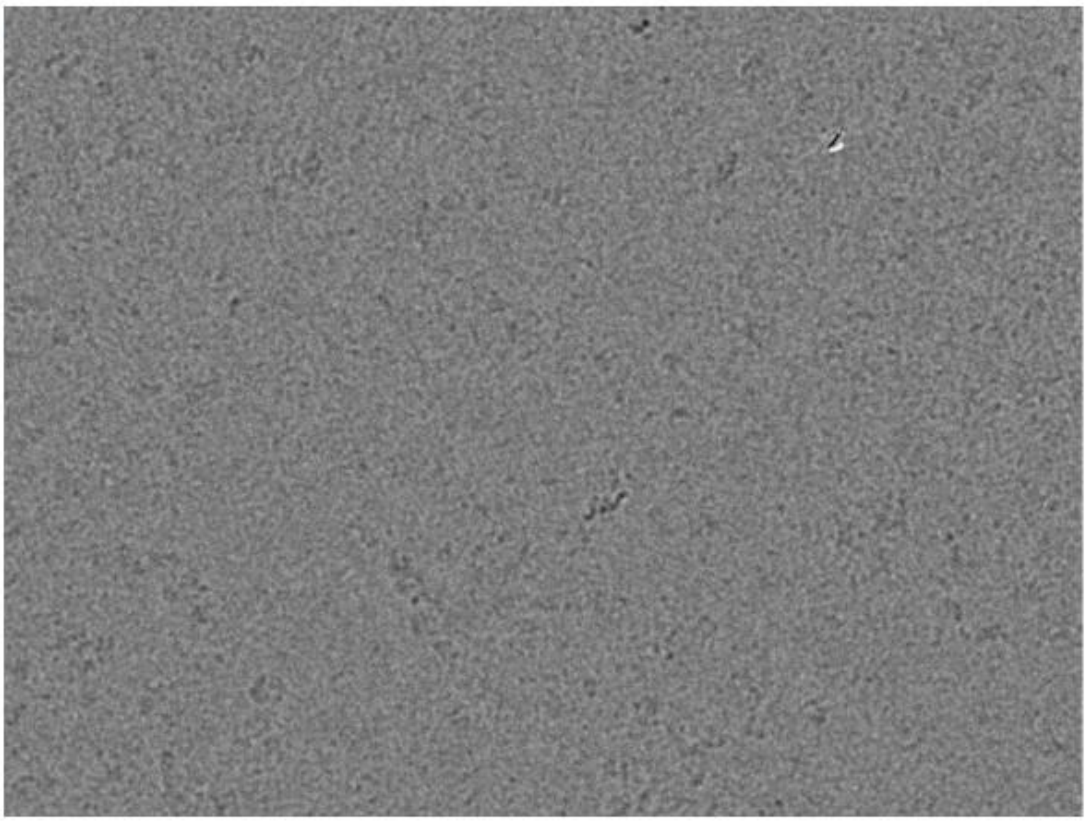

B.

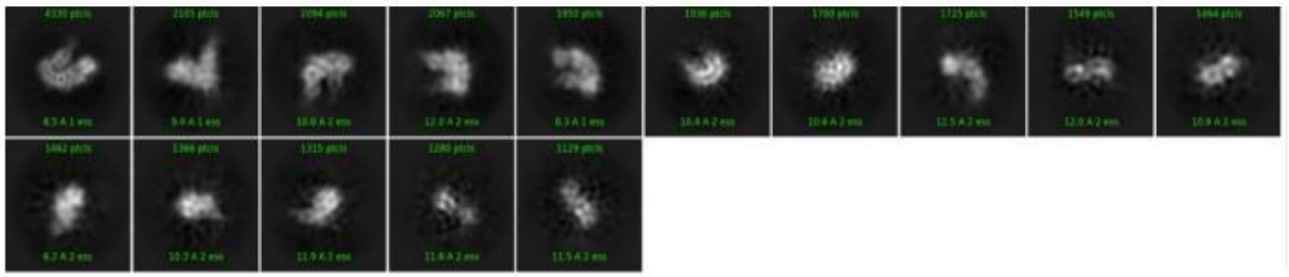

Figure 3.2.1: A) A representative micrograph of the data collected of the complex of full-length Ric-8A with mGαi1 and nb 9156. There is a high background present due to complex dissociation. B) 2D class averages generated from the data set in cryosparc. Most of the 2D class averages are very poor. Only the first class exhibits high resolution features.

then the expected size of 100 kilodaltons for Ric-8A:mGαi1:9156 complex. The proteins contributing to the background of the micrographs were unbound Ric-8A and mGαi1 that dissociated from exposure to the air-water interface during vitrification. A micrograph for the data collected is shown in Figure 3.2.1 A.

3.3.2: Particle picking, reference free 2D classification, and 3D classification

Particle picking was performed using the laplacian of guassian function with a diameter of 80-110 on all micrographs and multiple rounds of 2D classification was performed to remove junk particles. Good 2D classes were then used for template picking to select for more good particles. 2D classification and 3D classification was done using either Relion or Cryosparc software packages. Both Relion processing and Cryosparc processing produced the same results, in this case, for 2D classifications and 3D classifications. The resulting reference free 2D classes were very noisy in the data set, with only the one class average exhibiting secondary features (Figure 3.2.1). For this data set, only 3D classifications were performed, instead of 3D refinements, as 3D refinements only resulted in noisier maps. The 3D model obtained exhibited features that corresponded to Ric-8A and mGαi1. The nanobody and the helical domain of this map could not be found, and the observed density for mGαi1 most likely corresponded to the Ras domain. The 3D model generated from the data set is shown in Figure 3.2.2. It was clear from the data that sample and vitrification optimization would be required to achieve a high-resolution map of the complex.

3.4: Cryo-EM analysis of pRic-8A-491:DeltaN31Gαi1:8117:8109 Complex

3.4.1: Micrograph Analysis

To increase the resolution of the maps obtained, truncated forms of Ric-8A (forty residues at the C-terminus removed) and Gαi1 (31 residues at the N-terminus removed) were used to reduce the flexibility of the complex. Furthermore, two nanobodies (8117, 8109) were added to the complex to reduce the inherit flexibilty of the Ric-8A protein, where 8117 binds toward the N-terminus of Ric-8A and NB 8109 binds toward the C-terminus of Ric-8A. The nanobodies in this experiment would also act to facilitate image alignment during 2D classification and 3D classification. In addition to using nanobodies for complex stability, either 0.01% NP-40 or 0.01% OG detergents were added to the complex just prior to vitrification.

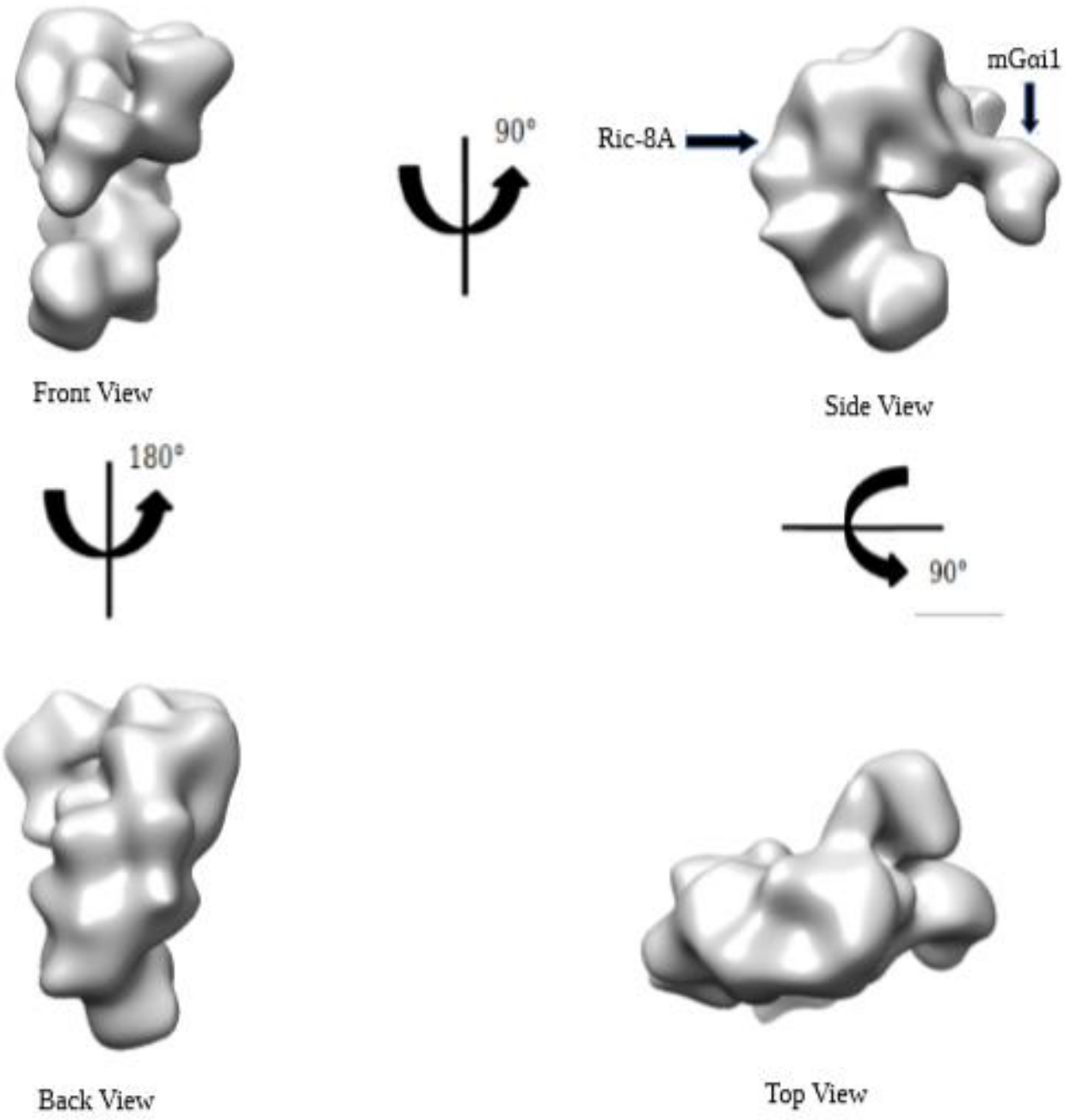

Figure 3.2.2) Preliminary 3D map generated from Full-length Ric-8A bound to mGαi1 and Nb 9156 at 15 angstrom resolution. Ric-8A density and mGαi1 density is labeled in the figure with differing views of the map.

The detergents in this experiment would act to reduce complex dissociation during vitrification, ideally leaving more intact good particles to achieve higher resolution.

The complex containing NP-40 was screened briefly on the Talos Arctica and approximately 1500 micrographs were collected at a total dose of 52 e/A^2. The addition of NP-40 greatly reduced the amount of background observed in the micrographs, indicating that complex dissociation was reduced, though the detergent did induce some protein aggregation. The complex containing OG was screened on the Talos Arctica and approximately 1300 micrographs were collected at a total dose of 50.4 e/A^2. The sample was imaged and collected with a phase plate to enhance the contrast of the particles for better visualization. The addition of OG appeared to have also reduced the amount of background present, with clear intact particles. It was concluded that the addition of detergents to the sample before vitrification was indeed, reducing complex dissociation at the air-water interface. The micrographs are shown in Figure 3.3.1.

3.4.2: Reference Free 2D classification and 3D classification

Both datasets collected for the pRic-8A-491:DeltaN31Gαi1:8117:8109 complexes were processed using the Cryosparc software package. For the data set containing NP-40, 2.6 million particles were picked and extracted using the template picking function. Multiple rounds of 2D classification were performed to remove poor particles and approximately 26,865 particles were left ab-initio reconstruction and 3D classification. For the data set containing OG, 355,6882 particles were picked and extracted for multiple rounds of 2D classification until 90,685 particles were left for 3D classifications. Interestingly, 3D classification and refinement of the data set containing NP-40 only resulted in very low-resolution maps (15 angstroms), despite the appearance of better particles in the micrographs. The final 2D classes did not exhibit any high resolution features, even after filtering out most of the junk particles in the data set. The low resolution observed in the 2D classifications of the data set was most likely due to the lack of non-aggregated protein particles, and thus, not enough particles were present to achieve high-resolution. The final 3D map did have low resolution features that corresponded to Ric-8A, Gαi1, Nb 8117, and NB 8109. For the data set containing OG, the 2D classifications were even more featureless then the NP-40 data set, despite having much less aggregation and the presence of many individual particles. This was most likely caused by the phase plate used to enhance the of the particles, where there was a loss of high frequency information.

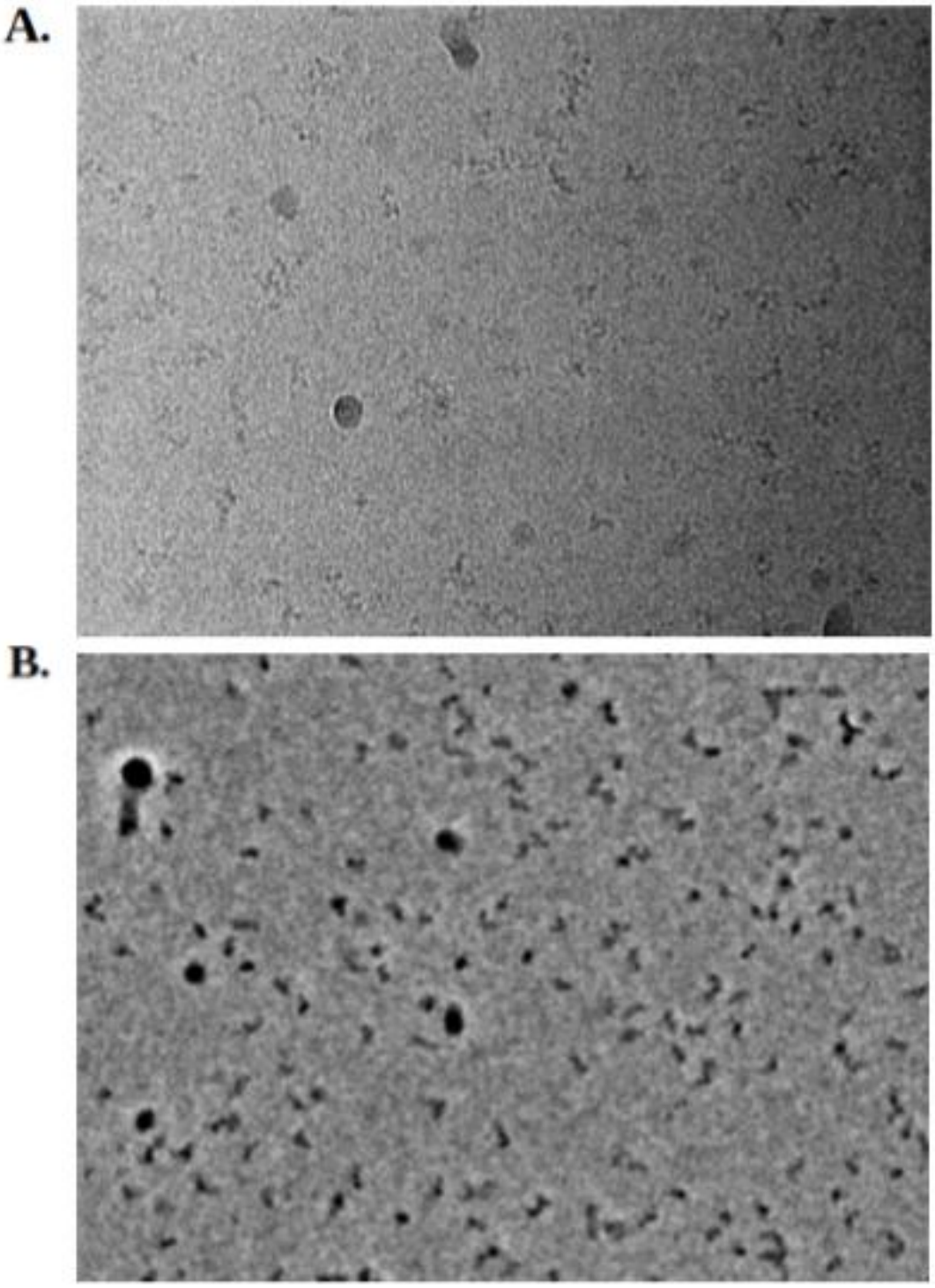

Figure 3.3.1) Micrographs of the phosphorylated Ric-8A-491:DeltaN31Gαi1:8117:8109 complex. A) The complex vitrified containing 0.01% NP-40. B) The complex vitrified containing 0.01% OG with a phase plate used to enhance the contrast of the particles.

A.

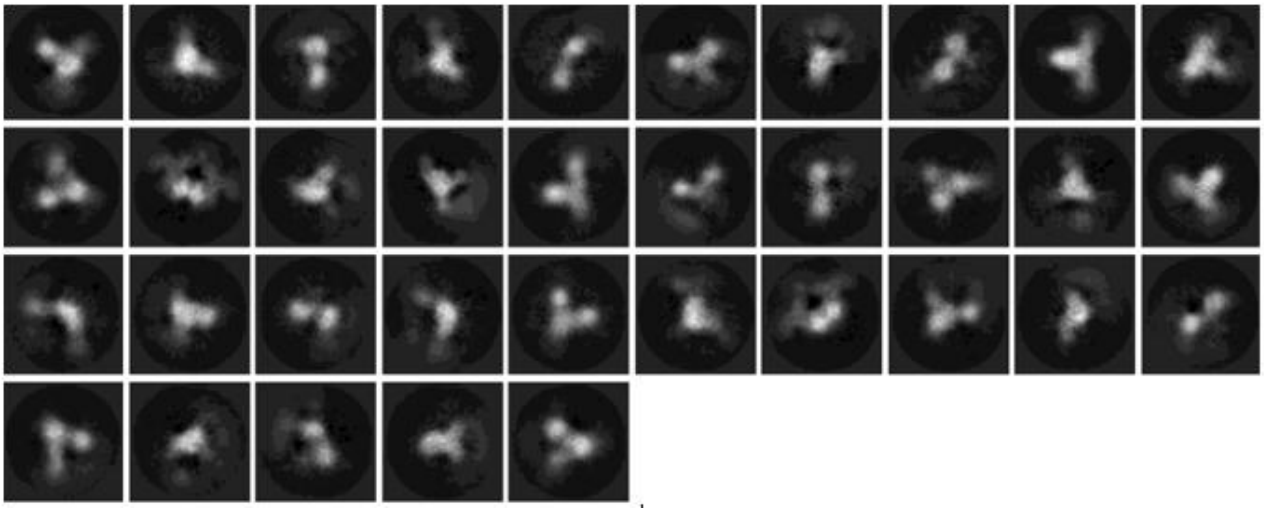

B.

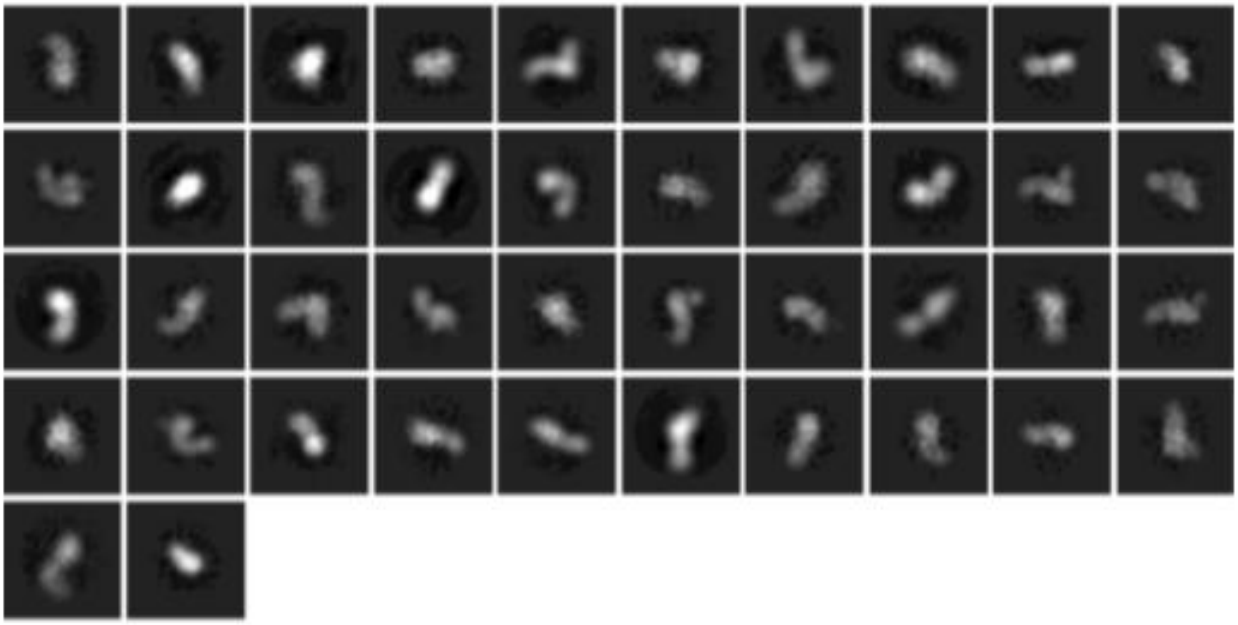

Figure 3.3.2) 2D class averages generated for PRic-8A-491:DeltaN31Gαi1:8117:8109 complex. A) 2D class averages of the complex vitrified containing 0.01% NP-40. B) 2D class averages of the complex vitrified containing 0.01% OG with a phase plate used to enhance the contrast of the particles.

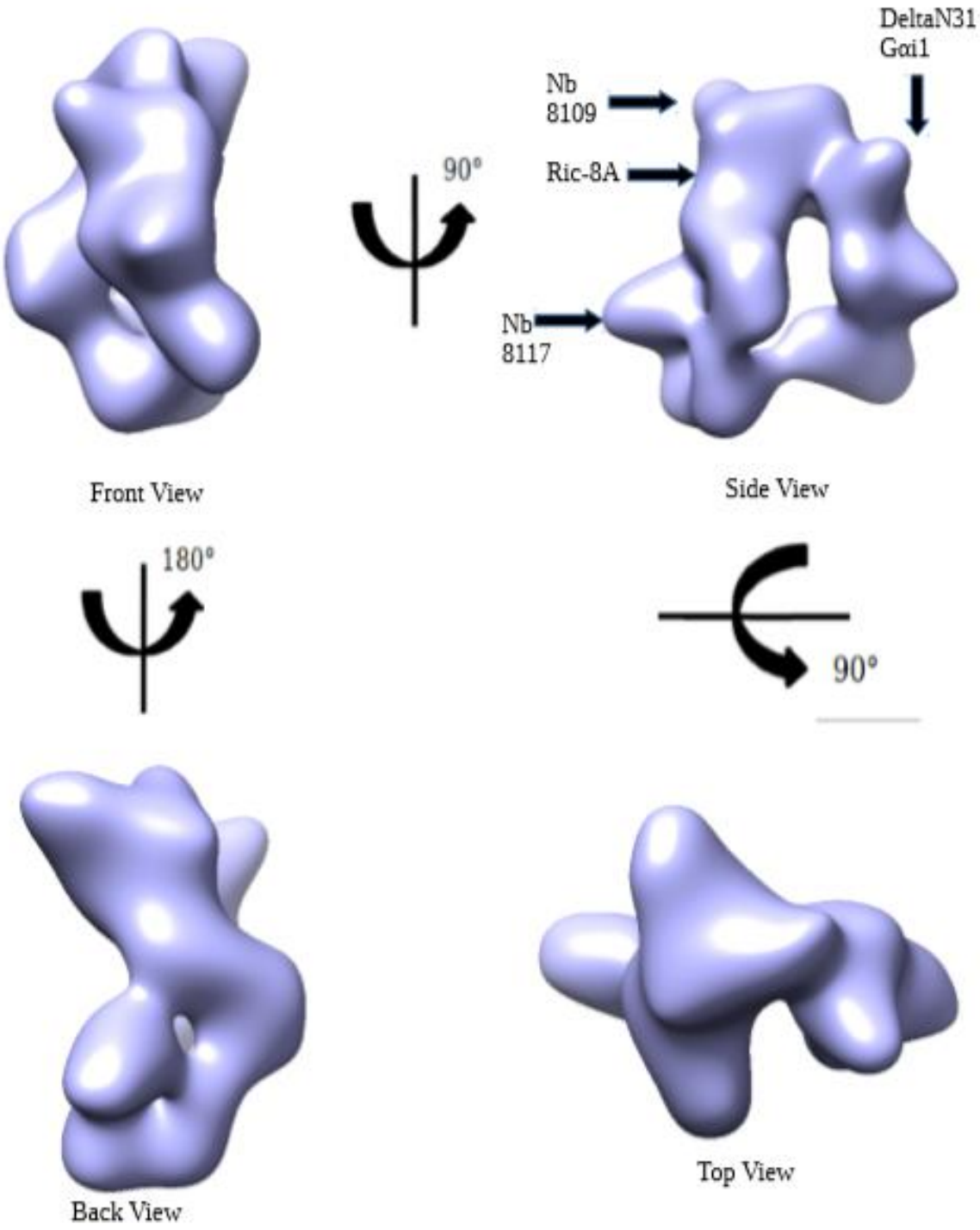

Figure 3.3.3: 3D map generated for the PRic-8A-491:DeltaN31Gαi1:8117:8109 complex frozen with 0.01% NP-40. Differing views of the map are shown, with labels for each of the individual components.

Attempts of performing 3D classification and refinement of this data set ultimately did not yield any usable map. The 2D class averages are shown in Figure 3.3.2 while the 3D map of the OG sample is shown in Figure 3.3.3.

3.5: Cryo-EM analysis of pRic-8A-491:DeltaN31Gαi1:8431:9156 Complex

3.5.1: Micrograph Analysis

The next attempt at increasing the resolution of the maps obtained was to use Nb 8431 and Nb 9156. Nb 8431 is a nanobody that only binds to the Ric-8A:Gαi1 complex, and does not bind to any of the protein components individually. It is thought that Nb 8431 binds at the interface between Ric-8A:Gαi1, such that even the addition of GTP does not dissociate the complex. Of course, Nb 9156 was added to help stabilize the helical domain of Gαi1 to increase the resolution of the complex. The complexes used in this experiment continued with the truncated forms of Ric-8A and Gαi1 to further reduce the flexibility of the complex. To increase the stability of the complex during vitrification, OG, and CHAPS were added prior to vitrification of the samples to reduce their interaction with the air-water interface. The addition of CHAPS before freezing resulted in a very heterogeneous micrograph (see Figure 3.4.1A), though some individual particles close to the predicted size of the complex could be seen. To further determine the state of the complex with CHAPS, approximately 1700 micrographs were collected on the Talos Artica microscope at a total dose of 60 e/A^2 for data processing. The complex containing OG appeared very homogeneous (relative to the sample containing CHAPS), with clear and well distributed particles (see Figure 3.4.2A). Approximately 1500 micrographs were collected of the OG sample on a Talos Arctica microscope at a total dose of 54 e/A^2 for data processing.

3.5.2: Reference Free 2D classification and 3D classification

Reference free 2D classifications and 3D classifications of the pRic-8A 491:DeltaN31Gαi1:8431:9156 Complex data sets was performed in Cryosparc. For the CHAPS sample, approximately 2.4 million particles were initially picked and after multiple rounds of 2D classification about 28,000 particles were left. The 2D class averages were of very low resolution (see Figure 3.4.1B), exhibiting no secondary features. Furthermore, the protein complex appeared damaged in the 2D class averages, most likely caused by the addition of CHAPS and thus, no useful 3D model could be obtained from this data. For the OG sample, approximately 540,000 particles were picked and multiple rounds of 2D

A.

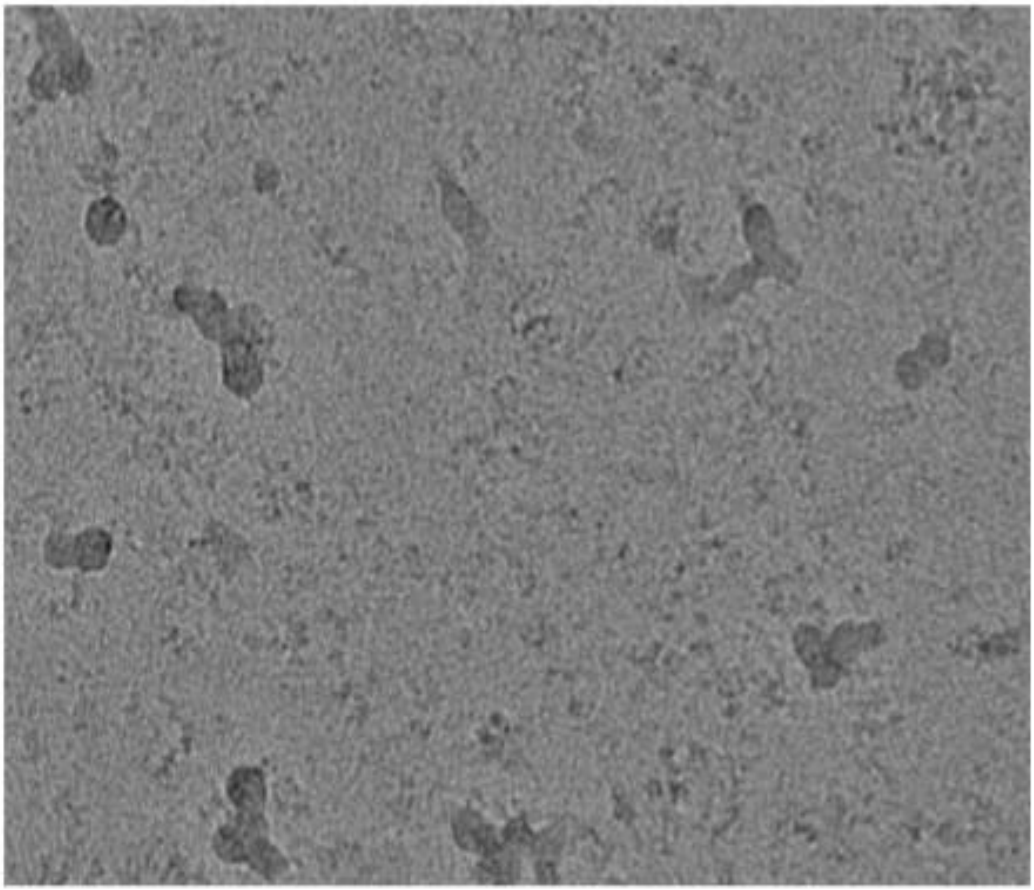

B.

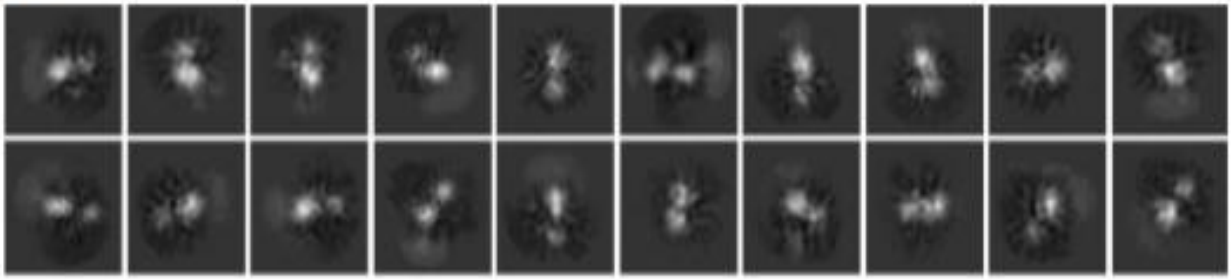

Figure 3.4.1: Micrograph and 2D class averages of Pric-8A-491:DeltaN31Gαi1:8431:9156 with CHAPS A) Micrograph of Pric-8A-491:DeltaN31Gαi1:8431:9156 vitrified with 0.01% CHAPS. B) 2D class averages generated from the micrographs using the Cryosparc software.

A.

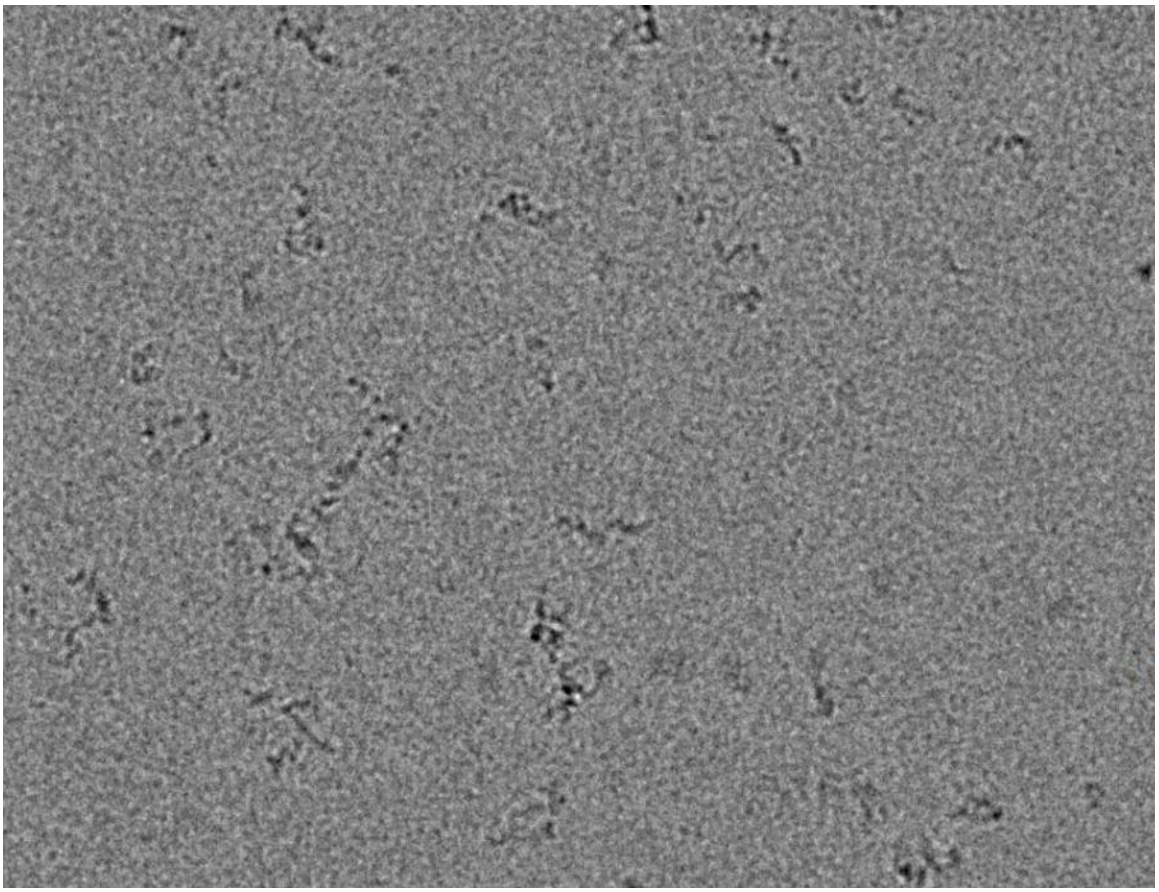

B.

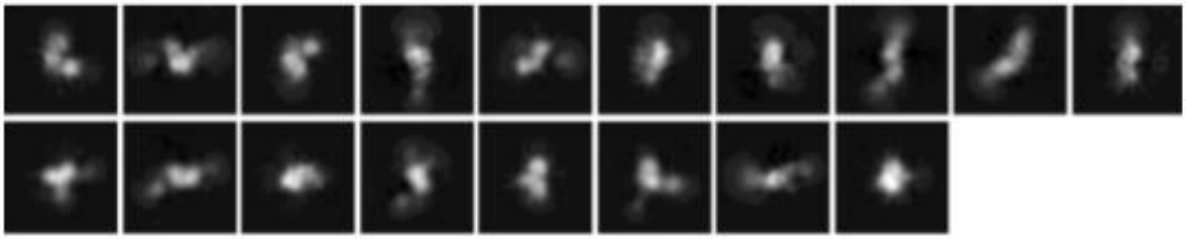

Figure 3.4.2: Micrograph and 2D class averages of Pric-8A-491:DeltaN31Gαi1:8431:9156 with 0.01% OG. A) Micrograph of Pric-8A-491:DeltaN31Gαi1:8431:9156 vitrified with 0.01% OG. B) 2D class averages generated from the micrographs using the Cryosparc software.

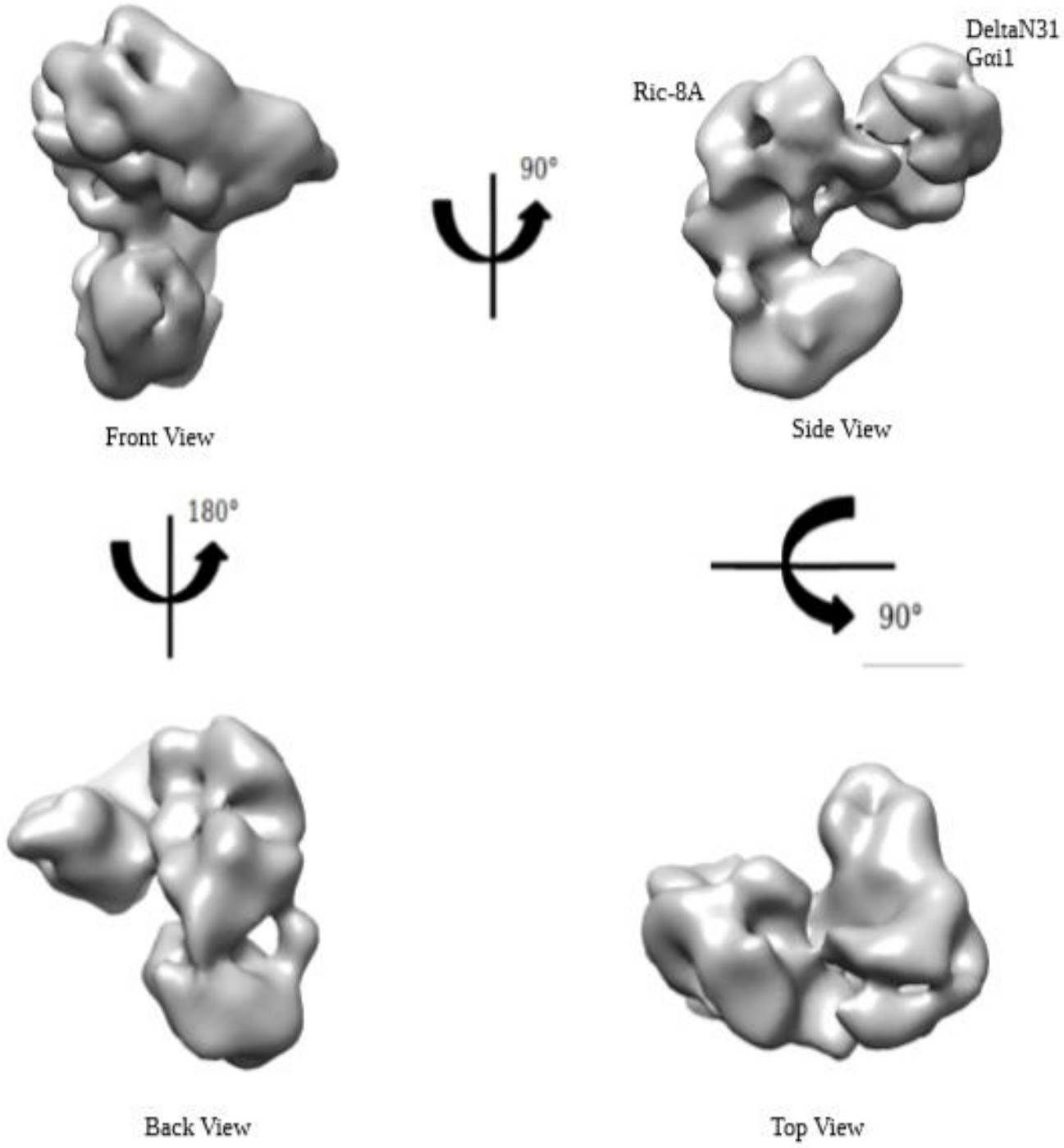

Figure 3.4.3: 3D model generated form the Pric-8A-491:DeltaN31Gαi1:8431:9156 with 0.01% OG dataset. The Ric-8A density is starting to exhibit some secondary structure features. The Gαi1 density is shown with only the ras domain. Nb 8431 and Nb 9156 density could not be observed in the map.

classification was performed, until a final set of 90,000 particles was obtained. The 2D class averages (see Figure 3.4.2B) appeared rather blurry, exhibiting no secondary features, despite having clear and distinguished particles in the micrographs. This may have been due to poor image alignment. 3D classification and refinement of the data resulted in a 13 angstrom map, with density that corresponds to Ric-8A and the ras domain of Gαi1 with some secondary features starting to show on the Ric-8A density (see Figure 3.4.3).

3.6: Cryo-EM analysis of pRic-8A-491:DeltaN31Gαi1:8117:8109:8119

Significant improvements were seen with the Ric-8A-491:DeltaN31Gαi1:8431:9156 complexes, and continued work on this complex may have eventually resulted in a high-resolution map. Though at this time, an approximately 4.0Å crystal structure of pRic-8A-491:DeltaN31Gαi1:8117:8119:8109 (hereon referred to as pR491:DeltaN31Gαi1:3nb) was obtained in the lab. To aid with model building, a high-resolution cryo-EM map of the pR491:DeltaN31Gαi1:3nb was then pursued.

3.6.1: Initial screening of pR491:DeltaN31Gαi1:3nbs on the Talos Arctica

Screening trials for optimal grids of the pR491:DeltaN31Gαi1:3nbs complex was performed on the Talos Arctica microscope. The best vitrification condition for the sample was found to be at 0.3 mg/mL containing 0.01% NP-40 (Figure 3.5.1 A). To determine the quality of the grid, a small data collection was performed on the Arctica microscope. Approximately 1,146 movies were collected at a total dose of 54 e/Å^2 followed by processing in Cryosparc. The 2D class averages generated from the collected data exhibited high-resolution features (protein secondary structure could be seen from 2D class averages) (Figure 3.5.1 B), indicating that the sample could go to high-resolution. Thus, the grid was saved and used for data collection on the Titan Krios to achieve the highest resolution possible for the sample.

3.6.2: Data collection and processing of pR491:DeltaN31Gαi1:3nbs

After screening, collecting data, and processing the data for the pR491:DeltaN31:Gαi1:3nbs grid sample from the Talos Arctica, the grid was placed onto a Titan Krios microscope for a high-resolution data collection. Approximately 7,240 movies were collected at a total dose of 48 e/Å^2 , and were further processed using a combination of Relion and Cryosparc softwares packages (Figure 3.5.2 B). Movies were aligned using motionCor2 and dose-weighting was performed. CTF correction was performed

A.

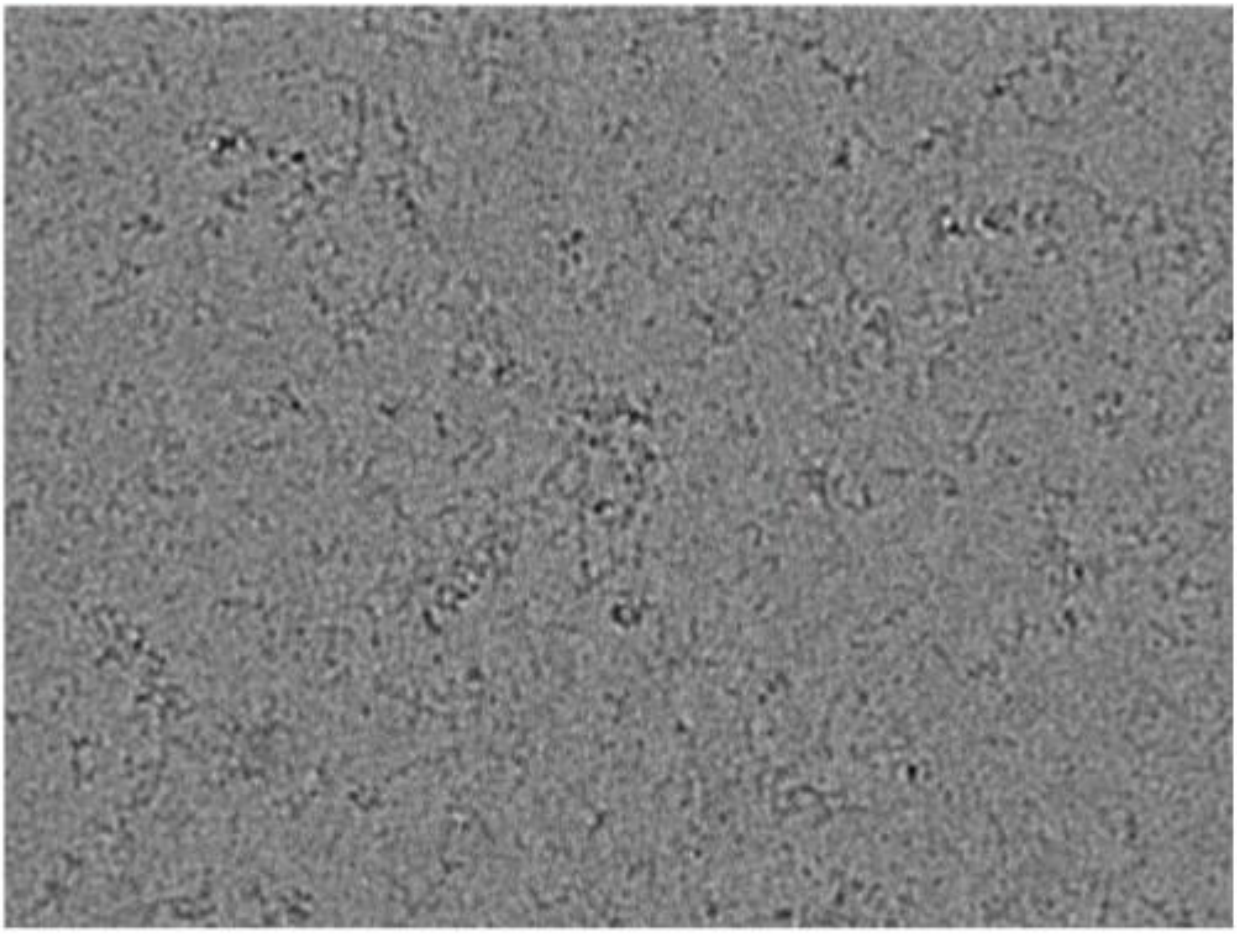

B.

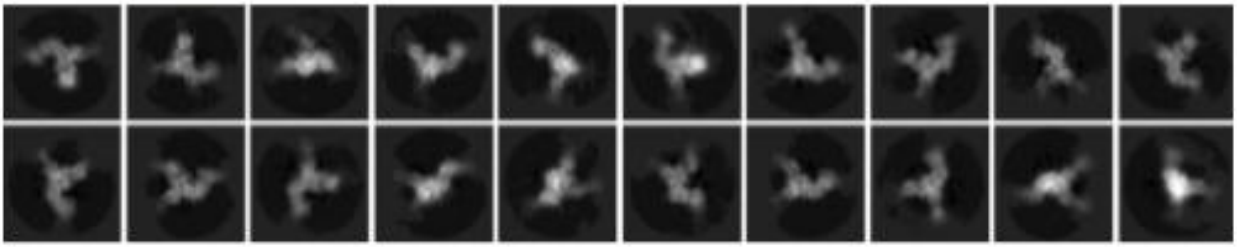

Figure 3.5.1: Micrographs and 2D class averages of PR491:DeltaN31Gαi1:3nbs obtained from screening on the Talos Arctica microscope. A) Micrograph of PR491:DeltaN31Gαi1:3nbs frozen with 0.01% NP-40. B) 2D class averages of PR491:DeltaN31Gαi1:3nbs, generated with cryosparc, displaying protein secondary structure and low background noise.

using CTFFIND 4.1 and micrographs with poorly modeled CTFs were manually removed, leaving 7,186 micrographs. Approximately 4 million particles were automatically picked and manually supervised in Cryosparc using the template picking function. The particles were imported into Relion, where multiple rounds of 2D classification was performed resulting in a total of 627,356 particles. The 2D class averages were generated until protein secondary structures appeared (Figure 3.5.2 A).

An Ab-inito model was generated in Relion and two rounds of 3D classification was performed afterwards. The best 3D classes were selected, resulting in a total of 277,573 particles. Those were then imported into Cryosparc for multiple rounds of hetero-refinement. A total of 169,006 particles were subjected to local CTF refinement. A total of 169,006 particles were subjected to local CTF refinement in Cryosparc and finally, non-uniform refinement in Cryosparc, resulting in a 4.77Å map based on the 0.143 FSC gold-standard curve (Figure 3.5.2 B). Finally, the map was sharpened to show high-resolution features. The 3D map obtained showed clear density for helices along Ric-8A, and density corresponding to Nbs 8117, 8109, and 8119 that could be seen bound to Ric-8A. Density could be observed for the Ras domain of Gαi1, though the helical domain was not present in the map, due to its inherent flexibility (Figure 3.5.3). It is likely that these nanobodies reduced flexible regions on Ric-8A, which inherently increased the stability of the complex, and may have acted to facilitate accurate image alignment.

3.7: Cryo-EM analysis of pR491:DeltaN31Gαi1:8117:8109:8119:9156 complex

A 4.77Å map was obtained for the PR491:DeltaN31Gαi1:3nb complex, though the map lacked the helical domain, most likely due to it's inherent flexibility. Due to the flexibility of the helical domain, resolutions higher then 4.77Å resolution for the complex could not be achieved. To increase the resolution of the complex, nanobody 9156 was added in addition to nanobodies 8119, 8109, and 8117. Nanobody 9156 binds to the helical domain of Gαi1 and thus, would act to reduce the flexibility of the helical domain in the Ric-8A:Gαi1 complex by acting as a sort of weight. This section will discuss the results obtained by adding nanobody 9156 to the complex.

3.7.1: Screening of the pR491:DeltaN31Gαi1:8117:8119:8109:9156 complex

Initial screening for optimal grids of the PR491:DeltaN31Gαi1:4nbs complex sample was performed on the Talos Arctica, similarly to the 3nb complex. The optimal grid condition was found to be at a protein concentration of 0.3 mg/mL containing 0.01% NP-40 (Figure 3.6.1 A). To confirm the quality of the sample, a small data collection was performed on the Talos Arctica microscope. Approximately 1,215 micrographs were collected at a total dose of 69 e/Å^2 and the micrographs were processed with Cryosparc to observe the resulting 2D class averages. The 2D class averages exhibited clear protein secondary structures, with little solvent noise surrounding the protein (Figure 3.6.1 B). The clear 2D class averages obtained from the small dataset collected on the Talos Arctica microscope indicated that the sample was of high quality and thus prompted for a high-resolution data collection on the Titan Krios microscope.

3.7.2: Data collection and processing of the pR491:DeltaN31Gαi1:8117:8109:8119:9156 complex

After screening the pR491:DeltaN31Gαi1:4nb complex on the Talos Arctica, the sample was placed onto the Titan Krios microscope for a high-resolution data collection. A very large data set was collected, comprising a total of 8,670 movie stacks at a total dose of 69 e/Å^2. The movie stacks were aligned using the motionCor2 software and the resulting micrographs were dose-weighted. Micrographs containing poorly modeled CTFs were removed resulting in a final count of 8,456 micrographs. Particles were picked from the micrographs using Topaz particle picking neural network software in Cryosparc, where 865,563 particles were picked. The particles were imported into Relion, where multiple rounds of 2D classification were performed to remove poor 2D class averages, which resulted in a total of 554,244 particles (Figure 3.6.2 A). An initial model was generated in Cryosparc using 49,921 particles, which yielded a model containing the helical domain. The initial model was low pass filtered at 20 Å and was used in Relion for 3D classification. Multiple rounds of 3D classification were performed in Relion yielding 167, 260 total particles. These particles were subjected to non-uniform refinement in Cryosparc resulting in a map with a final resolution of 4.0Å. CTF refinement was then performed in Cryosparc followed by non-uniform refinement again resulting in a map of 3.82 Å resolution based on the gold-standard FSC of 0.143 (Figure 3.6.2 B). The map exhibited high-resolution features, displaying helices and potential side-chains in some regions (Figure 3.6.3 and Figure 3.6.4). The helical domain was resolved in this map, most likely due to the presence of the fourth nanobody bound to the helical domain of Gαi1, which restricted the flexibility of the domain.

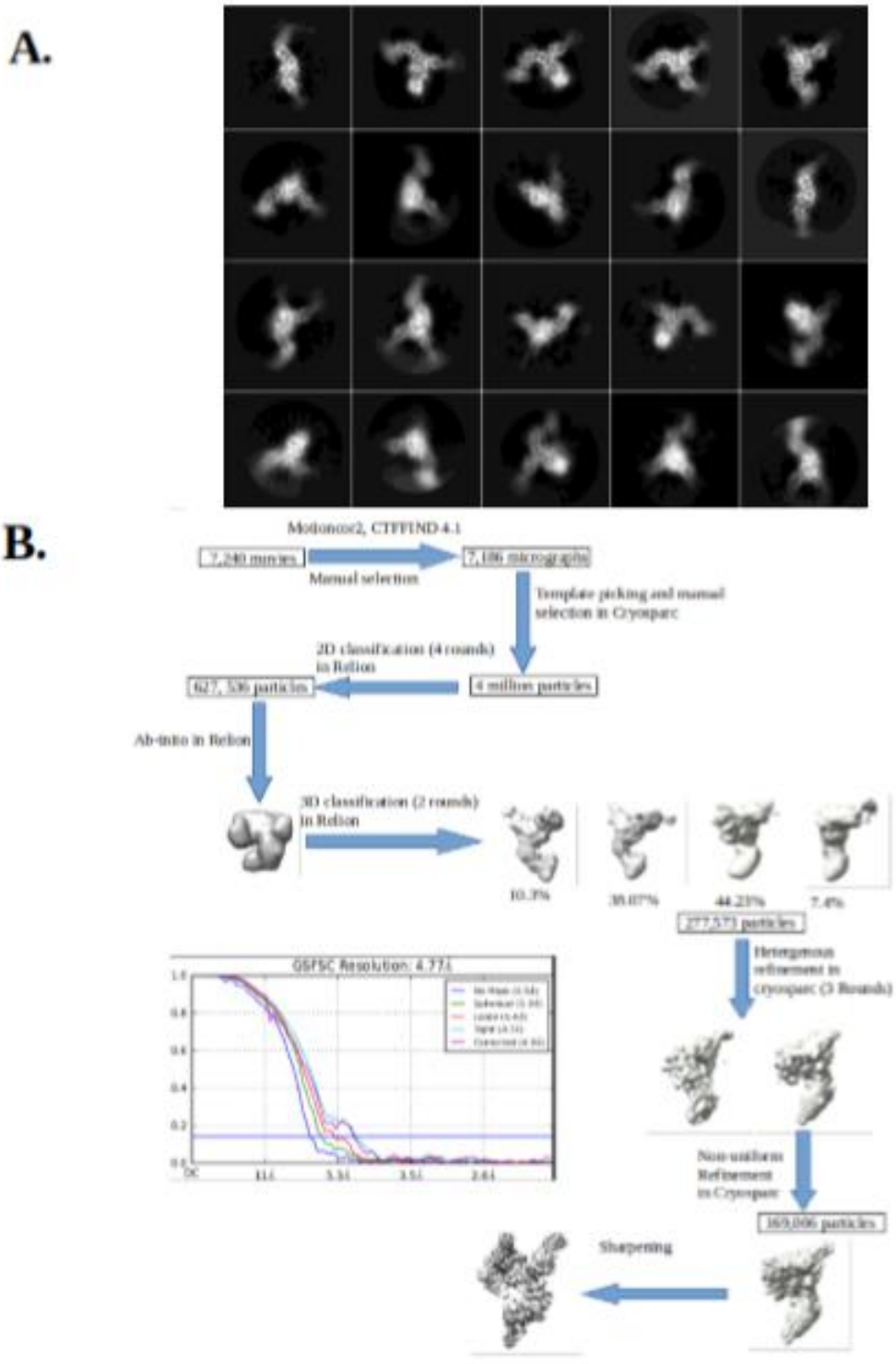

Figure 3.5.2) 2D class averages and processing work-flow for PR491:DeltaN31Gαi1:3nbs. A) 2D class averages in Relion. B) Processing work-flow used for map with the reportedFSC curve obtained.

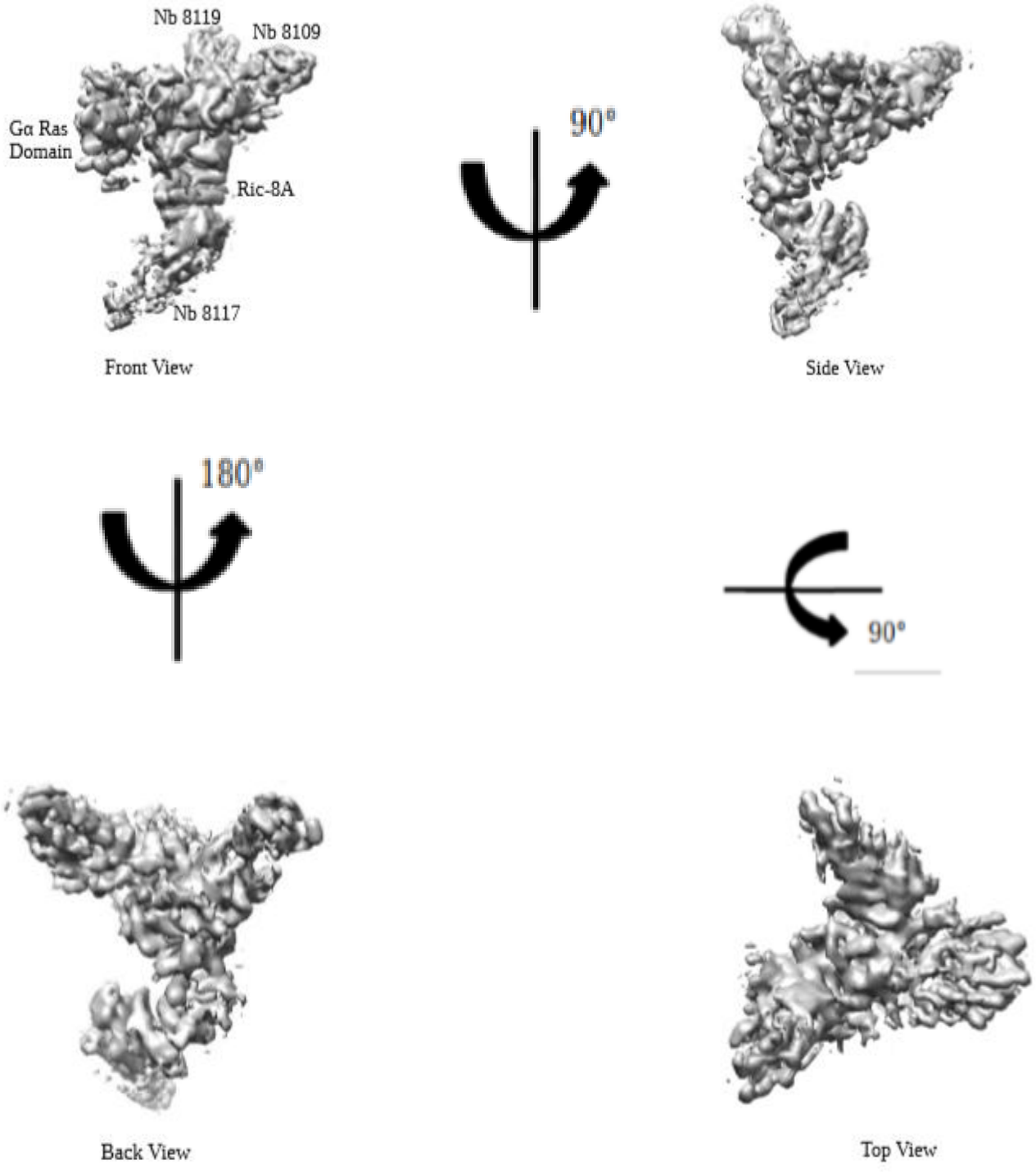

Figure 3.5.3) The 4.77Å map of pR491:DeltaN31Gαi1:3nbs with differing views and each individual component labeled. The helical domain was not observed in the map, and thus, is not shown.

A.

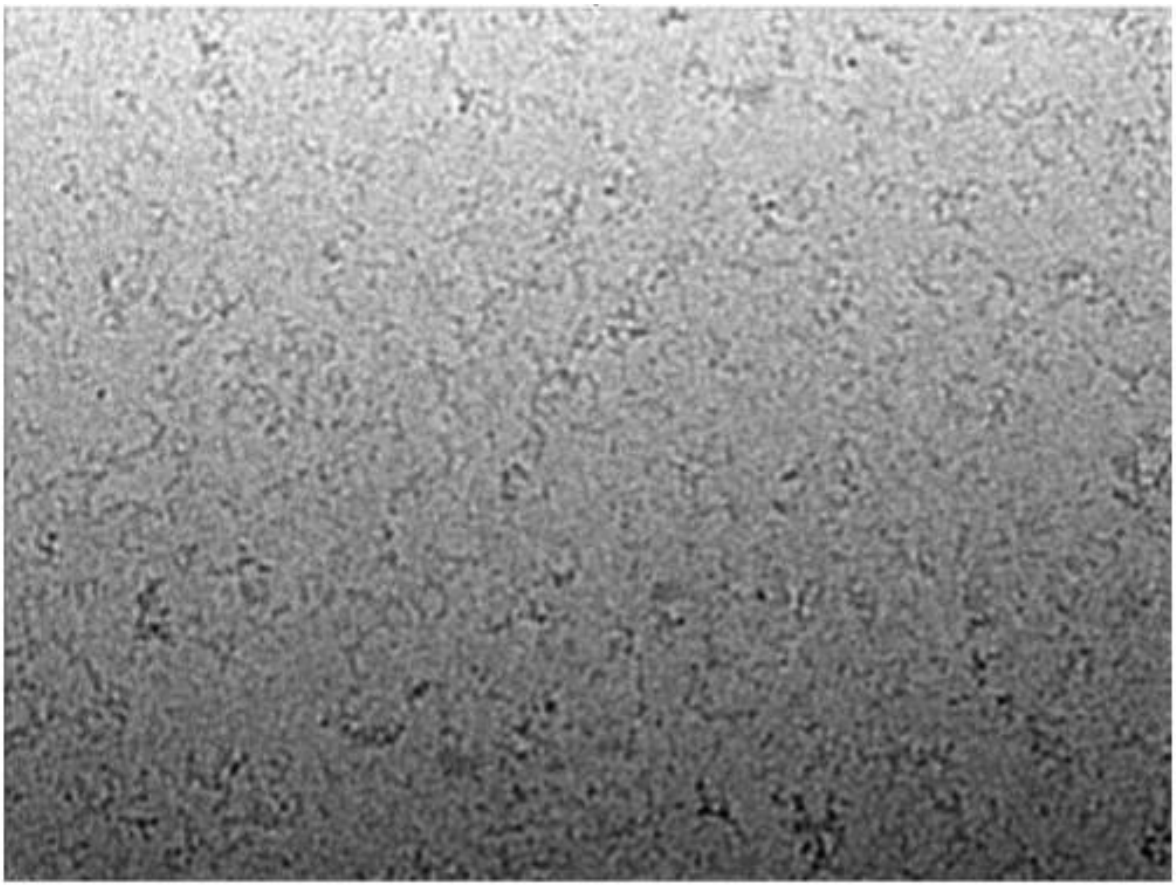

B.

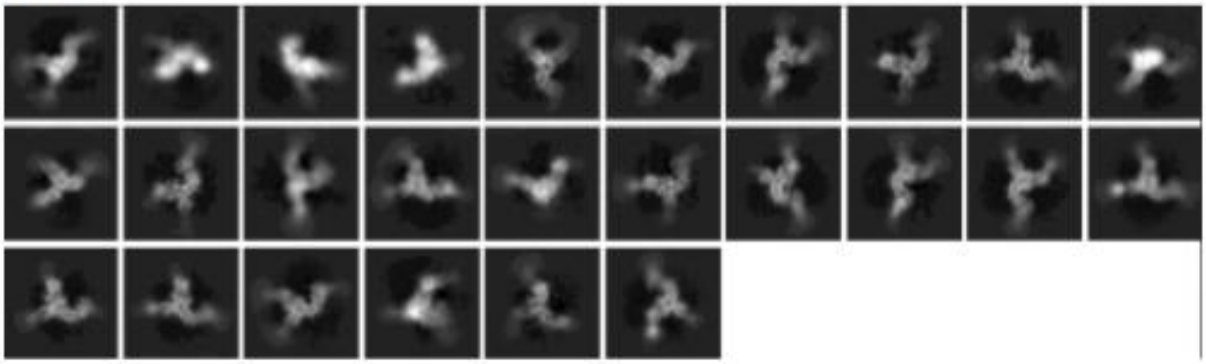

Figure 3.6.1) Representative micrograph and 2D class averages obtained from pR491:DeltaN31Gαi1:4nbs on the Talos Arctica. A) Micrograph of pR491:DeltaN31Gαi1:4nbs on the Talos. B) 2D class averages of pR491:DeltaN31Gαi1:4nbs generated with Cryosparc.

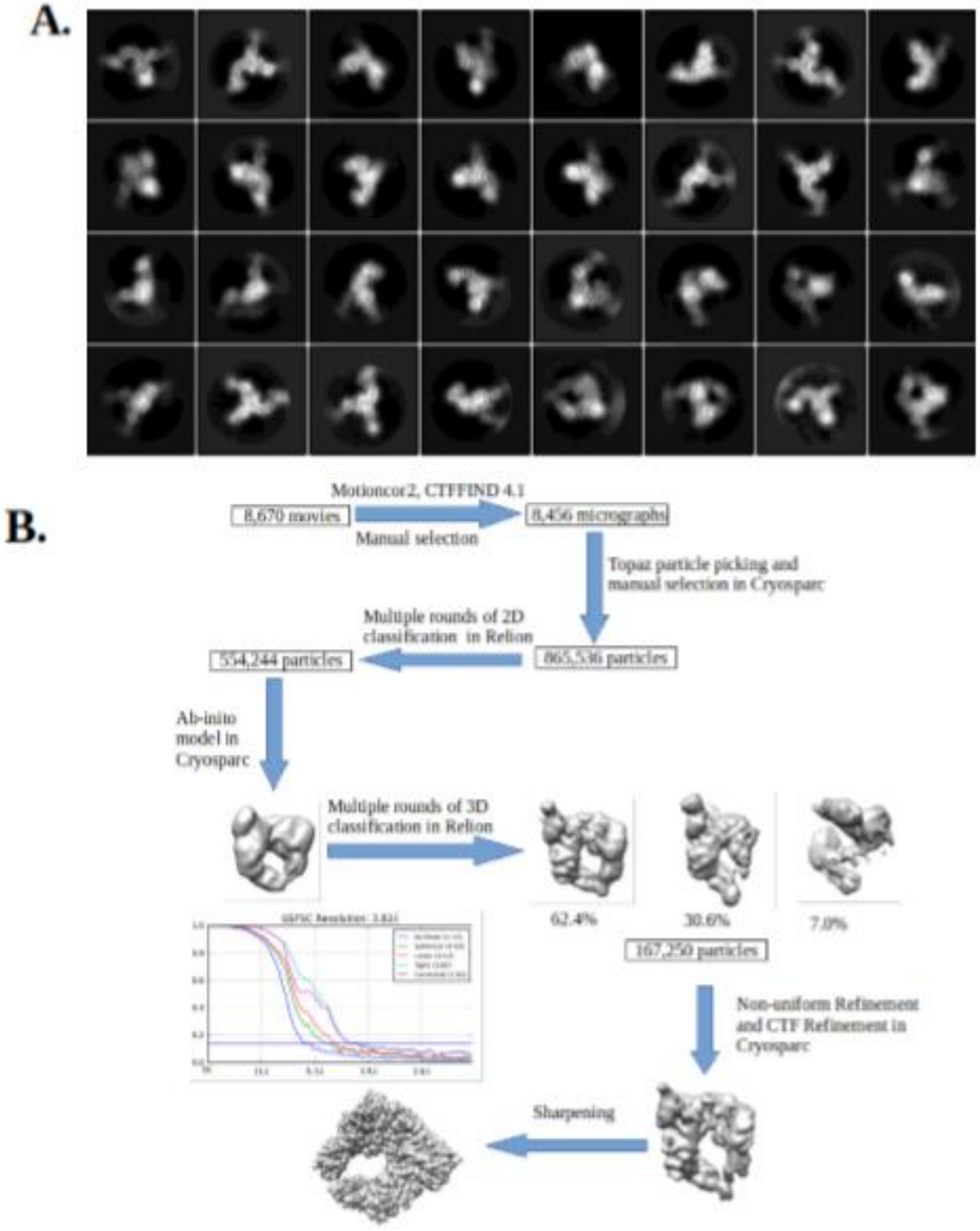

Figure 3.6.2) 2D class averages and processing workflow from the pR491:DeltaN31Gαi1:4nb complex data collected on the Titan Krios. A) 2D class averages of the pR491:DeltaN31Gαi1:4nbs complex from the Titan Krios. B) Processing workflow of the pR491:DeltaN31Gαi1:4nb complex.

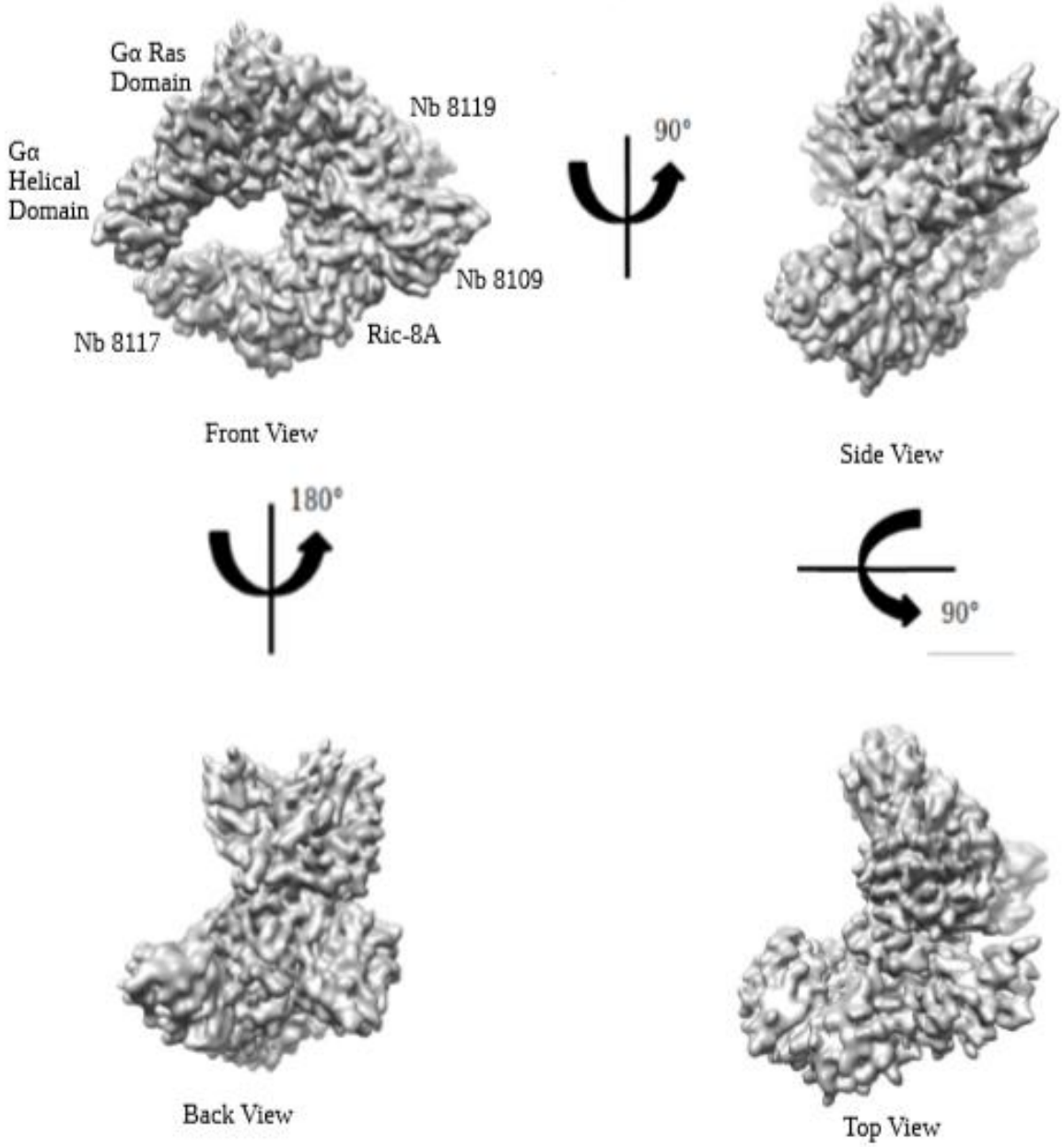

Figure 3.6.3) Differing views of the pR491:DeltaN31Gαi1:4nbs complex map at 3.82Å. The helical domain was observed in the map.

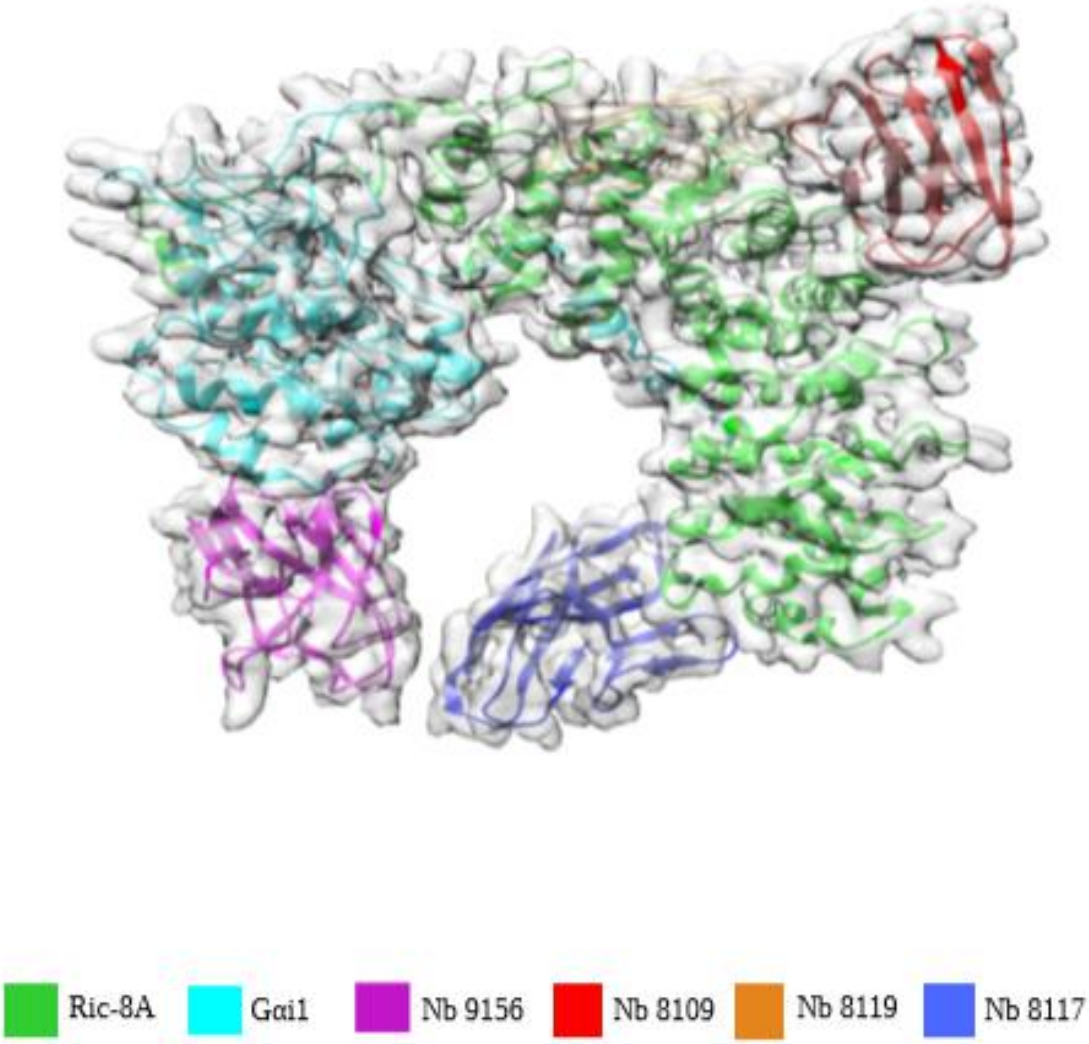

Figure 3.6.4) The 3.8Å map of the pRic8A1-491:DeltaN31Gαi1:4nb complex overlayed with the model generated from the map. Density corresponding to Ric-8A is shown in green, Gαi1 in cyan, Nb 9156 in purple, Nb 8109 in red, Nb 8119 in orange, and Nb 8117 in blue**.**

3.7.3: Chapter summary and conclusions

There was much optimization that was required to obtain a high-resolution map of the Ric-8A:Gα complex that involved sample preparation and differing vitrification conditions. In regards to sample preparation, multiple combinations of nanobodies were used, until the best combination was found that increased the stability of the complex and while aiding in image alignment. Furthermore, various different detergents had to be utilized that could reduce the deleterious effects of the air-water interface, while not inducing aggregation of the complex reducing the number of viable particles present for processing. It is important to note that the map shown in this thesis for pRic-8A:DeltaN31Gαi1:3nb complex was not used for the structure described in Chapter 4.

Chapter 4.
Structure of the Ric-8A:Gα Complex

4.1: Chapter Introduction

The work presented in this thesis has led to a 3.9 angstrom structure of the complex, and thus, this chapter will discuss the structure of the Ric-8A:Gαi1 complex and the insights that have been provided by the structure. In addition, very recent work has also been published by another group of the Full-length phosphorylated Ric-8A:Gαi1 and Ric-8A:Gαq structures, using cryo-EM, without the use of nanobodies to stabilize the complexes (169). The similarities and differences between all of these structures will be discussed along with the differing interpretations obtained from the structures.

4.2: Overall architecture of the cryo-EM Ric-8A:Gα structures

For discussion of the Ric-8A:Gα complex structure, “A”, “B”, and “C” will be used to describe the ARM repeat elements of Ric-8A, while “a” and “b” will be used for the HEAT repeat elements of Ric-8A (see Figure 4.1 for nomenclature). The four nanobody cryo-EM structure obtained from the work in this thesis, comprised of Ric-8A 1-491 and DeltaN31 Gαi1, reveals residues 2-487 of Ric-8A and the entirety of Gαi1 with the exception of the disordered linker (50-76) between the helical and the GTPase domain (168). The two structures determined by *seven et al*, using cryo-EM, was done with phosphorylated full-length Ric-8A bound to full-length Gαi1, and the other complex with the full-length Gαq isoform. Their Ric-8A:Gαi1 structure had Ric-8A residues 1-482 and the ras-like domain of Gαi1 residues (32-54 and 193-354) that were well ordered and easily assigned. The Ric-8A:Gαq complex had residues 1-451 of Ric-8A and residues (217-359) of Gαq that were also well ordered. The final structures of these complexes lacked the entirety of the helical domain, due to its inherent flexibility. The last forty residues of full-length Ric-8A (490-530), predicted to include a coil/beta strand and alpha helix/coil structure, were very disordered but resided close to the weak disordered density observed for the helical domain that jutted away from nucleotide binding site in an average position that is rotated □90° from the nucleotide bound forms of Gαq and Gαi1. Of further note, the N-terminus of Gα were also not observed in their structures from conformational heterogeneity (169).

4.3: Ric-8A interactions with Gα

There are three main interaction sites between Ric-8A and Gα and this is consistent between Gαi1 and Gαq isoform structures determined up to date (168, 169). The first interface of the interaction is formed by the C-terminal helix of Ric-8A (rα11) that contacts the switch II, P-loop, and the α3 helix of the Gα Ras-like domain (Figure 4.2A and D). The second interface is formed by the C-terminal helix (α5 helix)

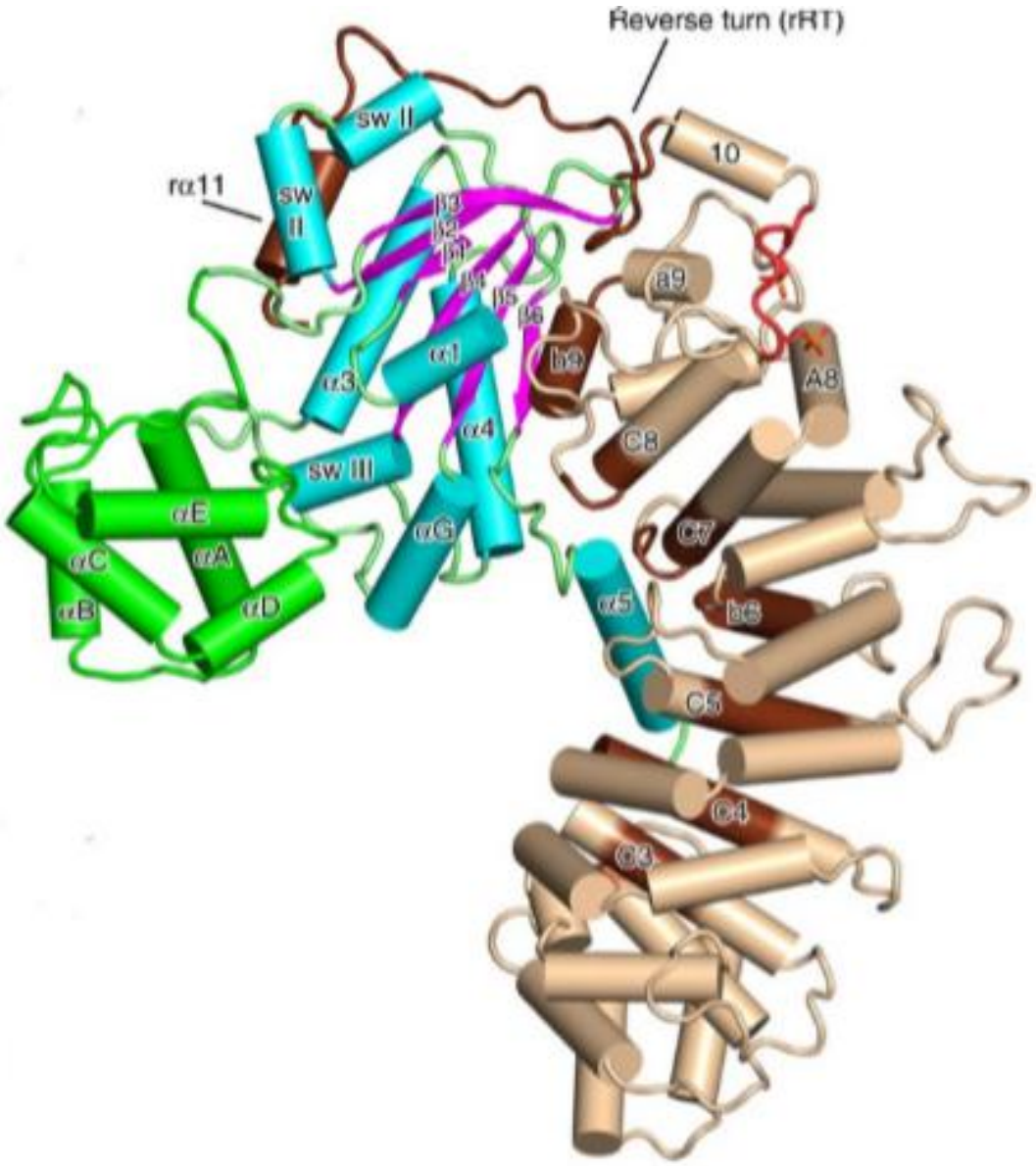

Figure 4.1) Displays the structure of the Ric-8A:Gαi1 complex with the nanobodies omitted. Ric-8A is shown in wheat, while the Gα GTPase domain is colored green and the Ras domain colored cyan. The loop segments of the Gα GTPase domain is colored green and the beta sheets of Gαi1 are colored purple. The segments of Ric-8A that contact Gαi1 are shown in dark brown. Ric-8A residues 335-340 are colored red which include the two phosphorylation sites. The figure was obtained from reference (168).

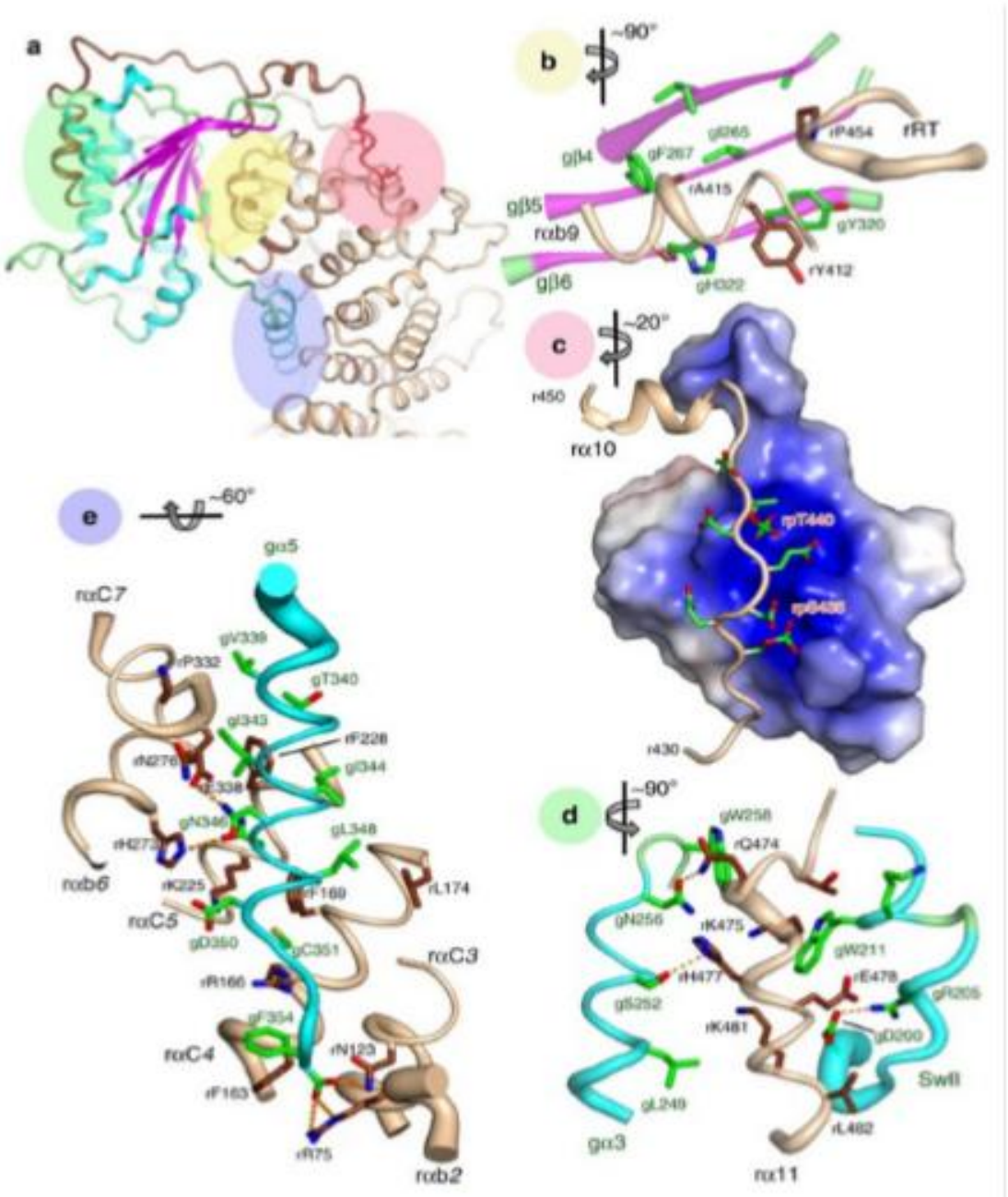

Figure 4.2) A) The major Ric-8A:Gα contact surfaces and phosphorylation sites are highlighted in green, yellow, pink, and blue overlays and these sites are enlarged in panels b-c. B) Interaction between the Gα and the Ric-8A C-terminal ARM/HEAT repeat helix rαbA9 and reverse turn r451–r457 (rRT). C) Acidic Ric-8A peptide with phosphorylated pS335 and pT440 bound to the positively charged surface of Ric-8A. D) Interaction of rα11 with gα3 and Switch II with hydrogen bonds shown as orange dashes. E) Contacts between gα5 and residues in successive ARM/HEAT repeats of Ric-8A. Polypeptide backbones are shown as tubes with carbon atoms of Ric-8A and Gα are shown in brown and green. Oxygen and nitrogen atoms are shown as red and blue. The figure was obtained from reference from (168).

of Gα which interacts with the concave surface of the ARM/HEAT repeats of Ric-8A (Figure 4.2A and E). The third contact region is formed from the Gα β4-β6 sheet with Ric-8A's αb9 Heat repeat (r411–r415) and its reverse turn r451–r457 (rRT) (Figure 4.2A and B). Together these three interactions take up a total of 3200 $Å^2$ solvent accessible surface area as was determined from the Ric-8A:Gαi1 complex (168).

4.4: Ric-8A interacts with the Gα C-terminus that facilitates GDP release

Ric-8A αb9 interacts with and occupies the site of the gα5 helix resulting in a 90^0 degree rotation of the gα5 helix relative to that of Gα bound to a guanine nucleotide (Figure 4.3 A, D). Ric-8A residues Y412, A415, A416, and L418 of αb9 interact to substitute for the gα5 helix and act to stabilize a hydrophobic patch of the Gα β-sheet core (Figure 4.2 B). Near the hydrophobic patch, the αa9 helix of Ric-8A acts to lever the beta hairpin away from the GTPase core (Figure 4.3 A). The β1-β5 undergo a 5^o counter-clockwise when viewed from the concave surface of the Gα β-sheet. The conformational changes that occur with the β1-β3 induce partial disorder of Gα. The gα5 helix connects to the β6 strand by a loop that contains the TCAT motif, which is important for coordinating the guanine nucleotide base of GDP or GTP in the Ras-like domain of Gα. The displacement of the gα5 helix causes the TCAT motif to move away from its nucleotide coordination site (Figure 4.3 B). This structural change also perturbs the conserved NKKD motif, located between β4-αG of Gα, which is required for specificity of guanosine nucleotides. Together, these conformational changes trigger the separation of the helical and Ras-like domains (168, 169).

4.5: Gα C-terminus binds to the Ric-8A ARM repeat trough

The α5 helix of Gα binds along the concave surface of Ric-8A and interacts with helices αb2 through αB8. Highly conserved hydrophobic residues in the gα5 helix (F336, V339, I344, I343, and L348) mediate side-chain packing interactions with Ric-8A. Furthermore, the interaction of the α5 helix with Ric-8A is further driven by polar interactions that include hydrogen bonds from N346 in Gαi1 (N352 in Gαq) and H273 in Ric-8A. The last carboxyl group of Gα (F354 for Gαi1 and V359 for Gαq) interacts with Ric-8A residues R71, R75, and N123 (168, 169). These interactions are shown in Figure 4.2 E.

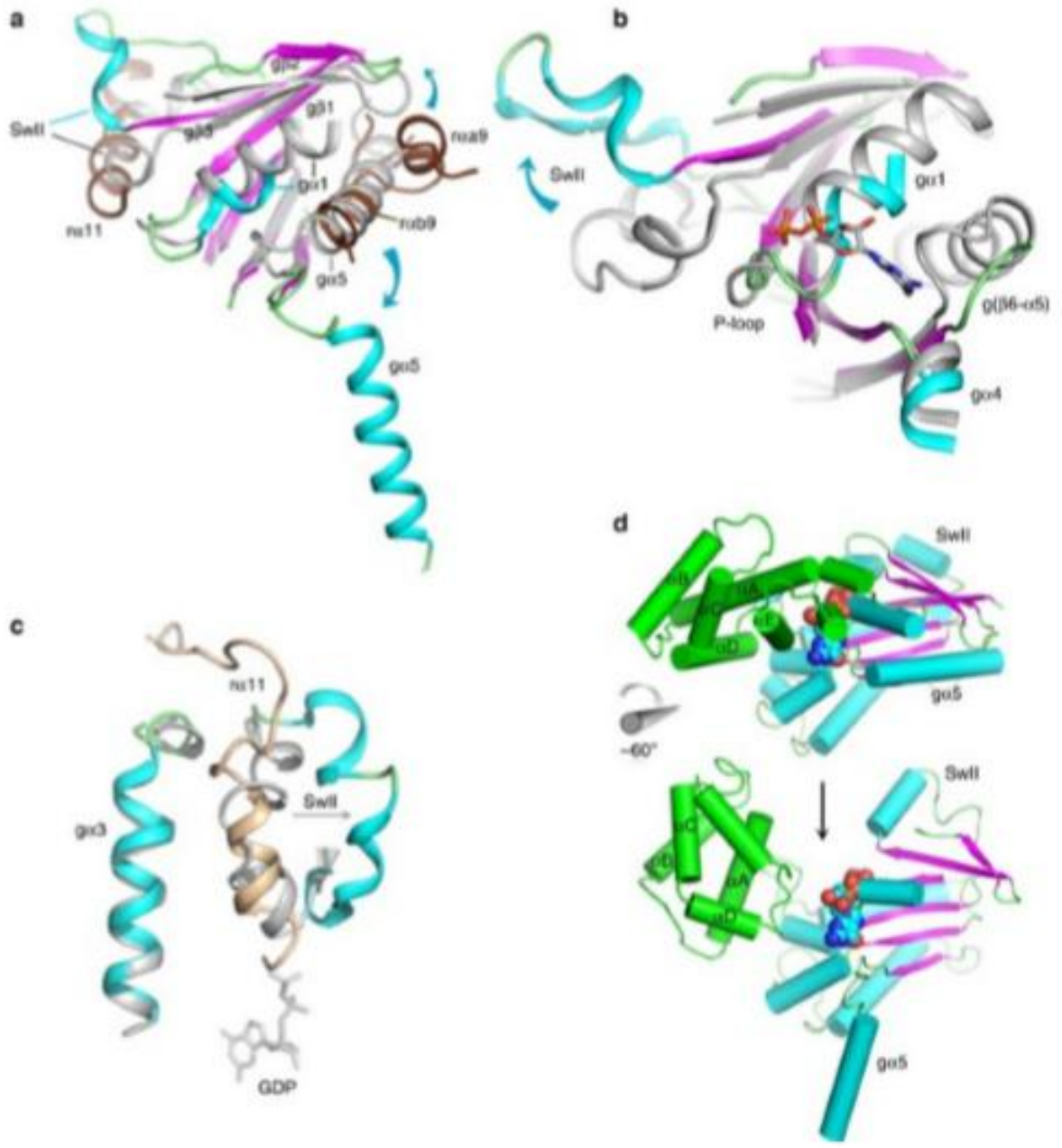

Figure 4.3) Conformational changes induced in Gα by Ric-8A. A) Conformational changes due to binding of Ric-8A αa9, αb9, and RT to Gαi1. B) Ric-8A-induced conformation changes dismantle the Gα nucleotide-binding site. GDP from 1GIT is included as a stick model for reference. C) Displacement of Switch II by rα11. The position of GDP bound to Gαi1•GDP is shown as a stick model. D) Ric-8A-induced rotation of the helical domain away from the GTPase domain of Gα: top, Gαi1•GDP (1GIT) rendered with helices as cylinders and β-strands as ribbons and the helical domain colored green; atoms of GDP are rendered as spheres. The figure was obtained from reference (168).

4.6: The role of Ric-8A phosphorylation with Ric-8A:Gα complexes

Phosphorylation at residues S435 and T440 by CK2 act to facilitate GEF activity through a structural mechanism that was previously unresolved. These two phosphorylated residues reside on an extended C-terminal coil region of Ric-8A close to the ARM/HEAT domain. Ric-8A αb9 and RT (reverse turn), which interact with the beta sheet of Gα, are connected by an intrinsically disordered sequence 430-440 which is followed by the Ric-8A α10 helix, respectively. Neither S435 or T440 interact directly with Gα though rather form multiple ionic interactions along an electropositive groove with conserved arginine and lysine residues (R348, R345, K349, K352, and R405) on Ric-8A (Figure 4.2 C). These ionic interactions help to immobilize the 430-450 connector of Ric-8A to stabilize the interaction of αb9 and RT with β4-β6 of Gα. Furthermore, it was shown that phosphorylation at S435 and T440 increased the thermal stability of Ric-8A in the absence of Gα potentially suggesting that Ric-8A adopts a more stable and compact conformation (169).

4.7: Ric-8A interacts with the Gα switch II and α3 regions

The Ric-8A helix α11 (residues 471-491 of the Ric-8A-491 structure) packs between the Gα switch II and α3 region (Figure 4.3 C). These two elements form the effector protein binding sites of Gα bound to GTP. Interestingly, the α11 helix occupies the position of the switch II in the G-protein heterotrimer, Gαi1 bound to GTP analogs, and in the Gαi1•GDP•Pi product complex (Figure 4.3 C). Furthermore, mutations at residues E478 and L482 in the α11 helix reduced GEF activity (168). The interaction of the α11 helix of Ric-8A with the Gα switch II and α3 region was present in both the Gαi1 and Gαq complex structures (169).

4.8: Ric-8A induces a conformational change to the Gα helical domain

Ric-8A causes the displacement of the α5 helix of Gα and re-orients the β2-β3 sheets of Gα that effectively disrupts stabilization interactions required for nucleotide binding (Figure 4.3 A). These conformational changes result in a loss of contacts between the helical and ras-like domain of Gα. The helical domain, as obtained from the Ric-8A:DeltaN31Gαi1:4nb structure, displays an approximate 60^{o} degree rotation of the helical domain around an axis aligned with αD of Gα (Figure 4.3 D). This conformational change results in the formation of a channel between the helical and Ras-like domain that allows the release of the nucleotide. The magnitude of this change was much lower then that observed for G-protein coupled receptor GEF activity, most likely due to steric hindrance from the

nanobody bound to the helical domain. Indeed, Ric-8A bound to Gαi1 or Gαq did not exhibit any density for the helical domain due to its conformational flexibility, though a little density in the early stages of processing were observed approximately 90^{o} away relative to nucleotide bound Gαi1 or Gαq (168).

4.9.1: Gα subtype selectivity by Ric-8A and Ric-8B

The binding of the α5 helix of Gαi1 and Gαq to Ric-8A share very similar interfaces, though despite this, there are a few different contact residues as observed from the the cryo-EM structures of the Ric-8A:Gαq and Ric-8A:Gαi1 complexes (169). Ric-8A accommodates these differences by reorientation of side chains, conformational changes that adjust the binding groove in the concave surface of the protein, and the formation of alternative backbone interactions. These variations result in differing surface contact surface areas between the last 23 terminal residues of Gαq and Ric-8A (2,780 Å^2) or Gαi1 (2,201 Å^2). The difference in contact regions between Gαq and Gαi1, suggests that Ric-8A is able to adjust the size of it's concave groove to accommodate differing Gα isotypes (169). To understand Ric-8B selectivity, an homology model was generated of a Ric-8B:Gαs complex and was compared to the Ric-8A:Gαq and Ric-8A:Gαi1 complexes (169). Superposition of the Ric-8B:Gαs, generated with homology modeling, with the cryo-EM structures of Ric-8A:Gαq or Ric-8A:Gαi1 complexes showed that differences with the amino acid compositions of the α5 helix of Gαs is not compatible with Ric-8A (169). The differences in amino acid compositions of the Gαs α5 helix may create clashes and repulsions with that of Ric-8A which results in inhibition of complex formation. The major difference found was a swap of the side chains of N347 (Gαi1) and H273 (Ric-8A). In Gαs, N347 is replaced with residue H387, which creates a steric clash with residue H273 of Ric-8A. Ric-8B contains an asparagine (N280) at the corresponding position which may enable a polar interaction with H387 of Gαs. In addition, a second steric clash was proposed (169), between Q384 of Gαs and F232 of Ric-8A. Ric-8B possesses a smaller side chain (V239), at a homologous position, which would enable Ric-8B binding. Thus, it is likely that the interactions of the α5 helix of Gα with Ric-8 determines specificity between differing isoforms (88).

4.9.2: Ric-8 primes Gα for GTP binding

There is an extensive interface formed between Ric-8A with Gα, which raises the question of how Gα is released from Ric-8A in response to GTP. The P-loop is slightly displaced by the α11 helix of Ric-8A, though the conformation of the P-loop still remains largely the same (Figure 4.3 B). Due to a lack of a conformational change of the P-loop, the P-loop is still available for subsequent binding to GTP. The electrostatic repulsion between the C-terminus of the Ric-8A α11 helix and the γ phosphate of GTP could promote the release of the α11 helix. This would in turn, allow the switch II region to refold into it's native GTP bound conformation. Indeed, GTP containing three phosphates relative to the two phosphates in GDP would exhibit higher affinity relative to the latter. The cell also contains 10-fold higher concentration of GTP relative to GDP, so it is likely that this has caused Ric-8A to develop into a GTP regulated chaperone for Gα subunits (169). Disruption of the switch II interactions with Ric-8A would restore the native structure of the Gα β2-β3 regions and would destabilize the interaction between Ric-8A and Gα. More work is required to understand the dynamics that accompany Ric-8A binding to Gα:GDP and Ric-8's release from Gα:GTP.

4.9.3: Conclusions and future Directions

In this study, a relatively high resolution structure of Ric-8A:Gαi1 was obtained at 3.85 Å. By combining various methods for sample optimization, such as trying various combinations of nanobodies and truncated forms of Ric-8A and Gαi1. Much work was done in finding the best vitrification conditions such that, complex dissociation would not occur at the air-water interface. This was done by either trying different nanobodies or different detergent types such as OG, CHAPS, and NP-40. The complex was on the small side for cryo-EM, at around 160 kilodaltons, though was still well-within the current range to obtain a high-resolution map. Due to the small size of the protein complex, it was very difficult to determine the quality of the grids just from visualization alone. To determine the quality of the grids, it was necessary to collect a small dataset and processing was required to assess the quality of the grids. While in some cases, direct visualization was sufficient, where high-background was present, i.e, small proteins corresponding to individual components of the complex. Interestingly, Ric-8A complex stabilization with NB 8431 and NB 9156 appeared rather homogeneous, with little to no background present, and thus, appeared very promising from direct visualization. Despite this, processing of the data resulted in a low-resolution map though improvement was seen relative to other datasets collected at the time.

The pRic-8A-491:DeltaN31Gαi1:3nb complex, frozen with 0.01% NP-40, resulted in a high resolution map at 4.8 Å resolution. It is likely that the nanobodies had three major factors for improving resolution in this structural analysis, which included providing features for facilitating image alignment during 2D or 3D classification, providing stability and reducing complex dissociation, and reducing overall inherent flexibility of the complex. The Ric-8A-491:DeltaN31Gαi1:3nb map showed clear density for Ric-8A, with helices clearly showing, and density for the Ras-like domain of Gαi1 along with density showing the nbs bound. Despite the high-resolution map obtained, no clear density could be observed for the helical domain of Gαi1, indicating the conformational flexibility of the domain. To restrain the domain for structural analysis, a fourth nanobody which binds to the helical domain of Gαi1, was added to reduce the conformational flexibility of the helical domain. Indeed, this increased the resolution of the pRic-8A:DeltaN31Gαi1 complex from 4.8 Å to 3.85 Å and resolved the helical density of Gα, which was not resolved in cryo-EM structures without nanobodies (169). The nanobody 9156, likely restrained the flexibility of the Gα helical domain, and thus, facilitating effective structural determination of the domain.

The structure of the complex obtained from this study revealed many insights into the structural mechanism of Ric-8A GEF and chaperone activity. The structure showed that phosphorylation of Ric-8A at residues S435 and T440 act as molecular staples bound by electrostatic interactions onto Ric-8A itself. Ric-8A disrupts the nucleotide binding region of Gα, which facilitates nucleotide release, and also primes Gα for binding to GTP resulting in its activation. While this study has provided much insights as to how Ric-8A functions as a GEF and a molecular chaperone for Gα subunits, more work is necessary to understand the dynamics of nucleotide release. Furthermore, it is not utterly clear how Ric-8A and Ric-8B exhibit specificity toward different Gα subunits, and thus, a clear direction would be to elucidate a high-resolution structure of the Ric-8B:Gαs complex. Also, noteworthy, is whether which of the three contacts of Ric-8A and Gα is responsible entirely for its GEF activity or as a molecular chaperone and thus, further work needs to be done to determine this.

References

1) Berg JM, Tymoczko JL, Stryer L. Biochemistry. 5th edition. New York: W H Freeman; 2002. Chapter 3, Protein Structure and Function.
2) Uings, I. J., & Farrow, S. N. (2000). Cell receptors and cell signalling. *Molecular pathology : MP*, *53*(6), 295–299.
3) Hanlon, C. D., & Andrew, D. J. (2015). Outside-in signaling--a brief review of GPCR signaling with a focus on the Drosophila GPCR family. *Journal of cell science*, *128*(19), 3533–3542. doi:10.1242/jcs.175158
4) Rasmussen, S. G. F., DeVree, B. T., Zou, Y., Kruse, A. C., Chung, K. Y., Kobilka, T. S., … Kobilka, B. K. (2011). Crystal structure of the β_2 adrenergic receptor–Gs protein complex. *Nature*, *477*(7366), 549–555.
5) Clapham DE, Neer EJ. Ann. Rev. Pharmacol. Toxicol. 1997;37:167.
6) Nestler EJ, Duman RS. Heterotrimeric G Proteins. In: Siegel GJ, Agranoff BW, Albers RW, et al., editors. Basic Neurochemistry: Molecular, Cellular and Medical Aspects. 6th edition. Philadelphia: Lippincott-Raven; 1999
7) Syrovatkina, V., Alegre, K. O., Dey, R., & Huang, X. Y. (2016). Regulation, Signaling, and Physiological Functions of G-Proteins. *Journal of molecular biology*, *428*(19), 3850–3868. doi:10.1016/j.jmb.2016.08.002
8) Taussig, R. and Gilman, A.G. (1995) J.Biol.Chem. 270, 1-4
9) Milde M, Rinne A, Wunder F, Engelhardt S, Bünemann M
Biochem J. 2013 Sep 15; 454(3):515-23
10) Rebecchi, M., and Pentylana, S. (2000) *Physiol. Rev.* **80**, 1291-1335
11) Runnels, L. W., and Scarlata, S. F. (1998) *Biochemistry* **37**,15563-15574
12) Kozasa T, Jiang X, Hart MJ, Sternweis PM, Singer WD, Gilman AG, Bollag G and Sternweis PC . (1998). *Science*, **280**, 2109–2111.
13) Fukuhara S, Chikumi H and Gutkind JS . (2000). *FEBS Lett.*, **485**, 183–188.
14) Fukuhara S, Murga C, Zohar M, Igishi T and Gutkind JS . (1999). *J. Biol. Chem.*, **274**, 5868–5879.
15) Wedegaertner P. B., Wilson P. T. and Bourne H. R. (1995) Lipid modifications of trimeric G proteins. J. Biol. Chem. **270**: 503–506
16) Peitzsch R. M. and McLaughlin S. (1993) Binding of acylated peptides and fatty acids to phospholipid vesicles: pertinence to myristoylated proteins. Biochemistry **32**: 10436–10443
17) Grassie M. A., McCallum J. F., Guzzi F., Magee A. I., Milligan G. and Parenti M. (1994) The palmitoylation status of the G-protein G(o)1 alpha regulates its activity of interaction with the plasma membrane. Biochem. J. **302**: 913–920
18) Galbiati F., Guzzi F., Magee A. I., Milligan G. and Parenti M. (1994) N-terminal fatty acylation of the alpha-subunit of the G-protein Gi1: only the myristoylated protein is a substrate for palmitoylation. Biochem. J. **303**: 697–700
19) Mumby S. M., Kleuss C. and Gilman A. G. (1994) Receptor regulation of G-protein palmitoylation. Proc. Natl. Acad. Sci. USA **91**: 2800–2804
20) Kisselev O., Ermolaeva M. and Gautam N. (1995) Efficient interaction with a receptor requires a specific type of prenyl group on the G protein gamma subunit. J. Biol. Chem. **270**: 25356–25358
21) Moffett S., Brown D. A. and Linder M. E. (2000) Lipid-dependent targeting of G proteins into rafts. J. Biol. Chem. **275**: 2191–2198

22) Myung C. S., Yasuda H., Liu W. W., Harden T. K. and Garrison J. C. (1999) Role of isoprenoid lipids on the heterotrimeric G protein gamma subunit in determining effector activation. J. Biol. Chem. **274**: 16595–16603
23) Dohlman H. G., Song J., Ma D., Courchesne W. E. and Thorner J. (1996) Sst2, a negative regulator of pheromone signaling in the yeast Saccharomyces cerevisiae: expression, localization and genetic interaction and physical association with Gpa1 (the G-protein alpha subunit). Mol. Cell. Biol. **16**: 5194–5209
24) Coleman DE, Berghuis AM, Lee E, Linder ME, Gilman AG, Sprang SR. Structures of active conformations of Gi alpha 1 and the mechanism of GTP hydrolysis. *Science*. 1994;265(5177):1405-1412.
25) Noel, J., Hamm, H. & Sigler, P. The 2.2 Å crystal structure of transducin-α complexed with $GTP_{\gamma}S$. *Nature* **366,** 654–663 (1993).
26) Mixon, M. B., Lee, E., Coleman, D. E., Berghuis, A. M., Gilman, A. G., & Sprang, S. R. (1995). Tertiary and Quaternary Structural Changes in Gialpha Induced by GTP Hydrolysis. *Science*, *270*(5238), 954–960.
27) Wall, M. A., Coleman, D. E., Lee, E., Iñiguez-Lluhi, J. A., Posner, B. A., Gilman, A. G., & Sprang, S. R. (1995). The structure of the G protein heterotrimer Gi alpha 1 beta 1 gamma 2. *Cell*, *83*(6), 1047–1058.
28) Masters, S. B., Stroud, R. M., & Bourne, H. R. (1986). Family of G protein alpha chains: amphipathic analysis and predicted structure of functional domains. *Protein Engineering*, *1*(1), 47–54.
29) Landis, C., Masters, S., Spada, A. *et al.* GTPase inhibiting mutations activate the α chain of G_S and stimulate adenylyl cyclase in human pituitary tumours. *Nature* **340,** 692–696 (1989) doi:10.1038/340692a0
30) Markby, D., Onrust, R., & Bourne, H. (1993). Separate GTP Binding and GTPase Activating Domains of a Gα Subunit. *Science*, *262*(5141), 1895-1901.
31) Rodbell, M. (1992). The Role of GTP-Binding Proteins in Signal Transduction: From the Sublimely Simple to the Conceptually Complex. In E. R. Stadtman, P. B. Chock, & A. Levitzki (Eds.), *Current Topics in Cellular Regulation* (Vol. 32, pp. 1–47).
32) Codina, J., & Birnbaumer, L. (1994). Requirement for intramolecular domain interaction in activation of G protein alpha subunit by aluminum fluoride and GDP but not by GTP gamma S. *Journal of Biological Chemistry*, *269*(47), 29339–29342.
33) Ridge, K. D., Abdulaev, N. G., Sousa, M., & Palczewski, K. (2003). Phototransduction: crystal clear. *Trends in Biochemical Sciences*, *28*(9), 479–487.
34) Wittinghofer, A., & Vetter, I. R. (2011). Structure-Function Relationships of the G Domain, a Canonical Switch Motif. *Annual Review of Biochemistry*, *80*(1), 943–971.
35) Sprang, S. R. (1997). G PROTEIN MECHANISMS: Insights from Structural Analysis. *Annual Review of Biochemistry*, *66*(1), 639–678.
36) Vetter, I. R., & Wittinghofer, A. (2001). The guanine nucleotide-binding switch in three dimensions. *Science (New York, N.Y.)*, *294*(5545), 1299–1304.
37) Siderovski, D. P., & Willard, F. S. (2005). The GAPs, GEFs, and GDIs of heterotrimeric G-protein alpha subunits. *International Journal of Biological Sciences*, *1*(2), 51–66.
38) Bos, J. L., Rehmann, H., & Wittinghofer, A. (2007). GEFs and GAPs: Critical Elements in the Control of Small G Proteins. *Cell*, *129*(5), 865–877.
39) Boriack-Sjodin, P. A., Margarit, S. M., Bar-Sagi, D., & Kuriyan, J. (1998). The structural basis of the activation of Ras by Sos. *Nature*, *394*(6691), 337–343.

40) Worthylake, D. K., Rossman, K. L., & Sondek, J. (2000). Crystal structure of Rac1 in complex with the guanine nucleotide exchange region of Tiam1. *Nature*, *408*(6813), 682–688.
41) Renault, L., Kuhlmann, J., Henkel, A., & Wittinghofer, A. (2001). Structural Basis for Guanine Nucleotide Exchange on Ran by the Regulator of Chromosome Condensation (RCC1). *Cell*, *105*(2), 245–255.
42) Structural basis for activation of ARF GTPase: mechanisms of guanine nucleotide exchange and GTP-myristoyl switching.*Cell.* 1998; 95: 237-248
43) Itzen, A., Pylypenko, O., Goody, R. S., Alexandrov, K., & Rak, A. (2006). Nucleotide exchange via local protein unfolding—structure of Rab8 in complex with MSS4. *The EMBO Journal*, *25*(7), 1445–1455.
44) Miller, K. G., Alfonso, A., Nguyen, M., Crowell, J. A., Johnson, C. D., & Rand, J. B. (1996). A genetic selection for Caenorhabditis elegans synaptic transmission mutants. *Proceedings of the National Academy of Sciences*, *93*(22), 12593–12598.
45) Miller, K. G., Emerson, M. D., McManus, J. R., & Rand, J. B. (2000). RIC-8 (Synembryn): A Novel Conserved Protein that Is Required for Gqα Signaling in the C. elegans Nervous System. *Neuron*, *27*(2), 289–299.
46)Miller, K. G., & Rand, J. B. (n.d.). *A Role for RIC-8 (Synembryn) and GOA-1 (Go□) in Regulating a Subset of Centrosome Movements During Early Embryogenesis in Caenorhabditis elegans*. 12.
47) Schade, M. A., Reynolds, N. K., Dollins, C. M., & Miller, K. G. (2005). Mutations That Rescue the Paralysis of Caenorhabditis elegans ric-8 (Synembryn) Mutants Activate the Gαs Pathway and Define a Third Major Branch of the Synaptic Signaling Network. *Genetics*, *169*(2), 631–649.
48) Reynolds, N. K., Schade, M. A., & Miller, K. G. (2005). Convergent, RIC-8-Dependent Gα Signaling Pathways in the Caenorhabditis elegans Synaptic Signaling Network. *Genetics*, *169*(2), 651–670.
49) *Wilkie, T. M., & Kinch, L. (2005). New Roles for Gα and RGS Proteins: Communication Continues despite Pulling Sisters Apart. Current Biology, 15(20), R843–R854.*
50) Klattenhoff, C., Montecino, M., Soto, X., Guzmán, L., Romo, X., de los Angeles García, M., Mellstrom, B., Naranjo, J. R., Hinrichs, M. V., & Olate, J. (2003). Human brain synembryn interacts with Gsα and Gqα and is translocated to the plasma membrane in response to isoproterenol and carbachol. Journal of Cellular Physiology, 195(2), 151–157.
51) David, N. B., Martin, C. A., Segalen, M., Rosenfeld, F., Schweisguth, F., & Bellaïche, Y. (2005). Drosophila Ric-8 regulates Gαi cortical localization to promote Gαi-dependent planar orientation of the mitotic spindle during asymmetric cell division. *Nature Cell Biology*, *7*(11), 1083–1090.
52) Hampoelz, B., Hoeller, O., Bowman, S. K., Dunican, D., & Knoblich, J. A. (2005). Drosophila Ric-8 is essential for plasma-membrane localization of heterotrimeric G proteins. *Nature Cell Biology*, *7*(11), 1099–1105.
53) Wang, H., Ng, K. H., Qian, H., Siderovski, D. P., Chia, W., & Yu, F. (2005). Ric-8 controls Drosophila neural progenitor asymmetric division by regulating heterotrimeric G proteins. *Nature Cell Biology*, *7*(11), 1091–1098.
54) Oner, S. S., Maher, E. M., Gabay, M., Tall, G. G., Blumer, J. B., & Lanier, S. M. (2013). Regulation of the G-protein Regulatory-Gαi Signaling Complex by Nonreceptor Guanine Nucleotide Exchange Factors. *The Journal of Biological Chemistry*, *288*(5), 3003–3015.
55) Woodard, G. E., Huang, N.-N., Cho, H., Miki, T., Tall, G. G., & Kehrl, J. H. (2010). Ric-8A and Giα Recruit LGN, NuMA, and Dynein to the Cell Cortex To Help Orient the Mitotic Spindle. *Molecular and Cellular Biology*, *30*(14), 3519–3530.

56) Gabay, M., Pinter, M. E., Wright, F. A., Chan, P., Murphy, A. J., Valenzuela, D. M., Yancopoulos, G. D., & Tall, G. G. (2011). Ric-8 Proteins Are Molecular Chaperones That Direct Nascent G Protein α Subunit Membrane Association. *Science Signaling*, *4*(200).
57)Papasergi, M. M., Patel, B. R., & Tall, G. G. (2015). The G Protein α Chaperone Ric-8 as a Potential Therapeutic Target. *Molecular Pharmacology*, *87*(1), 52–63.
58) Gabay, M., Pinter, M. E., Wright, F. A., Chan, P., Murphy, A. J., Valenzuela, D. M., Yancopoulos, G. D., & Tall, G. G. (2011). Ric-8 Proteins Are Molecular Chaperones That Direct Nascent G Protein α Subunit Membrane Association. *Science Signaling*, *4*(200).
59) Gabay, M., Pinter, M. E., Wright, F. A., Chan, P., Murphy, A. J., Valenzuela, D. M., Yancopoulos, G. D., & Tall, G. G. (2011). Ric-8 Proteins Are Molecular Chaperones That Direct Nascent G Protein α Subunit Membrane Association. *Science Signaling*, *4*(200).
60) Chan, P., Thomas, C. J., Sprang, S. R., & Tall, G. G. (2013). Molecular chaperoning function of Ric-8 is to fold nascent heterotrimeric G protein α subunits. *Proceedings of the National Academy of Sciences*, *110*(10), 3794–3799.
61) Nagai, Y., Nishimura, A., Tago, K., Mizuno, N., & Itoh, H. (2010). Ric-8B Stabilizes the α Subunit of Stimulatory G Protein by Inhibiting Its Ubiquitination. *The Journal of Biological Chemistry*, *285*(15), 11114–11120.
62) Chishiki, K., Kamakura, S., Yuzawa, S., Hayase, J., & Sumimoto, H. (2013). Ubiquitination of the heterotrimeric G protein α subunits Gαi2 and Gαq is prevented by the guanine nucleotide exchange factor Ric-8A. *Biochemical and Biophysical Research Communications*, *435*(3), 414–419.
63) Tall, G. G., Krumins, A. M., & Gilman, A. G. (2003). Mammalian Ric-8A (Synembryn) Is a Heterotrimeric Gα Protein Guanine Nucleotide Exchange Factor. Journal of Biological Chemistry, 278(10), 8356–8362.
64) Chan, P., Gabay, M., Wright, F. A., & Tall, G. G. (2011). Ric-8B Is a GTP-dependent G Protein αs Guanine Nucleotide Exchange Factor. The Journal of Biological Chemistry, 286(22), 19932–19942.
65) Thomas, C. J., Tall, G. G., Adhikari, A., & Sprang, S. R. (2008). Ric-8A Catalyzes Guanine Nucleotide Exchange on Gαi1 Bound to the GPR/GoLoco Exchange Inhibitor AGS3. The Journal of Biological Chemistry, 283(34), 23150–23160.
66) Pinna, L. A. (1990). Casein kinase 2: An 'eminence grise' in cellular regulation? Biochimica et Biophysica Acta (BBA) - Molecular Cell Research, 1054(3), 267–284.
67) Pinna, L. A., & Meggio, F. (1997). Protein kinase CK2 ("casein kinase-2") and its implication in cell division and proliferation. Progress in Cell Cycle Research, 3, 77–97.
68)Faust, M., & Montenarh, M. (2000). Subcellular localization of protein kinase CK2. Cell and Tissue Research, 301(3), 329–340.
69) Xu, X., Toselli, P. A., Russell, L. D., & Seldin, D. C. (1999). Globozoospermia in mice lacking the casein kinase II α' catalytic subunit. Nature Genetics, 23(1), 118–121.
70) Litchfield, D. W. (2003). Protein kinase CK2: structure, regulation and role in cellular decisions of life and death. Biochemical Journal, 369(1), 1–15.
71) Meggio, F., & Pinna, L. A. (2003). One-thousand-and-one substrates of protein kinase CK2? The FASEB Journal, 17(3), 349–368.
72) Trembley, J. H., Wang, G., Unger, G., Slaton, J., & Ahmed, K. (2009). CK2: A key player in cancer biology. Cellular and Molecular Life Sciences : CMLS, 66(0), 1858–1867.
73) Ruzzene, M., & Pinna, L. A. (2010). Addiction to protein kinase CK2: A common denominator of diverse cancer cells? Biochimica et Biophysica Acta (BBA) - Proteins and Proteomics, 1804(3), 499–504.
74) Montenarh, M. (2016). Protein kinase CK2 in DNA damage and repair. Translational Cancer Research, 5(1), 49-63–63.

75) Olsen, B. B., Wang, S.-Y., Svenstrup, T. H., Chen, B. P., & Guerra, B. (2012). Protein kinase CK2 localizes to sites of DNA double-strand break regulating the cellular response to DNA damage. BMC Molecular Biology, 13, 7.
76) Loizou, J. I., El-Khamisy, S. F., Zlatanou, A., Moore, D. J., Chan, D. W., Qin, J., Sarno, S., Meggio, F., Pinna, L. A., & Caldecott, K. W. (2004). The Protein Kinase CK2 Facilitates Repair of Chromosomal DNA Single-Strand Breaks. Cell, 117(1), 17–28.
77) Götz, C., & Montenarh, M. (2013). Protein kinase CK2 in the ER stress response. *Advances in Biological Chemistry*, *3*(3), 1–5.
78) Ahmad, K. A., Wang, G., Unger, G., Slaton, J., & Ahmed, K. (2008). Protein kinase CK2 – A key suppressor of apoptosis. *Advances in Enzyme Regulation*, *48*(1), 179–187.
79) Yamane, K., & Kinsella, T. J. (2005). Casein kinase 2 regulates both apoptosis and the cell cycle following DNA damage induced by 6-thioguanine. *Clinical Cancer Research: An Official Journal of the American Association for Cancer Research*, *11*(6), 2355–2363.
80) Izeradjene, K., Douglas, L., Delaney, A., & Houghton, J. A. (2005). Casein kinase II (CK2) enhances death-inducing signaling complex (DISC) activity in TRAIL-induced apoptosis in human colon carcinoma cell lines. *Oncogene*, *24*(12), 2050–2058.
81) Quobaili, F. A., & Montenarh, M. (2012). CK2 and the regulation of the carbohydrate metabolism. *Metabolism - Clinical and Experimental*, *61*(11), 1512–1517.
82) Montenarh, M. (2014). Protein Kinase CK2 and Angiogenesis. *Advances in Clinical and Experimental Medicine*, *23*(2), 153–158.
83) Yu, W., Yu, M., Papasergi-Scott, M. M., & Tall, G. G. (2019). Production of Phosphorylated Ric-8A proteins using protein kinase CK2. *Protein Expression and Purification*, *154*, 98–103.
84) Papasergi-Scott, M. M., Stoveken, H. M., MacConnachie, L., Chan, P.-Y., Gabay, M., Wong, D., Freeman, R. S., Beg, A. A., & Tall, G. G. (2018). Dual phosphorylation of Ric-8A enhances its ability to mediate G protein α subunit folding and to stimulate guanine nucleotide exchange. *Science Signaling*, *11*(532).
85) Figueroa, M., Victoria Hinrichs, M., Bunster, M., Babbitt, P., Martinez-Oyanedel, J., & Olate, J. (2009). Biophysical studies support a predicted superhelical structure with armadillo repeats for Ric-8. *Protein Science*, *18*(6), 1139–1145.
86) Zeng, B., Mou, T.-C., Doukov, T. I., Steiner, A., Yu, W., Papasergi-Scott, M., Tall, G. G., Hagn, F., & Sprang, S. R. (2019). Structure, Function, and Dynamics of the Gα Binding Domain of Ric-8A. *Structure*, *27*(7), 1137-1147.e5.
87) Andrade, M. A., Petosa, C., O'Donoghue, S. I., Müller, C. W., & Bork, P. (2001). Comparison of ARM and HEAT protein repeats11Edited by P. E. Wright. *Journal of Molecular Biology*, *309*(1), 1–18.
88) Thomas, C. J., Briknarová, K., Hilmer, J. K., Movahed, N., Bothner, B., Sumida, J. P., Tall, G. G., & Sprang, S. R. (2011). The Nucleotide Exchange Factor Ric-8A Is a Chaperone for the Conformationally Dynamic Nucleotide-Free State of Gαi1. *PLOS ONE*, *6*(8), e23197.
89) Srivastava, D., Gakhar, L., & Artemyev, N. O. (2019). Structural underpinnings of Ric8A function as a G-protein α-subunit chaperone and guanine-nucleotide exchange factor. *Nature Communications*, *10*(1), 3084.
90) Kant, R., Zeng, B., Thomas, C. J., Bothner, B., & Sprang, S. R. (2016). *Ric-8A, a G protein chaperone with nucleotide exchange activity induces long- range secondary structure changes in Ga*. 20.
91) Van Eps, N., Thomas, C. J., Hubbell, W. L., & Sprang, S. R. (2015). The guanine nucleotide exchange factor Ric-8A induces domain separation and Ras domain plasticity in Gαi1. *Proceedings of the National Academy of Sciences*, *112*(5), 1404–1409.

92) Shoemaker, S. C., & Ando, N. (2018). X-rays in the Cryo-EM Era: Structural Biology's Dynamic Future. *Biochemistry*, *57*(3), 277–285.
93) Kühlbrandt, W. (2014). Cryo-EM enters a new era. *ELife*, *3*, e03678.
94) Nogales, E., & Scheres, S. H. W. (2015). Cryo-EM: A Unique Tool for the Visualization of Macromolecular Complexity. *Molecular Cell*, *58*(4), 677–689.
95) Orlov, I., Myasnikov, A. G., Andronov, L., Natchiar, S. K., Khatter, H., Beinsteiner, B., Ménétret, J.-F., Hazemann, I., Mohideen, K., Tazibt, K., Tabaroni, R., Kratzat, H., Djabeur, N., Bruxelles, T., Raivoniaina, F., Pompeo, L. di, Torchy, M., Billas, I., Urzhumtsev, A., & Klaholz, B. P. (2017). The integrative role of cryo electron microscopy in molecular and cellular structural biology. *Biology of the Cell*, *109*(2), 81–93.
96) Danev, R., Yanagisawa, H., & Kikkawa, M. (2019). Cryo-Electron Microscopy Methodology: Current Aspects and Future Directions. *Trends in Biochemical Sciences*, *44*(10), 837–848.
97) Cheng, Y., Glaeser, R. M., & Nogales, E. (2017). How Cryo-EM Became so Hot. *Cell*, *171*(6), 1229–1231.
98) Murata, K., & Wolf, M. (2018). Cryo-electron microscopy for structural analysis of dynamic biological macromolecules. *Biochimica et Biophysica Acta (BBA) - General Subjects*, *1862*(2), 324–334.
99) Herzik, M. A., Wu, M., & Lander, G. C. (2019). High-resolution structure determination of sub-100 kDa complexes using conventional cryo-EM. *Nature Communications*, *10*(1), 1032.
100) Fan, X., Wang, J., Zhang, X., Yang, Z., Zhang, J.-C., Zhao, L., Peng, H.-L., Lei, J., & Wang, H.-W. (2019). Single particle cryo-EM reconstruction of 52 kDa streptavidin at 3.2 Angstrom resolution. *Nature Communications*, *10*(1), 2386.
101) Khoshouei, M., Radjainia, M., Baumeister, W., & Danev, R. (2017). Cryo-EM structure of haemoglobin at 3.2 Å determined with the Volta phase plate. *Nature Communications*, *8*(1), 16099.
102) Grey, J. L., & Thompson, D. H. (2010). Challenges and opportunities for new protein crystallization strategies in structure-based drug design. *Expert Opinion on Drug Discovery*, *5*(11), 1039–1045.
103) Carpenter, E. P., Beis, K., Cameron, A. D., & Iwata, S. (2008). Overcoming the challenges of membrane protein crystallography. *Current opinion in structural biology*, *18*(5), 581–586. doi:10.1016/j.sbi.2008.07.001
104) Holcomb, J., Spellmon, N., Zhang, Y., Doughan, M., Li, C., & Yang, Z. (2017). Protein crystallization: Eluding the bottleneck of X-ray crystallography. *AIMS biophysics*, *4*(4), 557–575. doi:10.3934/biophy.2017.4.557
105) Cheng, Y. (2015). Single-Particle Cryo-EM at Crystallographic Resolution. *Cell*, *161*(3), 450–457.
106) Schwander, P., Fung, R., Phillips, G. N., & Ourmazd, A. (2010). Mapping the conformations of biological assemblies. *New Journal of Physics*, *12*(3), 035007.
107) Choi, K. J., Shin, J. I., & Lee, S. H. (2018). Workflw of Cryo-Electron Microscopy and Status of Domestic Infrastructure. *Applied Microscopy*, *48*(1), 6–10.
108) Carroni, M., & Saibil, H. R. (2016). Cryo electron microscopy to determine the structure of macromolecular complexes. *Methods*, *95*, 78–85.
109) Frank J, Verschoor A, and Boublik M (1981) Computer averaging of electron micrographs of 40S ribosomal subunits. Science 214, 1353-1355.
110) Scheres S H (2012) RELION: implementation of a Bayesian approach to cryo-EM structure determination. J. Struct. Biol. 180, 519-530
111) Punjani, A., Rubinstein, J. L., Fleet, D. J., & Brubaker, M. A. (2017). cryoSPARC: algorithms for rapid unsupervised cryo-EM structure determination. *Nature Methods*, *14*(3), 290–296.

112) Afonine, P. V., Poon, B. K., Read, R. J., Sobolev, O. V., Terwilliger, T. C., Urzhumtsev, A., & Adams, P. D. (2018). Real-space refinement in *PHENIX* for cryo-EM and crystallography. *Acta Crystallographica Section D Structural Biology*, *74*(6), 531–544.
113) Thompson, R. F., Walker, M., Siebert, C. A., Muench, S. P., & Ranson, N. A. (2016). An introduction to sample preparation and imaging by cryo-electron microscopy for structural biology. *Methods*, *100*, 3–15.
114) Passmore, L. A., & Russo, C. J. (2016). Specimen Preparation for High-Resolution Cryo-EM. In *Methods in Enzymology* (Vol. 579, pp. 51–86). Elsevier.
115) Dubochet, J., Adrian, M., Lepault, J., & McDowall, A. W. (1985). *Cryo-electron microscopy of vitrified biological specimens*. 4.
116) Kasas, S., Dumas, G., Dietler, G., Catsicas, S., & Adrian, M. (2003). Vitrification BlackwellPublishingLtd. of cryoelectron microscopy specimens revealed by high-speed photographic imaging. *Journal of Microscopy*, 6.
117) Baker, L. A., & Rubinstein, J. L. (2010). Chapter Fifteen - Radiation Damage in Electron Cryomicroscopy. In G. J. Jensen (Ed.), *Methods in Enzymology* (Vol. 481, pp. 371–388). Academic Press.
118) Jensen, G. J. (2001). Alignment Error Envelopes for Single Particle Analysis. *Journal of Structural Biology*, *133*(2), 143–155.
119) Kudryashev, M., Castaño-Díez, D., & Stahlberg, H. (2012). Limiting factors in single particle cryo electron tomography. *Computational and Structural Biotechnology Journal*, *1*.
120) Glaeser, R. M., & Han, B.-G. (2017). Opinion: hazards faced by macromolecules when confined to thin aqueous films. *Biophysics Reports*, *3*(1–3), 1–7.
121) Taylor KA, Glaeser RM (2008) Retrospective on the earlydevelopment of cryoelectron microscopy of macromoleculesand a prospective on opportunities for the future. J Struct Biol163:214–223
122) D'Imprima, E., Floris, D., Joppe, M., Sánchez, R., Grininger, M., & Kühlbrandt, W. (2019). Protein denaturation at the air-water interface and how to prevent it. *ELife*, *8*, e42747.
123) Vinothkumar, K. R., & Henderson, R. (2016). Single particle electron cryomicroscopy: trends, issues and future perspective. *Quarterly Reviews of Biophysics*, *49*, e13.
124) Kelly DF, Abeyrathne PD, Dukovski D, Walz T (2008) The affinitygrid: a pre-fabricated EM grid for monolayer purification.J Mol Biol 382:423–433
125) Benjamin CJ, Wright KJ, Hyun S-H, Krynski K, Yu G, Bajaj R, Guo F,Stauffacher CV, Jiang W, Thompson DH (2016) NonfoulingNTA-PEG-based TEM grid coatings for selective capture ofhistidine-tagged protein targets from cell lysates. Langmuir32:551–559
126) Naydenova, K., Peet, M. J., & Russo, C. J. (2019). Multifunctional graphene supports for electron cryomicroscopy. *Proceedings of the National Academy of Sciences*, *116*(24), 11718–11724.
127) FRANK, J. 2006. Three-dimensional electron microscopy of macromolecular assemblies : visualization of biological molecules in their native state, Oxford ; New York, Oxford University Press.
128) Inkson, B. J. (2016). 2 - Scanning electron microscopy (SEM) and transmission electron microscopy (TEM) for materials characterization. In G. Hübschen, I. Altpeter, R. Tschuncky, & H.-G. Herrmann (Eds.), *Materials Characterization Using Nondestructive Evaluation (NDE) Methods* (pp. 17–43). Woodhead Publishing.
129) Veesler, D., Campbell, M. G., Cheng, A., Fu, C., Murez, Z., Johnson, J. E., Potter, C. S., & Carragher, B. (2013). Maximizing the potential of electron cryomicroscopy data collected using direct detectors. *Journal of Structural Biology*, *184*(2).
130) Wu, S., Armache, J.-P., & Cheng, Y. (2016). Single-particle cryo-EM data acquisition by using direct electron detection camera. *Microscopy*, *65*(1), 35–41.

131) McMullan, G., Faruqi, A. R., & Henderson, R. (2016). Direct Electron Detectors. In *Methods in Enzymology* (Vol. 579, pp. 1–17). Elsevier.
132) Faruqi, A. R. (1998). Design principles and applications of a cooled CCD camera for electron microscopy. *Advances in Experimental Medicine and Biology*, *453*, 63–72.
133) Bai, X., Fernandez, I. S., McMullan, G., & Scheres, S. H. (2013). Ribosome structures to near-atomic resolution from thirty thousand cryo-EM particles. *ELife*, *2*, e00461.
134) Campbell, M. G., Cheng, A., Brilot, A. F., Moeller, A., Lyumkis, D., Veesler, D., Pan, J., Harrison, S. C., Potter, C. S., Carragher, B., & Grigorieff, N. (2012). Movies of Ice-Embedded Particles Enhance Resolution in Electron Cryo-Microscopy. *Structure*, *20*(11), 1823–1828.
135) Rubinstein, J. L., & Brubaker, M. A. (2015). Alignment of cryo-EM movies of individual particles by optimization of image translations. *Journal of Structural Biology*, *192*(2), 188–195.
136) Ripstein, Z. A., & Rubinstein, J. L. (2016). Chapter Five - Processing of Cryo-EM Movie Data. In R. A. Crowther (Ed.), *Methods in Enzymology* (Vol. 579, pp. 103–124). Academic Press.
137) Mastronarde, D. N. (2005). Automated electron microscope tomography using robust prediction of specimen movements. *Journal of Structural Biology*, *152*(1), 36–51.
138) Carragher, B., Kisseberth, N., Kriegman, D., Milligan, R. A., Potter, C. S., Pulokas, J., & Reilein, A. (2000). Leginon: An Automated System for Acquisition of Images from Vitreous Ice Specimens. *Journal of Structural Biology*, *132*(1), 33–45.
139) Tan, Y. Z., Cheng, A., Potter, C. S., & Carragher, B. (2016). Automated data collection in single particle electron microscopy. *Microscopy*, *65*(1), 43–56.
140) Scheres, S. H. W. (2016). Chapter Six - Processing of Structurally Heterogeneous Cryo-EM Data in RELION. In R. A. Crowther (Ed.), *Methods in Enzymology* (Vol. 579, pp. 125–157). Academic Press.
141) Serna, M. (2019). Hands on Methods for High Resolution Cryo-Electron Microscopy Structures of Heterogeneous Macromolecular Complexes. *Frontiers in Molecular Biosciences*, *6*.
142) Tang, G., Peng, L., Baldwin, P. R., Mann, D. S., Jiang, W., Rees, I., & Ludtke, S. J. (2007). EMAN2: An extensible image processing suite for electron microscopy. *Journal of Structural Biology*, *157*(1), 38–46.
143) Boekema, E. J., Folea, M., & Kouřil, R. (2009). Single particle electron microscopy. *Photosynthesis Research*, *102*(2–3), 189–196.
144) Sigworth, F. J. (2016). Principles of cryo-EM single-particle image processing. *Microscopy*, *65*(1), 57–67.
145) Carazo, J. M., Sorzano, C. O. S., Otón, J., Marabini, R., & Vargas, J. (2015). Three-dimensional reconstruction methods in Single Particle Analysis from transmission electron microscopy data. *Archives of Biochemistry and Biophysics*, *581*, 39–48.
146) Rohou, A., & Grigorieff, N. (2019). *CTFFIND4: Fast and accurate defocus estimation from electron micrographs*. 18.
147) Zhang K. (2016). Gctf: Real-time CTF determination and correction. *Journal of structural biology*, *193*(1), 1–12. doi:10.1016/j.jsb.2015.11.003
148) Zanetti, G., Riches, J. D., Fuller, S. D., & Briggs, J. A. (2009). Contrast transfer function correction applied to cryo-electron tomography and sub-tomogram averaging. *Journal of structural biology*, *168*(2), 305–312. doi:10.1016/j.jsb.2009.08.002
149) Zhu, J., Penczek, P.A., Schroder, R., and Frank, J. (1997). Three-dimensional reconstruction with contrast transfer function correction from energy-filtered cryoelectron micrographs: procedure and application to the 70S Escherichia coli ribosome. J Struct Biol118, 197-219.
150) Scheres, S.H., and Chen, S. (2012). Prevention of overfitting in cryo-EM structure determination. Nat Methods9, 853-854.

151) van Heel, M., and Schatz, M. (2005). Fourier shell correlation threshold criteria. J Struct Biol151, 250-262
152) Chen, S., McMullan, G., Faruqi, A.R., Murshudov, G.N., Short, J.M., Scheres, S.H., and Henderson, R. (2013). High-resolution noise substitution to measure overfitting and validate resolution in 3D structure determination by single particle electron cryomicroscopy. Ultramicroscopy135, 24-35.
153) Rosenthal, P.B., and Henderson, R. (2003). Optimal determination of particle orientation, absolute hand, and contrast loss in single-particle electron cryomicroscopy. J Mol Biol333, 721-745.
154) Scheres, S.H. (2014). Beam-induced motion correction for sub-megadalton cryo-EM particles. Elife3, e03665.
155) Griffin, L., & Lawson, A. (2011). Antibody fragments as tools in crystallography. *Clinical and experimental immunology*, *165*(3), 285–291. doi:10.1111/j.1365-2249.2011.04427.x
156) Wu, S., Avila-Sakar, A., Kim, J., Booth, D. S., Greenberg, C. H., Rossi, A., … Cheng, Y. (2012). Fabs enable single particle cryoEM studies of small proteins. *Structure (London, England : 1993)*, *20*(4), 582–592. doi:10.1016/j.str.2012.02.017.
157) Kim, J., Tan, Y. Z., Wicht, K. J., Erramilli, S. K., Dhingra, S. K., Okombo, J., Vendome, J., Hagenah, L. M., Giacometti, S. I., Warren, A. L., Nosol, K., Roepe, P. D., Potter, C. S., Carragher, B., Kossiakoff, A. A., Quick, M., Fidock, D. A., & Mancia, F. (2019). Structure and drug resistance of the Plasmodium falciparum transporter PfCRT. *Nature*, *576*(7786), 315–320.
158) Zhu, S., Noviello, C. M., Teng, J., Walsh, R. M., Kim, J. J., & Hibbs, R. E. (2018). Structure of a human synaptic GABA-A receptor. *Nature*, *559*(7712), 67–72.
159) Xenaki, K. T., Oliveira, S., & van Bergen en Henegouwen, P. M. P. (2017). Antibody or Antibody Fragments: Implications for Molecular Imaging and Targeted Therapy of Solid Tumors. *Frontiers in Immunology*, *8*.
160) El-Sayed, A., Bernhard, W., Barreto, K., Gonzalez, C., Hill, W., Pastushok, L., Fonge, H., & Geyer, C. R. (2018). Evaluation of antibody fragment properties for near-infrared fluorescence imaging of HER3-positive cancer xenografts. *Theranostics*, *8*(17), 4856–4869.
161) Pardon, E., Laeremans, T., Triest, S., Rasmussen, S. G. F., Wohlkönig, A., Ruf, A., Muyldermans, S., Hol, W. G. J., Kobilka, B. K., & Steyaert, J. (2014). A general protocol for the generation of Nanobodies for structural biology. *Nature Protocols*, *9*(3), 674–693.
162) Muyldermans, S., Cambillau, C., & Wyns, L. (2001). Recognition of antigens by single-domain antibody fragments: the superfluous luxury of paired domains. *Trends in Biochemical Sciences*, *26*(4), 230–235.
163) Muyldermans, S. (2013). Nanobodies: Natural Single-Domain Antibodies. *Annual Review of Biochemistry*, *82*(1), 775–797.
164) Bennett, K. L., Smith, S. V., Truscott, R. J. W., & Sheil, M. M. (1997). Monitoring Papain Digestion of a Monoclonal Antibody by Electrospray Ionization Mass Spectrometry. *Analytical Biochemistry*, *245*(1), 17–27.
165) Rasmussen, S. G. F., Choi, H.-J., Fung, J. J., Pardon, E., Casarosa, P., Chae, P. S., DeVree, B. T., Rosenbaum, D. M., Thian, F. S., Kobilka, T. S., Schnapp, A., Konetzki, I., Sunahara, R. K., Gellman, S. H., Pautsch, A., Steyaert, J., Weis, W. I., & Kobilka, B. K. (2011). Structure of a nanobody-stabilized active state of the β2 adrenoceptor. *Nature*, *469*(7329), 175–180.
166) Lauwereys, M., Arbabi Ghahroudi, M., Desmyter, A., Kinne, J., Hölzer, W., De Genst, E., … Muyldermans, S. (1998). Potent enzyme inhibitors derived from dromedary heavy-chain antibodies. *The EMBO journal*, *17*(13), 3512–3520. doi:10.1093/emboj/17.13.3512
167) De Genst, E., Silence, K., Decanniere, K., Conrath, K., Loris, R., Kinne, J., … Wyns, L. (2006). Molecular basis for the preferential cleft recognition by dromedary heavy-chain antibodies.

Proceedings of the National Academy of Sciences of the United States of America, *103*(12), 4586–4591. doi:10.1073/pnas.0505379103.
168) McClelland, L.J., Zhang, K., Mou, T. *et al.* Structure of the G protein chaperone and guanine nucleotide exchange factor Ric-8A bound to Gαi1. *Nat Commun* **11,** 1077 (2020).
169) Seven, Alpay Burak, et al. “Structures of Gα Proteins in Complex with Their Chaperone Reveal Quality Control Mechanisms.” *Cell Reports*, vol. 30, no. 11, 2020, doi:10.1016/j.celrep.2020.02.086.
170) Coleman, D. E., & Sprang, S. R. (1999). Structure of Gialpha1.GppNHp, autoinhibition in a galpha protein-substrate complex. *The Journal of biological chemistry*, *274*(24), 16669–16672.
171) Vetter, I. R. & Wittinghofer, A. The guanine nucleotide-binding switch in three dimensions. *Science* **294**, 1299–1304 (2001)
172) Flock, T., Ravarani, C., Sun, D. *et al.* Universal allosteric mechanism for Gα activation by GPCRs. *Nature* **524,** 173–179 (2015).
173) Pardon, E., Laeremans, T., Triest, S., Rasmussen, S. G., Wohlkönig, A., Ruf, A., Muyldermans, S., Hol, W. G., Kobilka, B. K., & Steyaert, J. (2014). A general protocol for the generation of Nanobodies for structural biology. *Nature protocols*, *9*(3), 674–693.